DEPARTAMENT OF
PHYSICS

NOVA SCHOOL OF
SCIENCE & TECHNOLOGY

BRUNO MIGUEL PEREIRA PASSARINHO

Bachelor in Biomedical Engineering

SURFACE FUNCTIONALIZATION OF RESORBABLE BIOMEDICAL IMPLANTS WITH METALLIC OXIDES

DISSERTATION

MASTER IN BIOMEDICAL ENGINEERING

NOVA University Lisbon

March, 2024

NOVA SCHOOL OF SCIENCE & TECHNOLOGY

DEPARTAMENT OF PHYSICS

SURFACE FUNCTIONALIZATION OF RESORBABLE BIOMEDICAL IMPLANTS WITH METALLIC OXIDES

DISSERTATION

BRUNO MIGUEL PEREIRA PASSARINHO

Bachelor in Biomedical Engineering

Adviser: João Pedro Oliveira
Full Professor, NOVA University Lisbon

Co-adviser: Ana Baptista
Researcher, NOVA University Lisbon

Examination Committee:

Chair: Susana Isabel dos Santos Silva Sério Venceslau,
Associate Professor, NOVA University Lisbon

Rapporteurs: Jorge Alexandre Monteiro Carvalho Silva,
Associate Professor, NOVA University Lisbon

Adviser: João Pedro Oliveira,
Full Professor, NOVA University Lisbon

MASTER IN BIOMEDICAL ENGINEERING

NOVA University Lisbon
March, 2024

Surface Functionalization of Resorbable Biomedical Implants with Metallic Oxides

ACKNOWLEDGMENTS

Firstly, I want to thank Professor João Pedro Oliveira and Professor Ana Baptista for their help, guidance, and companionship, enhanced by their scientific expertise, which motivated to the continuous pursuit of knowledge. I also want to express my gratitude to Professor Isabel Ferreira for all the support throughout these months. Next, I would like to thank my colleagues in the laboratory for the great atmosphere they provided throughout this project. To Catarina Carmo, Miguel Brito, Catarina Bianchi, Mariana Moniz and João Carmo for being there at any time and essentially for trusting that the laboratory wouldn't explode in the pursuit of knowledge. A special mention to Jia Jia and Maria Morais, for the assistance provided during this project. To Mariana, Júlio, Marta, Catarina, Madalena, and Beatriz, for being united in each other's struggles and trying to help each other even if it was just to convey confidence that everything would go well. And finally, I want to thank my "bestie" in the laboratory, Cristiana, for the random but genuine friendship that brought us together. Will cherish the moments lived together in research, forever.

I also want to thank the teachers and mentors who contributed to my scientific and personal development, and for inspiring curiosity in the search for something more. To my biomedical colleagues who, from fellow fighters, became lifelong friends. To the impeccable ones, legends! And friends like family! Because they are. To Vasco, Rui, Zé, Dani, Miguel and Rita, friends who believed that the path is made with all its curves and slips, and never stopped supporting. To the family that life has given me and that has been there in the good and not so good moments year after year. I would also like to thank my family for their presence and support in all moments. For my father and mother, for providing everything I could hope for, in the pursuit of my future. To Joana for the wonderful Tom and Jerry relationship and to Sara, whose presence endured and inspired the writing of this work. Never would´ve imagined all the wonderful gifts from the Atlantic pearl. I hold you all in my heart and express my gratitude.

This work was carried out within the scope of the project "All-Fiber Integrated Photovoltaic Storage Devices for e-Textiles" with reference PTDC/CTM-CTM/157/2020, funded by national funds through FCT, IP.

"Success is not final; failure is not fatal: It is the courage to continue that counts." (W. S. Churchill).

ABSTRACT

Bioresorbable materials, like magnesium alloys, offer promising prospects in medical implants, naturally degrading within the body and negating removal surgeries. Yet, challenges persist in enhancing their corrosion resistance and biocompatibility. This study delves into magnesium alloys' behavior in simulated body fluids, exploring methods for bolstering corrosion resistance via surface functionalization. Such advancements are pivotal in advancing medical implant technology and ameliorating patient outcomes. Additionally, Wire Arc Additive Manufacturing (WAAM) emerges as a cost-effective solution for fabricating intricate, patient-specific implants, including magnesium alloys, augmenting biocompatibility and integration. Electrodeposited TiO_2 coatings further enhance implant properties, warranting optimization for tailored biomedical applications.

This work aimed to the functionalization of WAAM-printed Magnesium based AZ61A alloy samples with TiO_2 coatings applied via Electrodeposition, to improve the substrates resistance to corrosion and degradation. The surfaces were characterized using Raman Spectroscopy and XRD, with SEM analysis being used to detail microstructure morphology. To access the potential benefits of the TiO_2 coating, corrosion resistance and electrochemical activity of coated and uncoated substrates were assessed through Cyclic Voltammetry, alongside mass variation analysis in static in-vitro degradation tests. The study concluded that coating the WAAM substrates with TiO_2 potentially enhances their corrosion resistance in electrochemical activity and degradation under simulated human body conditions. Optimal electrodeposition TiO_2 parameters were determined to be 1V for 45 minutes, with $TiCl_4$ as a precursor. At these voltage parameters, the samples exhibited thicker and more homogeneous coatings compared to 0.5 V, where the coating was heterogeneous, or 1.5 and 2 V, where cluster aggregation occurred. Deposition times of 15 and 30 minutes resulted in thinner layers, while deposition times of 60 minutes led to decreased surface homogeneity. In accordance with this research, the TiO_2 coating was able to reduce the alloy degradation in-vitro, also creating a corrosion protective behavior in electrochemical activity.

Keywords: Bioresorbable materials, Electrodeposition, Titanium Dioxide, WAAM, AZ61A

RESUMO

Os materiais bio absorvíveis, como as ligas de magnésio, oferecem perspetivas promissoras em implantes médicos, degradando-se naturalmente no corpo e dispensando as cirurgias de remoção. No entanto, persistem desafios para melhorar a sua resistência à corrosão e biocompatibilidade. Este estudo investiga o comportamento das ligas de magnésio em fluidos corporais simulados, explorando métodos para reforçar a resistência à corrosão através da funcionalização da superfície. Estes avanços são fundamentais para o progresso da tecnologia de implantes médicos e para melhorar os cuidados com os doentes. O Fabrico Aditivo por fio e arco (WAAM) surge como uma solução económica para o fabrico de implantes complexos e específicos para cada doente, incluindo ligas de magnésio, aumentando a biocompatibilidade e a integração. Os revestimentos de TiO_2 por eletrodeposição melhoram as propriedades dos implantes, justificando a otimização para aplicações biomédicas personalizadas. Este trabalho teve como objetivo a funcionalização de amostras de liga de magnésio AZ61A impressas por WAAM com revestimentos de TiO_2 aplicados por eletrodeposição, para melhorar a resistência dos substratos à corrosão e à degradação. As superfícies foram caracterizadas usando espetroscopia Raman e XRD, com análise SEM sendo usada para detalhar a morfologia da microestrutura de superfície. Para avaliar os potenciais benefícios do revestimento de TiO_2, a resistência à corrosão e a atividade eletroquímica dos substratos revestidos e não revestidos foram avaliadas através de Voltametria Cíclica, juntamente com a análise da variação de massa em testes de degradação estática *in-vitro*. O estudo concluiu que o revestimento dos substratos WAAM com TiO2 pode aumentar a sua resistência à corrosão em atividade eletroquímica e degradação, em condições de corpo humano simuladas. Os parâmetros de eletrodeposição de TiO_2 foram otimizados a 1V durante 45 minutos, com $TiCl_4$ como precursor. Com estes parâmetros, as amostras apresentaram revestimentos mais espessos e homogéneos em comparação com 0,5 V, onde o revestimento era heterogéneo, ou 1,5 e 2 V, onde ocorreu a agregação de aglomerados. Os tempos de deposição de 15 e 30 minutos resultaram em camadas mais finas, e 60 minutos levaram a um revestimento heterogéneo. Observou-se que o revestimento de TiO_2 reduziu a degradação da liga *in-vitro*, criando também um comportamento protetor da corrosão na atividade eletroquímica.

Palavras chave: Biomateriais absorvíveis, Eletrodeposição, Dióxido de Titânio, WAAM, AZ61A

CONTENTS

LIST OF FIGURES

LIST OF TABLES

1

INTRODUCTION

The purpose of the following dissertation is the surface functionalization of resorbable biomedical implants with metallic oxides. Resorbable biomaterials are designed to gradually degrade and be absorbed by the surrounding tissues over time. This unique characteristic, when combined with the study of specific metallic oxides coatings, offers several distinct advantages in medical applications, enhancing the biocompatibility of resorbable biomaterials, promoting better integration with biological tissues, and mitigating the risk of adverse reactions or immune responses commonly associated with implants. Furthermore, titanium dioxide (TiO_2) coatings have been researched for their ability to impart antimicrobial properties to resorbable materials, reducing the risk of infections while improving corrosion resistance, which is critical in surgical settings and represent a groundbreaking innovation with profound implications for medical practice and patient care. By providing temporary structural support or scaffolding during tissue repair and regeneration processes, resorbable biomaterials with TiO_2 coatings facilitate natural healing mechanisms without impeding long-term tissue function, fostering advancements in regenerative medicine and tissue engineering as temporary orthopedic and vascular implants.

This work aims to obtain bioresorbable metallic alloys using wire and arc additive manufacturing (WAAM) and functionalize the substrates surface with a defect free TiO_2 coating through cathodic electrodeposition (ED). The ED parameters that were optimized towards the printed substrates will be presented in detail. We also aimed to the characterization of the coating surface morphology, as well as the behavioral differences between coated and uncoated substrates in electrochemical activity, corrosion resistance and *in-vitro* degradation under simulated body fluids.

This document is divided into 6 chapters: Chapter 2 is related to the theoretical concepts, where the WAAM method, bioresorbable materials and TiO_2 surface functionalization topics are discussed; Chapter 3 is the State of the Art focusing on the Magnesium in biomedical alloys and TiO_2 coating studies; Chapter 4 is an description of the Materials and Methods used during this project; In Chapter 5 the results obtained along with their discussion will be presented. Chapter 6 will approach the conclusions of the work, regarding the proposed objectives and future perspectives.

2

SUMMARY OF THEORETICAL CONCEPTS

In this chapter, some theoretical concepts will be presented. I will address the concept of biomaterials, dwelling into absorbable biomaterials with an emphasis on magnesium and introducing the WAAM technique in their development. Finally, titanium dioxide and its properties as a coating will be discuss.

2.1 Bioresorbable Materials

The remarkable progress in medical science and technology has significantly enhanced human life expectancy and overall well-being. One of the most notable advancements is the development of various biomaterials. Biomaterials encompass both inorganic and organic substances designed to replicate physiological components or processes. Depending on their interaction with host tissues, biomaterials are broadly categorized into biotolerant, bioactive, and bioinert materials. They come in forms such as polymers, ceramics, and metals, and their suitability for use in physiological environments depends on their ability to exhibit excellent biocompatibility, provoke an appropriate biological response, possess suitable mechanical properties, demonstrate superior corrosion resistance, and exhibit high fatigue resistance. [1]. Metallic implants are extensively utilized in orthopedic, cardiovascular, and oral applications among various types of implant materials. These traditional implant materials, such as stainless steels, titanium, and cobalt-chromium alloys, offer commendable resistance to corrosion, wear, and fatigue, coupled with exceptional load-bearing capacities [2]. However, these alloys also contribute to various negative effects, including stress shielding and inflammation of local tissues due to a potential release of cytotoxic ions [3]. Additionally, when used as temporary implants (such as plates, screws, and wires), a second surgery is generally required to remove the implant after the tissues have healed, which leads to increasing patient morbidity and health care costs. Materials that gradually degrade in-vivo with a healthy host response are known as bioresorbable, biodegradable, or bioabsorbable materials. Their derivatives are completely absorbed with no debris and with only minimally hazardous side effects, dissolving completely while supporting tissue repair [4].

Although polymers are dominant in the current medical market, Mg-based, Fe-based and Zn-based alloys have been proposed as better biodegradable materials for load-bearing applications due to their superior combination of strength and ductility over polymers [5]. The conventional approach to metallic biomaterials emphasizes corrosion-resistant metals for use within the body. However, a novel category of materials known as "biodegradable metals" (BMs) has recently challenged this paradigm, offering an alternative for biomedical implants. BMs can be defined as metals designed to gradually corrode in vivo, prompting a suitable host response through the release of corrosion by-products, and ultimately dissolve completely once their role in tissue healing is fulfilled, leaving no residual implant. Thus, BMs primarily consist of essential metallic elements metabolizable by the human body, showcasing appropriate degradation rates and modes within the physiological environment. The typical mode of degradation in BMs is through a corrosion process. The corrosion generally proceeds by an electro-chemical reaction with electrolyte to produce oxides, hydroxides, hydrogen gas, or other compounds. Thus, implant materials that 'corrode', such as magnesium alloys, are currently attracting significant interest [6]. Bioresorbable metals are breaking the current paradigm in bio-material science to develop only corrosion resistant implants. Metals which consist of trace elements existing in the human body are promising candidates for this approach. The purpose of biodegradable implants and coatings is to support tissue regeneration and healing in a specific application by material degradation and concurrent implant replacement through the surrounding tissue. Biodegradable metals have an advantage over existing biodegradable materials such as polymers, ceramics or bioactive glasses in load bearing applications that require a higher tensile strength and a Young's modulus that is closer to bone. Due to their favorable mechanical properties and biocompatibility, as well as the capability to control their rapid corrosion rates, magnesium and its alloys have garnered significant interest as temporary bio-implants. While magnesium's ability to safely biodegrade and its natural biocompatibility render magnesium alloys suitable for temporary implants, their high corrosion rates present a challenge, as they may degrade before the healing process concludes. Various methods, including alloying with different elements and surface modification have been investigated to enhance the biocompatibility and corrosion resistance of different Mg based alloys [1], [7], [8], [9].

2.1.1 Magnesium

Magnesium (Mg) is a lightweight, silvery-white metal commonly utilized as an alloy in engineering applications due to its inherent weakness in its pure form. Magnesium (Mg) metal possesses a lower standard electrode potential compared to hydrogen, allowing it to degrade into Mg ions and hydrogen gas when immersed in an aqueous solution under standard conditions. As the fourth most abundant cation in the human body, and the second most abundant intracellular cation after potassium, magnesium (Mg^{2+}) plays a crucial role in hundreds of biochemical reactions and is essential for the formation of bone and soft tissue, being an essential cofactor for diverse metabolic reactions involving more than 300 enzymes

within the human body. The Tolerable Upper Intake Level for adults is 350 mg/day as average healthy adult requires 24–30 grams of magnesium to maintain regular bodily functions (distributed approximately 53% in bone, 27% in muscle, 19% in soft tissues, and less than 1% in the serum), with the recommended daily allowance (RDA) set between 310–420 mg to ensure overall health and no systemic toxicity or infection effects. Excess magnesium ions can be safely transported through the circulatory system and efficiently excreted via urine and feces without causing adverse effects although excess magnesium typically leads to bowel intolerance, with diarrhoea being the initial sign of excess [10], [11], [12], [13], [14].

At 20°C, the density of Mg and its alloys is approximately 1.74 g/cm^3, making it 1.6 times less dense than aluminium and 4.5 times less dense than steel. Interestingly, Mg's density is slightly lower than that of natural bone, which typically ranges from 1.8 to 2.1 g/cm^3. Additionally, the elastic modulus of pure Mg is around 45 GPa, which closely aligns with the 40 to 57 GPa range of human cortical bone. This similarity in elastic moduli suggests that using Mg in hard tissue engineering applications could minimize the risk of bone stress shielding and prevent bone resorption in the human body [15], [16], [17]. Consequently, magnesium-based metals mechanical properties to human cortical bone, coupled with its biocompatibility represent a novel class of metallic biomaterials position it as a promising material for the development of biodegradable biomedical implants [18], [19].

The major disadvantage of using Mg in many engineering applications is its low corrosion resistance, especially in electrolytic, aqueous environments where it rapidly degrades[20]. The medical application of Mg-based implants has been significantly limited due to the electrolytic aqueous environment of chloride-rich bodily fluids, with a pH typically ranging between 7.4 and 7.6. The rapid corrosion rate of Mg implants leads to a swift evolution of subcutaneous hydrogen gas and can create gas bubbles adjacent to the implants, leading to the separation of tissues and/or tissue layers. Mg high corrosion rate within the body may also restrict its usage in various applications due to the destruction of its mechanical integrity particularly in load-bearing applications [21], [22].

The body fluids consist of water, dissolved oxygen, proteins, and electrolytic ions such as chloride and hydroxide. In such an environment, magnesium, with an electrochemical potential of -2.37 V, is highly prone to corrosion, leading to the migration of free ions from the metal surface into the surrounding fluid environment. These ions have the potential to form various chemical species, including metal oxides, hydroxides, chlorides, and other compounds. From a thermodynamic perspective, assuming no barrier to the oxidation of the metal surface, the reaction would proceed rapidly, generating hydrogen gas and depleting the metal substrate surface. However, the electrochemical reaction also results in the migration of ions from the metal surface into the solution, where they form species contributing to the formation of an oxide layer adhering to the metal surface [23], [24].

The corrosion of Mg in an aqueous physiological environment can be expressed in the following equations, with the primary anodic reaction expressed by the partial reaction presented in equation (R1), while the reduction of protons is expressed by the partial reaction occurring at the cathode (R2).

$$Mg \rightarrow Mg^{2+} + 2e^{-} \qquad R\,1$$

$$2\,H_2O + 2e^{-} \rightarrow 2OH^{-} \qquad R\,2$$

Magnesium (Mg) exhibits high reactivity upon contact with water and transforms into magnesium hydroxide ($Mg(OH)_2$) (Reaction 3). In both acidic and neutral environments, this product is soluble, rendering it non-protective. The dissolution of the hydroxide layer raises the pH value, making it more difficult to dissolve further as magnesium hydroxide exhibits lower solubility in alkaline environment precipitating $Mg(OH)_2$. Within the human body, this undesired pH increase in surrounding tissues can also negatively impact cell viability. Furthermore, magnesium can also form MgO (Reaction 4), when in contact with O_2, which is more soluble, saturating the surface water layer and also promotes the precipitation of $Mg(OH)_2$.

$$Mg_{(s)} + 2\,H_2O_{(l)} \rightarrow Mg(OH)_{2(s)} + H_{2(g)} \qquad R\,3$$

$$2\,Mg_{(s)} + O_{2(g)} \rightarrow 2\,MgO_{(s)} \qquad R\,4$$

Solid state Magnesium and the $Mg(OH)_2$ layer formed on the metal surface is slightly soluble and reacts with Cl^- ions to produce highly soluble magnesium chloride and hydrogen gas (Reactions 5 and 6). When the layer fully covers and seals the metal surface, it forms a kinetic barrier or passive layer that physically limits or prevents further migration of ionic species across the metal oxide solution interface. The disappearance of the hydroxide layer due to chloride ions hastens the corrosion of magnesium and magnesium alloys. The corrosion of magnesium in an aqueous physiological environment can be described by the following equations.

$$Mg_{(s)} + 2Cl^{-}_{(aq)} \rightarrow MgCl_2 + 2\,e^{-} \qquad R\,5$$

$$Mg(OH)_{2\,(s)} + 2\,Cl^{-}_{(aq)} \rightarrow MgCl_2 + 2\,OH^{-} \qquad R\,6$$

The unfortunate complication arises from the fact that pure magnesium corrodes too rapidly in the physiological environment's pH range of 7.4–7.6 and high Cl^- content. As a result, it loses mechanical integrity before the tissue has adequately healed and produces hydrogen gas in the corrosion process at a rate too fast for the host tissue to manage. The other reaction product, magnesium hydroxide, exhibits partial solubility and in the body's high-chloride environment with a neutral pH, magnesium hydroxide converts to magnesium chloride ($MgCl_2$), which is fully soluble [17], [25], [26], [27].

Within the human body magnesium can also react in the presence of calcium, phosphate and carbonate ions, forming new substances. The main intermediate product deposits on the surface of Mg-based metals are: $Mg(OH)_2$, $MgCO_3$, $Mg_3(PO_4)_2$, $CaCO_3$, and $Ca_3(PO_4)_2$ [17]. Those are represented in the following reactions.

$$OH^- + HCO_3^- \rightarrow CO_3^{2-} + H_2O \quad \text{R 7}$$

$$Mg^{2+} + CO_3^{2-} \rightarrow MgCO_3 \quad \text{R 8}$$

$$H_2PO_4^-/HPO_4^{2-} + OH^- \rightarrow PO_4^{3-} + H_2O \quad \text{R 9}$$

$$Mg^{2+} + PO_4^{3-} \rightarrow Mg_3(PO_4)_2 \quad \text{R 10}$$

Regarding this work, the focus shifted mainly to Magnesium Hydroxide $Mg(OH)_2$, Magnesium Oxide (MgO) and magnesium phosphate $Mg_3(PO_4)_2$, as it was used a PBS (Phosphate Buffer Solution) to simulate the corrosion effects of Mg in the human body. These species can precipitate on the Mg surface due to their low solubility in physiological conditions. These precipitates can accumulate on the Mg surface, contributing to corrosion processes and affecting the performance of Mg-based implants or devices[28], [29], [30]. Several possibilities exist to tailor the corrosion rate of magnesium. Alloying is an important way to improve corrosion resistance and mechanical properties of magnesium. Protective coatings and surface treatments can also be applied to improve the corrosion resistance, biological compatibility, and biological activity of magnesium-based implants. Aluminum-containing magnesium alloys, particularly those in the AZ series (Mg–Al–Zn system), are widely used industrially. Alloying magnesium with aluminum results in reduced corrosion rates and increased tensile strength. Increasing the aluminum content from 1 to 5 wt.% promotes the formation of equiaxed grains and reduces their size. Additionally, alloying with zinc (up to 1 %) further enhances corrosion resistance and strength at room temperature[9], [26], [31], [32], [33], [34], [35], [36], [37].

AZ61A is a Magnesium based alloy, comprising aluminum (Al) at 6.5%, zinc (Zn) at 1.1%, and trace elements like manganese (Mn), nickel (Ni), and iron (Fe). Among these, aluminum serves as the principal alloying element, offering solid solution strengthening and enabling age hardening in magnesium alloys. The addition of zinc in minor quantities (1%) enhances the castability and corrosion resistance of magnesium alloys. With a specific gravity of 1.74 $g.cm^{-3}$ and tensile strength comparable to Al–Mg or Al–Mg–Si alloys, AZ61A is widely employed in structural applications due to its notable specific strength [38]. In Figure A-6-3 some mechanical properties of the AZ61A commercial alloy are shown. In general comparison magnesium alloys offers extremely close proprieties (Table 2-1) to those of natural bone, like density and elastic modulus[39] and with alloying elements present in the human body[40]. The unique properties of magnesium and its alloys make them ideal candidates for additive manufacturing in the realm of bioresorbable implants. Their biocompatibility, mechanical strength, and corrosion resistance offer promising avenues for further exploration and innovation in this field.

Table 2-1 Physical and mechanical properties of human bone, Mg and Ti alloy [39]

Properties	Natural bone	Magnesium	Titanium alloy
Density (g/cm^3)	**1.8-2.1**	**1.74-2**	**4.4-4.5**
Compressive Yield Strenght (MPa)	**3-20**	**41-45**	**110-117**
Elastic Modulus (GPa)	**130-180**	**65-100**	**758-1117**

2.2 Wire and Arc Additive Manufacturing (WAAM)

Additive manufacturing (AM) is an 3D printing manufacturing technique that constructs three-dimensional objects by sequentially adding thin layers of material, guided by computer control, and based on a digital model. This technology has gained significant academic as well as industry interest [41], [42] due to its ability to create complex geometries with customizable structures and material properties and several other benefits over traditional subtractive manufacturing[43], [44]. It presents several advantages for biomedical implants[45]. It allows for the fabrication of intricate geometries and internal structures, which are difficult to achieve with traditional methods. This capability enables the customization of implants to match patient-specific anatomies, enhancing their functionality, fit and fast prototyping[46]. AM also facilitates iterative design processes, reducing development time and production costs. Additionally, it minimizes resource waste by building parts layer by layer, using only the required amount of material[47] and enables the integration of multiple bioresorbable materials into a single component[48], offering opportunities for tailored properties and enhanced biocompatibility and potentially promoting tissue integration, vascularization, and osseointegration[49]. AM fundamentally relies on a heat source to melt the feed material, depositing it layer by layer to construct a predefined component. One of AM techniques is directed energy deposition (DED). DED additive manufacturing techniques employ thermal energy to melt and fuse materials during layer deposition. AM presents numerous advantages over traditional manufacturing methods, making it especially appealing for fabricating bioimplants with intricate geometries tailored to meet the specific requirements of individual patients [50].

Wire arc additive manufacturing (WAAM) is a type of directed energy deposition (DED) technique that utilizes wire feedstock instead of powder, simplifying the deposition process. In WAAM, an arc-generated plasma melts the wire, which is then deposited onto a substrate mounted on a manipulator. Unlike powder bed fusion (PBF) systems, WAAM allows for faster production with fewer post-fabrication processes. WAAM encompasses three wire-based welding methodologies: GMAW/MIG (Gas metal arc welding and Metal inert gas), PAW (Plasm arc welding), and GTAW/TIG (Gas tungsten arc welding and Metal inert gas). MIG is the most common in WAAM, where an electric arc is formed between the consumable filament and the metal workpiece. TIG and PAW utilize a non-consumable tungsten electrode, creating an electric arc with the workpiece. The possibility pf controlling the heat source is easier with a plasma arc compared to laser or electron beam sources, enabling better control overheat penetration depth. Wire-feed-based AM processes are also more user-friendly and less hazardous to health compared to powder-feed-based processes. Moreover, using wire as a material feed reduces the risk of contamination and oxidation, as wires have a lower surface-to-volume ratio than powders. Since WAAM does not involve recycling and reusing powder, it does not compromise the quality of fabrication [51]. Unlike more conventional methods like Selective Laser Sintering (SLS) and Electron Beam Melting (EBM), DED, particularly Wire Arc Additive Manufacturing, offers advantages such as high energy

efficiency, deposition rate, and cost-effectiveness[52], [53], [54], since wire feed orientation and welding parameters variations impact deposit consistency and process planning complexity[55], [56], [57]. The process, represented in Figure 2-1 is characterized by its simplicity, versatility, and advantages such as high energy efficiency, deposition rate, and cost-effectiveness, making it suitable for large-scale fabrication projects. WAAM allow to obtain fully dense parts with improved mechanical properties and has the potential to create dedicated biomedical-based substrates with potential application for biomedical implants[58], [59].

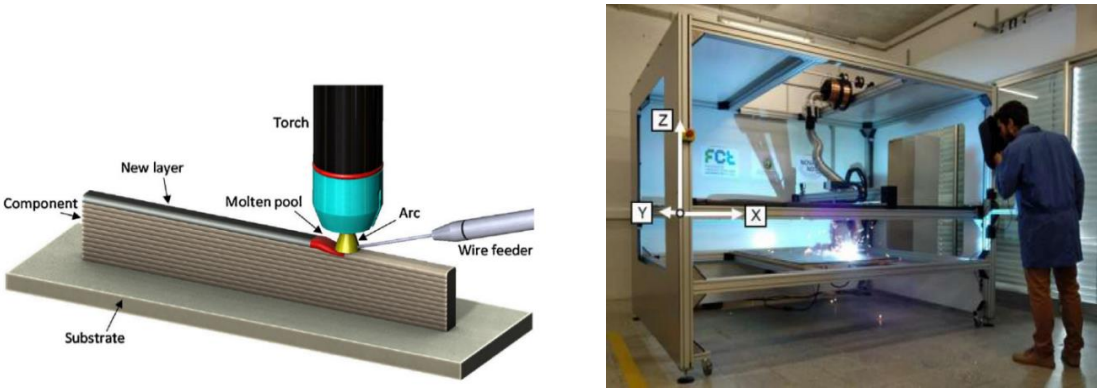

Figure 2-1 Illustration of the WAAM process (left) [60] and photo of the KEMPPI GMAW welding machine, model Pro MIG 501 used in this work [39] (right).

Magnesium-based biomaterials have unique properties that make them a natural choice for the development of biomedical implants, but due to their intricate shape and design, magnesium-based materials find it difficult to replicate the hierarchical structures of bones using traditional production processes like casting and other thermo-mechanical processing. Any complex geometry and nearly net shape of the components can be manufactured with additive manufacturing (AM), making Mg alloy with satisfactory compositional, microstructural, and design requirements[50], [61].

Overall, WAAM holds significant promise for the fabrication of Mg-based biomedical implants, but further research and development are needed to address the existing challenges and fully exploit its potential in the medical field.

2.3 Surface Functionalization

As stated above magnesium alloys usually corrode too quickly in the human body, but various advances have been made to retard its fast degradation, such as surface modification as it has been proved to be an effective method to make Mg degradation adjustable and improve biocompatibility. From the viewpoint of corrosion resistance, different coatings showed varied degradation behaviours, which is dependent on the formation technique [62], [63], [64].

The surface of an implant serves as the primary site for interactions between the implant and host cells or tissues. Surface-related attributes, including topography, energy, and chemical composition, play crucial roles in determining the implant's corrosion resistance, tissue integration, and overall

quality. By modifying the surface of the implant, it is possible to alter its final characteristics, ensuring that the surface provides distinct functions compared to the bulk implant. This surface modification enables tailored interactions with the surrounding biological environment, enhancing the implant's performance, corrosion resistance and compatibility with the host tissue [65], [66], [67], [68].

Nowadays, a variety of surface coating techniques, including electrochemical deposition, sol–gel, sputter deposition, spray deposition, biomimetic deposition[69], as well as coating materials, such as CaP[70], TiO_2, ZrO_2 and ZnO [71]have been proposed to induce favourable properties to the surface of the biomaterials. Surface functionalization of magnesium alloys improves the mechanical properties, biocompatibility and is one of the most effective ways to prevent corrosion [72], [73].

Our work focused on the surface functionalization of WAAM printed Mg-based AZ61A alloy substrates, using titanium dioxide (TiO_2) applied through electrodeposition, to protect the substrate surface and control magnesium corrosion and degradation rates.

2.3.1 Titanium Dioxide

Titanium dioxide (TiO_2) is a semiconductor metallic oxide and currently one of the most widely utilized materials due to its versatile properties and applicability across various industries including aerospace, automotive, electronics, construction, and healthcare [74]. In its pure form, TiO_2 exists as a white crystalline powder and is well known for its numerous advantages which include high photo-catalytic activity, long-term stability, photosensitivity, and antimicrobial properties [75], [76], [77], [78], [79], [80].

Research has delved into the biomedical applications of TiO_2, encompassing a diverse array of functional applications, including photodynamic therapy for cancer, cell imaging, biosensors for biological assays, and genetic engineering [81], [82]. Currently TiO_2 finds applications in numerous biomedical areas, including orthopaedics, dentistry, drug delivery systems, and tissue engineering as it promotes tissue integration and inhibits bacterial growth [77], [83]. In the context of bioresorbable implants, TiO_2 plays a pivotal role in the development of protective coatings for medical devices that serve as a protective barrier that enhances the biocompatibility and longevity of implant materials. By applying TiO_2 coatings through techniques such as electrodeposition, researchers can tailor the surface properties of bioresorbable materials to meet specific biomedical requirements, such as corrosion resistance, tissue integration, and controlled degradation rates [35], [84], [85], [86], [87], [88], [89], [90].

Its biocompatibility, chemical stability, and low toxicity make TiO_2 an ideal candidate for use in medical implants and devices that interact with biological systems. The main goal of our work was to deposit a TiO_2 coating on the AZ61A Mg alloy substrates to improve their degradation rate improving bioactivity, biocompatibility, and anti-bacterial performance.

TiO_2 can occur as one of three major crystal structures: the stable rutile (tetragonal, a = b = 4.584 Å, c = 2.953 Å), meta stable anatase (tetragonal, a = b =3.782 Å, c = 9.502 Å) and brookite (rhombohedral, a = 5.436 Å, b = 9.166 Å, c = 5.135 Å) [79], [91].

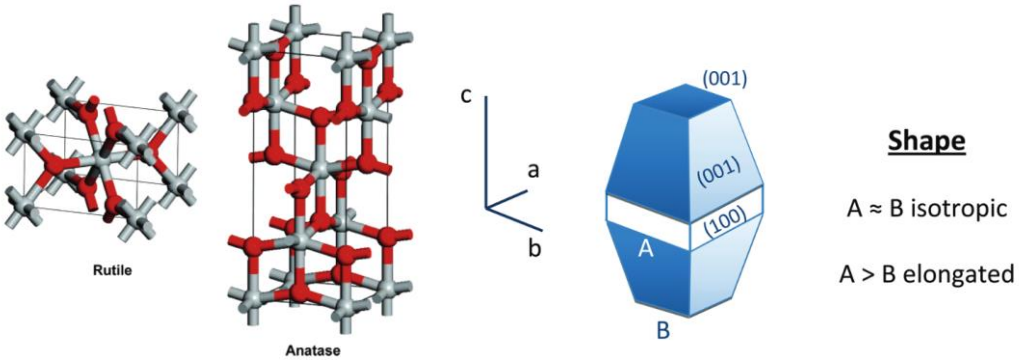

Figure 2-2 Bulk crystal structure of rutile (left) and anatase (right). Titanium atoms are gray, and oxygen atoms are red. (Obtained from [80] (left) and morphology of anatase nanocrystals (right) [92])

The brookite structure has received less attention in experimental investigations compared to rutile and anatase crystals. Figure 2-2 is a schematic representation of both crystal structures which can be characterized by chains of TiO_6 octahedra, wherein each Ti^{4+} ion is surrounded by a coordinated octahedron of six O^{2-} ions. The distinction between the two crystal structures lies in the distortion of each octahedron and the arrangement of the chains of octahedra. In rutile, the octahedron exhibits a slight orthorhombic distortion, while in anatase, the distortion is more pronounced, resulting in lower symmetry compared to orthorhombic. Anatase also features larger Ti-Ti distances and shorter Ti-O distances compared to rutile. In the rutile structure, each octahedron interacts with 10 neighbouring octahedra, sharing oxygen pairs along edges with two neighbours and sharing corner oxygen atoms with eight neighbours. Conversely, in the anatase structure, each octahedron interacts with eight neighbours, sharing both edges and corners with four neighbours.[69], [93]

These differences in lattice structures between the two forms of TiO_2 contribute to variations in mass densities, electronic band structures, surface structure, as well as bulk diffusion, surface transfer capability, and redox potentials. The distinctive properties of TiO_2 surfaces are also influenced by factors such as size and shape as rutile is considered the most stable phase for particles with sizes exceeding 35 nm whereas anatase is regarded as the most thermodynamically stable for nanoparticles with sizes below 10–20 nm.[82], [91] Anatase, with its higher surface area and greater number of surface defects, exhibits enhanced surface reactivity compared to rutile. This increased reactivity enables more efficient adsorption of molecules and ions onto the surface, making anatase TiO_2 well-suited for application as biomedical coatings to improve biocompatibility [94], [95], [96] [97], [98].

In the development of this project, it was intended to obtain anatase TiO_2 to understand the effects that this phase could have on enhancing the alloy surface properties enhancing biocompatibility, corrosion resistance and overall quality, always regarding potential health hazards related to TiO_2 [99], [100].

3
STATE OF THE ART

The goal of this chapter is to provide an overview of the recent development of bioresorbable implants, their production with WAAM method including their usage in the biomedical field. It is also presented a general overview of TiO_2 coatings to improve properties of the bioresorbable materials, particularly Mg-alloy biomedical implants.

3.1 WAAM of Bioresorbable Materials

In recent years, wire arc additive manufacturing (WAAM) has increasingly attracted attention from the manufacturing sector due to its ability to create large metal components with high deposition rate, low equipment cost, high material utilization, and consequent environmental friendliness. The origin of the WAAM process can be traced back to the 1925s when Baker proposed to use an electric arc as the heat source with filler wires as feedstock materials to deposit metal ornaments[3]. WAAM technology has seen a growing utilization, with researchers increasingly employing it for industry and academia in recent years[54]. However, there remains a scarcity of studies exploring WAAM's potential in the biomedical field, particularly in enhancing the quality of bioresorbable implants and foster advances in their potential applications. The study of Soni et al. (2022)[59] showcases the viability of using WAAM to fabricate dense Zn parts for potential biomedical implants. The technique allows to overcome chemical properties of Zn, enabling the production of defect free samples. The electrochemical response and degradation behavior of WAAM Zn samples closely resemble those of wrought Zn, with minimal differences observed. It also presented *in-vitro* cell studies indicate cytocompatibility referring that while WAAM presents a promising method for near-net-shaped implant fabrication, additional system modifications are needed to enable substrate movement for complex geometry. Singh et al. (2021)[53] stated to produce high-quality, defect-free components, it is crucial to align the performance features of the WAAM process with an understanding of material characteristics establishing a relation between WAAM parameters and material composition with produced samples microstructure. Similar observations had been made by Wu et al. (2018)[55] to whom research proposed a quality-based framework to address high-quality WAAM parts, promising wide application in the future, but stating that research is needed to

understand the underlying physical and chemical metallurgical mechanisms in WAAM for process optimization and control. Following studies, as the work of Dong et al. (2020)[101] revealed the production of WAAM Al-Zn-Mg-Cu samples with overall higher tensile properties. The research of Jafari et al. (2021)[57] addresses WAAM key aspects of heat input and management, emphasizing its impact on samples shrinkage, deformation, and residual stresses. It also discusses process planning considerations and outlines future research directions to improve component quality and accuracy, particularly for complex structures. Since then, consistent progress has been made on the development of this technology, particularly in the last years[52]. So far, metal additive manufacturing towards biomedical applications is primarily devoted to selected laser melting, which has some limitations especially in what concerns mechanical durability. WAAM allow to obtain from Mg-Based alloys, fully dense parts with improved mechanical properties and has the potential to create dedicated biomedical-based substrates with potential application for biomedical implants, in accord with Zeng et al. (2022)[37].

3.2 Bioresorbable Mg alloy in the biomedical field

In 2014, the studies of Chen et al.[24] approach the concept of smart implant, stating that significant advancements had been made in the development of magnesium-based alloys and understanding their *in-vitro* and *in-vivo* performance as potential "smart implants". The study found that magnesium alloys have advantages over Fe-based and Zn-based alloys for biodegradable implants as next-generation implants demand materials with appropriate mechanical properties, corrosion resistance, excellent biocompatibility, and bioactivity in the human body. Manivasagam and Suwas [27], in the same year, said that Mg and its alloys become natural biomaterials as elemental Mg is found in the human body in abundance. The authors also referred that the Mg mechanical properties are identical to the natural bone as well as being inherently bioresorbable. Riaz, et al. (2018)[34] stated that the use of Mg as an implant material reduces the risk of long-term incompatible interaction of implant with tissues and eliminates the second surgical procedure to remove the implant. Similar research was developed by May, et al (2020)[102]. Furthermore, Jamel et al. in 2022 found that Zn as an alloying element is highly effective in promoting alloy strength and biocompatibility, as Mg alloys have elevated corrosion rates, helping maintain mechanical integrity for designated healing times[26]. Recently Yi, et al. (2022) [58] research showed progresses in WAAM of Mg alloy, as it is anticipated to offer a novel approach for producing custom, intricate components, catering to the needs of different industries. This is directly relevant to our research question as it suggests that WAAM of Mg alloys provide a good option for biomedical implants, as a new approach in custom bioresorbable implant development. To improve those implants corrosion resistance as well as biocompatibility and adaptability, alloying[9], [26] and surface functionalization techniques[103] are investigated in recent years. In this document we will focus on surface functionalization starting by mentioning Tian and Liu, who in 2014[68] stated that surface modification, in comparison to alloy designs, offers a more cost-effective solution, provides flexibility in constructing

multifunctional surfaces, and avoids the need for adding potentially toxic alloying elements. Wan, et al. (2016)[72] showed that orthopedic implants surface modification through chemical deposition, with bioactive elements, adapts bioresorbable Mg alloys regarding biodegradation, biocompatibility, and mechanical loss property. In the review provided by Wieszczycka, et al. (2021)[36] surface functionalization techniques are described as a fundamental component in the development of smart materials in diverse industries, including the biomedical field. Furthermore, the work of Su et al. (2022) shows that nature inspired surface functionalization of metallic biomaterials improves overall biocompatibility and cell adhesion[104]. We follow the work of Peron, et al. (2020 and 2022)[88], [89] investigating the corrosion resistance enhancement of Mg alloys in Simulated Body Fluid when coated with sputtered TiO_2 layer, comparing its effectiveness with a similar coating produced via Atomic Layer Deposition (ALD), and naturally the potential that TiO_2 revealed attract our attention.

3.3 Titanium Dioxide Coatings

Titanium dioxide (TiO_2) is one of the commercially available antimicrobial coatings due to its stability, reactivity, reusability, durability, and low-cost. Due to its biocompatibility, mechanical strength, and strong resistance to corrosion, TiO_2 has numerous applications in the biomedical field [105]. In addition to the work of Peron, et al, mentioned above, Hou et al. (2020)[106] successfully deposited a TiO_2 thin film onto Mg-Zn alloy surface and according to their findings, the corrosion rate of Mg-Zn alloy was significantly reduced by the application of TiO_2 coating. Cell experiments further demonstrated the prepared coating's ability to improve endothelial cell viability and adhesion, significantly reduce hemolysis and platelet adhesion, and exhibit high biocompatibility. Park et al. (2017) [107] showed that by adjusting the nucleation growth time in the deposition process, the antibacterial activity against S. aureus could be improved. The production of reactive oxygen species explains TiO_2 antibacterial effect. Singh, et al. (2021) also stated that a TiO_2– Hydroxyapatite (HA) hybrid coating deposited on Mg alloy improved corrosion resistance[95]. Similar work and conclusions regarding corrosion resistance of a TiO_2 coating were obtained since White, et al (2013)[75], with several studies concluding the effectiveness of TiO_2 coatings[67], [109], [110]. Regarding our project the focus relay on the use of the Electrodeposition process [111], [112], [113].

Ribeiro, João (2022) research has been the foundation to this project. Set to produce Mg-alloys and determine the effect of a HA coating on the degradation of the material, it has concluded in a general way that the coating helped with the corrosion rate by slowing it down[39]. Following Ribeiro, João research, we aimed to functionalize WAAM printed Mg-alloy based implants with TiO_2 coating applied through Electrodeposition, to improve substrates corrosion resistance, biocompatibility, and electrochemical activity, potentially contributing to advances regarding bioresorbable implants.

4
MATERIALS AND METHODS

This work examined the Magnesium based AZ61A alloy with a titanium dioxide applied through electrochemical deposition (ED). The optimal ED parameters were determined and a microstructure study, in vitro degradation assessment, and electrochemical characterization using Cyclic Voltammetry (CV) were performed in the coated and uncoated alloys to assess efficacy with reference to alloy protection, corrosion resistance and biocompatibility. Optical Microscopy (OM), Scanning Electron Microscopy (SEM), X-Ray Diffraction (XRD), and Raman Spectroscopy (RS) were used to evaluate the samples. Additionally, the alloy was formed into printed substrates using the WAAM process, and the coated and uncoated substrates underwent the same prior testing.

4.1 WAAM of Biomedical Alloys

My work began with the study of a filament of commercial alloy AZ61A (Figure A-6-1). This Mg based alloy (92% Mg, 5.80% to 7.20% Al, 0.40% to 1.50% Zn, 0.15% Mn, 0.1% Si and traces of Cu around 0,05%, Fe and Ni (both 0,005%) was also used as feedstock in WAAM of different metallic substrates for further studies. In this project, additive manufacturing of Mg-based alloy components was conducted within the Mechanical Engineering Department. The primary objective was to obtain flawless parts using Wire Arc Additive Manufacturing (WAAM) techniques, followed by thorough characterization in subsequent stages. For the deposition process, a Gas Metal Arc Welding (GMAW) machine was utilized (Pro MIG 501 by KEMPP, showed in Figure 2-1), alongside a Pro MIG 3200 power source, also from KEMPPI.

Figure 4-1 Image of sample WAAM printed substrates of AZ61A alloy (left) and sliced WAAM printed wall (right).

The manufacturing parameters selected are detailed in Table A-1 and the obtained WAAM printed substrate wall is shown in Figure A-6-2, from which we prepare the study substrates displayed in Figure

4-1. The WAAM printed substrate walls were cut into pieces that best suited our needs. It was considered using a hacksaw but unable to produce a clean cut and a smooth surface, a Linear Precision Saw was used to cut the samples (Buehler Isomet 4000 showed in Figure A-6-38). The filament and the WAAM substrates were characterized and used in the following steps. All samples were polished with grit paper P1000 and washed with Ethanol prior to subsequential tests and ED process.

4.2 Electrodeposition Process

In this step it is described the preparation of the Electrodeposition solution used in the Titanium Dioxide coating, along with the two Phosphate Buffer Solutions, one acid and the other neutral pH, utilized in the *in-vitro* degradation and the electrochemical and corrosion tests.

4.2.1 TiO2 Electrodeposition Solution

We started the preparation of the deposition solution by choosing the most adequate precursor of TiO_2 and upon research it was chosen $TiCl_4$ (titanium chloride (IV) SIGMA-ALDRICH 189,68 g/mol; density of 1.728 g/cm^3 at 20 °C). To prepare hydrolysed $TiCl_4$, a controlled process was employed. A total of 22 mL (37,9360 g) of titanium tetrachloride ($TiCl_4$) was meticulously added dropwise to 78 mL of chilled water, maintained at approximately 4°C, within an ice bath. During the reaction, a distinct yellow precipitate initially formed, subsequently dissolving upon the addition of water, ultimately yielding 100 ml of 2M stock solution of hydrolysed $TiCl_4$ (or $TiCl_3^+$). [114] It is noteworthy that all chemicals employed in this process were of analytical grade and were utilized without further purification. Furthermore, the preparation of all solutions in this work adhered to exacting standards, employing Milli Q water (18.2 M$\Omega \cdot$ cm) to ensure precision and purity. Before initiating the electrodeposition process, two solutions were prepared, cetyltrimethylammonium bromide (CTAB - SIGMA-ALDRICH) and potassium nitrate (KNO_3 - SIGMA-ALDRICH), each at a concentration of 0.1 M and a total volume of 100 ml. For the CTAB solution, 36.4450 g were dissolved in 100 mL of Milli-Q water. In the case of the KNO_3 solution, 10.1100 g were weighed and dissolved in 100 mL of Milli-Q water. The final TiO_2 deposition solution was prepared as follows: 1 mL of titanium trichloride solution ($TiCl_3^+$) was mixed with 88 mL of deionized water. Following, 10 mL of potassium nitrate (KNO_3) solution was added to the mixture. Finally with the addition of 1 mL of CTAB, a 100 mL deposition solution was created, with each ED utilizing 50 ml. It is noteworthy that this solution was freshly prepared before each deposition and its pH was measured (pH 5-6). All mixing and dissolving stages were performed using a stirrer at 450 rpm, at room temperature.

4.2.2 Phosphate Buffer Solutions

In this step two Phosphate-Buffered Saline (PBS) solutions were prepared to simulate body fluids. To that effect, the pH values were around 7 and 5.5. To prepare the PBS of neutral pH, 4g of NaCl

(Sodium Chloride, SIGMA-ALDRICH, 99.5%), 0.7200g of Na_2HPO_4 (di-Sodium Hydrogen Phosphate Anhydrous, Pan-Reac AppliChem, _99.0%), 0.12g of KH_2PO_4 (Potassium Phosphate Mono-basic, SIGMA-ALDRICH, 99.0%) 0.1000g of KCl (Potassium Chloride, SIGMA-ALDRICH, 99.5-100%), and were dissolved and then diluted to 1L of mili-Q water. Solution pH was confirmed afterwards.

For the acid PBS two solutions were prepared. In the first one we dissolved 13.1200g of KH_2PO_4 in 964 ml of mili-Q water. The second one consisted of 1.2892g of Na_2HPO_4 dissolved in 36 ml of mili-Q water also. These 2 solutions were then mixed to obtain a total volume of 1 L of PBS with a pH 5.5. All PBS solutions were prepared using a stirrer ate 450 rpm, at room temperature.

4.3 Electrodeposition of Titanium Dioxide

Electrodeposition is commonly employed to produce a coating, usually metallic, on a surface by the electrochemical reduction at the cathode. The substrate to be coated is used as cathode and immersed into a solution which contains a salt of the metal to be deposited. The metallic ions are attracted to the cathode and reduced to metallic form, creating a coating on it. The relevant literature reveals that cathodic electrodeposition leads to better results in the production of coating layers than chemical conversion layers, however, careful adjustment of the parameters is necessary. Sometimes there are traces of the substrate mixed into the coating forming new phases, such that the coating is not purely by deposition but also to some extent by conversion at the interface [69], [72]. To overcome that and enhance the surface adhesion strength, structural capability and biocompatibility, incorporation of Metallic oxides is one of the suitable choices as several have been reported to modify surface properties of the coatings successfully[115], [116], [117], [118], [119], [120]. The main advantage in ED is the control of film thickness, morphology, and composition through electrolyte quantity and concentration, deposition current and applied potential. It is noteworthy that the protocol employed for this electrochemical deposition procedure was based on a compilation of well-established articles and research studies[66], [112], [121], [122]. In Figure 4-2 it is represented a schematic of the ED process.

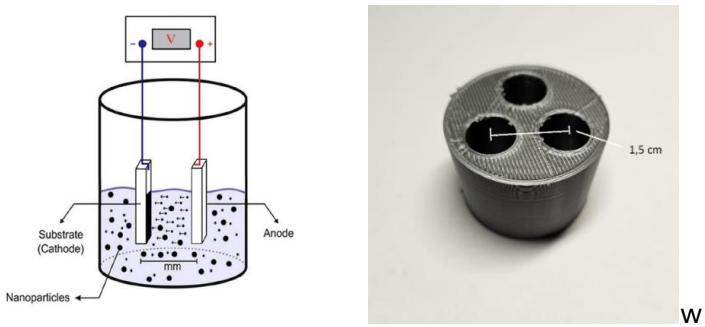

Figure 4-2 Schematic representation of the ED process (obtained from[39]) (left), and custom plastic lid (right).

An electrochemical setup was employed, utilizing a voltage source in conjunction with a Graphite rod serving as the counter electrode (anode). The working electrode (cathode) consisted of either the

AZ61A commercial alloy filament or the substrates produced via Wire and Arc Additive Manufacturing (WAAM). Before the ED process, a custom plastic lid (Figure 4-2) featuring three evenly spaced holes separated by 5 mm was printed. The centres of these holes were situated 1.5 cm apart, with the chosen lid having a diameter of 33 mm and 25 mm in height. This lid (detailed in STL presented in Figure A-6-6) was fabricated using an Ender-5 3D printer, serving the critical purpose of maintaining electrode distance throughout the entirety of the experiments, as any deviation in this factor could potentially impact the experimental outcomes. The exposed area of WAAM substrates in ED was approximately 3.5 cm^2.

The initial phase of experimentation involved the use of the commercial AZ61A Magnesium alloy as the deposition substrate. Electrodeposition was conducted on AZ61A filament at a potential of 0.5 V for a duration of 60 minutes. Additionally, an electrodeposition test at 6 V for 60 minutes was carried out for comparative analysis. Following this preliminary approach, the potentials of 1 V, 1.5 V, and 2 V were applied for deposition times of 15, 30, 45, and 60 minutes. All ED processes utilized the deposition solution detailed in section 4.2.1 and present deposition current values around 1 mA. Post-deposition, the substrates underwent a drying process at room temperature spanning 3 hours, followed by annealing at 450°C for a duration of 30 minutes in an oven. After a gradual cooling process overnight, the resulting samples were deemed ready for utilization in the following phases of experimentation. Following the exhaustive series of tests conducted on the commercial alloy, the optimal coating parameters were ascertained and subsequently applied to the materials produced via the Wire and Arc Additive Manufacturing (WAAM) process. Figure A-6-5 shows the ED process and electrode detail.

4.4 Microstructure Analysis and Characterization

Following the Electrodeposition of TiO_2 on the commercial AZ61A alloy an analysis of the substrates was conducted. Therefore, a macroscopical observation of the obtained coatings was completed with Optical Microscopy (Leica DMi8), SEM imaging, Raman Spectroscopy and XRD. The samples were analysed before and after any follow up test regarding corrosion, degradation, and electrochemical performance.

4.4.1 Chemical Characterization with Raman Spectroscopy

Raman Spectroscopy is an optical and vibrational spectroscopic method, which is frequently used for tissue characterization and based on the Raman effect, which asserts that when light with a wavelength of between 750 and 850 nm is impacted on a tissue, its molecules will reflect the light with a specific wavelength. It is feasible to identify the molecular structure and content of the tissue using this technic, enabling the identification of numerous chemical components[123], [124], [125]. A Micro Raman Witec Alpha 300RAS equipped with a 633 nm wavelength laser was used for the chemical characterization of the coated substrates.

4.4.2 Structural and Morphological Characterization with SEM and XRD

The microstructure and surface morphology of the samples were examined by Scanning Electron Microscopy and X-Ray Diffraction, after ED process. Scanning Electron Microscopy (SEM) is a useful method for examining surfaces. It is a morphological analysis that produces detailed pictures and is frequently used for contaminant detection and defect characterization. Photons and electrons are emitted as the electron beam scans the surface and interacts with the substance. A specialized detector that gathers these particles gathers data about the surface. An image of the sample is created after the beam has covered the entire surface. The equipment used for the SEM analysis was a Hitachi SU3800 [68], [79], [91], [126], [127].

X-Ray Diffraction (XRD) is a non-destructive technique used to describe the crystalline structure of a sample, providing data on structures, crystal orientation and defects, phases, and average grain size, allowing identification based on the sample diffraction pattern. XRD measure the intensities and scattering angles of the X-rays that leave a material after the bombardment with incident X-rays at certain angles, producing the XRD peaks. The atomic positions within the planes determine the peak intensities, and so the XRD pattern is characterized by the periodic atomic arrangements of the material. In addition, XRD provides information on how internal stresses and flaws cause a less than ideal structure. XRD was performed using the X-ray diffractometer PANalytical's X'Pert PRO MRD and the diffractogram measurements were carried out from 10° to 90° (2Θ), with a scanning step size of 0.0167°. The radiation source was a monochromatic Cu Kα with wavelength 1.540598 Å[69], [128], [129], [130].

4.5 *In-vitro* Degradation Tests

In-vitro degradation of the substrates was performed by immersion testing under static simulated physiological conditions. Its objective was to determine the rate of degradation that the AZ61A alloy, along with the protective effect that the TiO_2 coating could reveal. It was compared an uncoated sample, a coated but not annealed sample and an annealed sample of the commercial AZ61A alloy. It also used a Titanium based alloy, applied frequently in the biomedical field, to compare degradation results. For each of these substrates, a total of eight samples were prepared, with each sample cut to a length of approximately 3 cm. To simulate physiological conditions, half of the samples were immersed in a PBS with a pH of 7.4. and 4 were submerged in a solution with a pH of 5.5. Each sample was added to a test tube, immersed in 5 ml of the respective PBS, and left in a water bath at 37 ºC. All samples were weighted at the beginning of the test and again once a week, upon rinsing of the PBS with distilled water and before returning the samples to the tubes with fresh PBS solution. The degradation tests lasted four months. With those values it was intended to determine evidence of mass loss through degradation *in-vitro*, and the protective effects of TiO_2 coating in that regard.

4.6 Electrochemical Characterization through Cyclic Voltammetry

Cyclic voltammetry (CV) is widely regarded as one of the most versatile electroanalytical techniques for investigating electroactive species. Its adaptability and ease of use have led to its extensive application across electrochemistry, inorganic chemistry, organic chemistry, and biochemistry. Often employed as the initial experiment in electrochemical studies, CV allows for the rapid observation of redox behaviour across a broad potential range. The resulting voltammogram, akin to a conventional spectrum, provides valuable insights into the system's behaviour as a function of an energy scan[131], [132].

CV involves cycling the potential of an electrode submerged in a solution while measuring the resulting current. The potential of the working electrode is controlled relative to reference electrodes such as a Saturated Calomel Electrode (SCE) or a silver/silver chloride electrode (Ag/AgCl). The potential applied across these electrodes can be considered an excitation signal. In CV, the excitation signal typically takes the form of a linear potential scan with a triangular waveform, as depicted in Figure 4-3, along with an illustration of the CV setup. This triangular excitation signal sweeps the electrode potential between two values, known as the switching potentials, versus Reference Electrode, after which the scan direction is reversed, resulting in a positive scan back to the original potential. Figure A-6-39 details the 3-electrode set-up used in this research.

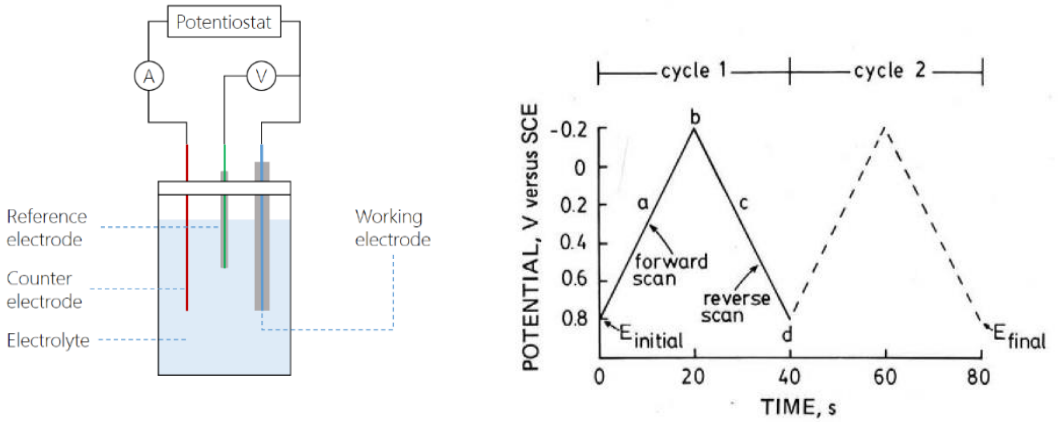

Figure 4-3 Illustration of the Cyclic Voltammetry process (obtained from [39]) (left) and typical excitation signal for cyclic voltammetry - a triangular potential waveform with switching potentials at 0.8 and -0.2 V versus SCE (obtained from [133]) (right).

A cyclic voltammogram is a graphical representation of current, responsabile for oxidation and redution reactions in the solution and working eletrode, plotted against potential. Since the potential varies linearly with time, the horizontal axis can also be interpreted as a time axis. By measuring the current at the working electrode throughout the potential scan, CV helps assess ongoing redox reactions potentials. To simulate human body conditions, tests were conducted in PBS of pH 7 and 5.5.

In electrochemical tests a potentiostat Gamry Instruments - Interface 1010 E was used. Applying a three-electrode cell configuration, the WAAM substrates and AZ61A filaments under examination

served as the working electrode, a graphite rod was used as the counter electrode and an (Ag/AgCl) silver electrode as the reference electrode. Throughout the project, an Ag/AgCl (silver) electrode was employed as the reference electrode, documented as a stable reference electrode (vs SCE) in electrochemical experiments[133]. To simulated physiological fluid, CV tests were conducted in the neutral and acid PBS, beginning with Open Circuit Potential tests in TiO_2 coated and uncoated AZ61A alloy, in neutral and acid PBS. Tests were conducted for 4000 s. Following previous research [39], the CV experiments were initiated by performing an initial CV, in neutral PBS, scanning both ways between -2 V and 2 V, employing a scan rate of 50 mV/s and a maximum current of 0.2 A. Concerning the scan rate was important in the study to define the value that best fit because high values could lead to not detecting all redox reactions and low values could allow secondary reactions which leads to the loss of substrate. This initial CV cycle was conducted for a total of 5 cycles. During this phase, we closely monitored the electrochemical reactions occurring at the material's surface. Notably, the formation of hydrogen bubbles was observed as indication of ongoing reactions. Consequently, we conducted an extended CV test, comprising a total of 50 cycles. By the end of the 50 cycles, we noted that the current had substantially decreased and was approaching zero. This significant decrease in current indicated that the material's electrochemical reactions had nearly ceased. Building upon the insights gained from the 50-cycle CV test, we adjusted our approach. Subsequent tests were conducted at 20 cycles, scanning both ways between -2 V and 2 V, employing a scan rate of 50 mV/s and a maximum current of 0,2 A. To ensure electrode distance, we applied the lid developed in Ribeiro, João [39] which maintained the three electrodes at 1.5 cm of each other.

To ensure standard patterns across experiments it was imperative to maintain a consistent surface area of material immersed in the solution and ensure the same volume of solution in each experiment. To achieve this, and like ED process, 50 ml of (PBS) for each test was used and the length of the material immersed was approximately 3 cm in all experiments (Surface area approximately 3.5 cm^2). The electrochemical process was conducted in both PBS (acid and neutral), using TiO_2 coated and uncoated WAAM printed AZ61A substrates and filaments, to evaluate their effect on surface protection and degradability rate. To better understand the corrosion effects on the substrates surface, SEM images were obtained after each CV, and mass loss was registered, by weighting the substrates before and after each CV. Figure A-6-39 shows the 3 electrode set-up, with Reference Electrode (A), Working Electrode (B) and Counter Electrode (C) [134], [135]. Electrochemical tests allowed us to better understand the influence of TiO_2 coatings in the well documented corrosion rate of magnesium and magnesium-based alloys[20], [73], [88], [89], [95], [136].

5
RESULTS AND DISCUSSION

In this chapter, the results of the project along with its discussion will be explained. Set as the main goal the electrodeposition of a TiO_2 coating on WAAM printed AZ61A alloy substrates, here we present the ED optimization process and the base it set for the TiO_2 coated WAAM printed substrates evaluation. The substrates characterization was possible through Optical Microscope imaging, SEM, XRD and Raman Spectroscopy. This section also shows coating effects in mass variation and corrosion evaluation upon submission to *in-vitro* degradation tests, as well as its electrochemical activity through cyclic voltammetry tests, both in neutral and acid PBS.

5.1 Electrodeposition of TiO_2

At the initial phase of the study, the electrodeposition (ED) process of TiO_2 was undertaken to explore and understand the critical parameters regarding this process, aiming to potentially establish the most effective conditions for achieving a homogeneous and high-quality TiO_2 coating on the AZ61A Mg-based biomedical alloy, as Mg alloys coatings adhesion is an issue. The evaluation of different precursors for TiO_2 formation, comparing $TiCl_4$ to alternative candidates, was carried out to determine the most suitable precursor for the electrodeposition process while several parameters were systematically researched. The concentration of Ti in the deposition solution, the distance between electrodes, applied voltage, time intervals, deposition current, and choice of a graphite rod as a counter electrode were carefully chosen due to lack of understanding of their individual and collective impacts on the TiO_2 coating quality. Prior to each electrodeposition process, the substrates underwent thorough cleaning with ethanol to ensure a pristine surface for coating. Figure A-6-4 shows an Optic Microscope image of the uncoated AZ61A.

Following the study of An et al. (2004)[137], an electrodeposition solution composed of $TiCl_3^+$ (0.01 M), KNO_3 (0.1 M), and CTAB (0.01 M) was initially employed. While this solution demonstrated promise, alternative solutions based on the work of Lockande et al. (2005)[112], which suggested the use of HCl and EDTA, were also explored. However, upon deposition, it was observed that the latter

solution led to the corrosion of the AZ61A Mg-based alloy filament. Subsequently, the deposition solution comprising KNO_3 and CTAB, which was determined to have a pH around 5, was reinstated[112]. Exploratory electrodeposition trials were started with its initial tests carried out at 2 V for a duration of 30 minutes. During this process, the formation of bubbles within the solution was observed. Examination of the substrate following deposition revealed the presence of a seemingly uniform white layer. A subsequent trial was conducted at 6 volts (Figure A-6-10), but optical microscopic imaging disclosed an uneven coating characterized by numerous clusters and a notably rough surface. At 6 volts, the deposition current would rapidly decrease to zero at around 1.9 to 2 V. Based on the outcomes of these preliminary trials, the optimization of the electrodeposition process was carried out by investigating the most favourable combination of voltage and deposition time. Electrodeposition trials were conducted at 0.5, 1, 1.5, and 2 volts, each for durations of 15, 30, 45, and 60 minutes. The ED at 0,5 V presented an extremely uneven surface and the voltage was discarded (Figure A-6-9). It was also noted that the ED at 1V could sustain an apparently robust and homogeneous coating (Figure A-6-8 and Figure A-6-7). Optical microscopy was employed to scrutinize the quality of the coatings. In the appendix section it is possible to represent a summary of the optical microscope images obtained to complement the visual appreciation of the TiO_2 coatings, observed in Table A-2, Table A-3, Table A-4 and Table A-5.

The comprehensive optimization efforts revealed that 45 minutes of electrodeposition at 1 volt (Figure 5-1) yielded the most desirable results for coating the commercial AZ61A alloy. This configuration produced a uniform and TiO_2 coating, and represented a significant milestone in this work, setting the stage for the WAAM printed substrates ED process. The same process was applied to a titanium based alloy. All following ED processes were performed at 1V for 45 minutes, with 1.5 cm between electrodes and 50 ml of deposition electrolyte. To note that the electrodeposited substrates underwent a meticulous post deposition treatment process. Solutions for coating the electrodes with films of TiO_2 were freshly prepared each time revealing a transparent appearance at room temperature. All the characterization analyses presented were conducted using samples with TiO_2 coating (Figure A-6-36), and uncoated (Figure A-6-37) but unannealed samples were also in degradation tests and XRD.

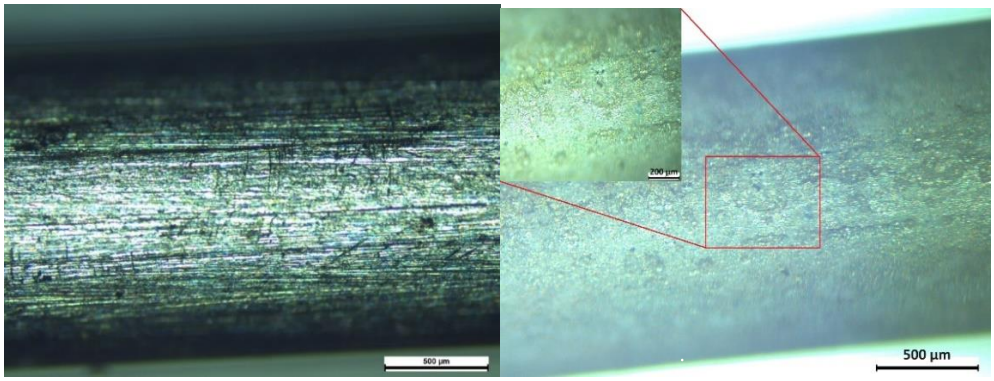

Figure 5-1 Optical microscope image of uncoated AZ61A commercial alloy (left) and with TiO_2 annealed coating.

To note that the electrodeposited substrates underwent a meticulous post-deposition treatment process to fully achieve crystal phase of anatase. Solutions for coating the electrodes with films of TiO_2

were freshly prepared each time revealing a transparent appearance at room temperature. All the characterization analyses presented were conducted using the annealed samples. Based on these observations, a plausible mechanism for the electrochemical deposition is proposed, emphasizing the essential role of $NO3^-$ ion reduction at the initiation stage of electrodeposition.

$$TiCl_3^- \rightarrow Ti^{4+} + Cl^- \quad \text{R 11}$$

$$KNO_3 \rightarrow K^+ + NO_3^- \quad \text{R 12}$$

$$NO_3^- + H_2O + 2\,e^- \rightarrow NO_2^- + 2\,OH^- \quad \text{R 13}$$

$$TiO^{2+} + 2\,OH^- \rightarrow TiO(OH)_2 \quad \text{R 14}$$

$$TiOH^{2+} + 2OH^- \rightarrow Ti(OH)_3 \quad \text{R 15}$$

The $Ti(OH)_3$ is finally converted to TiO_2 upon drying and annealing process. Solutions for coating the substrates with TiO_2 were prepared for each ED, at room temperature. It was observed a thick layer formed on the filament surface, showing a grey colour and being susceptible to peeling off. After annealing, the surface showed a tendency towards a whiter colour, with a firm and thick layer. SEM images are presented in section 5.2.3 to help understand the surface morphology. The presence of CTAB plays a crucial role in promoting coating formation, as evidenced by the increased thickness of the TiO_2 film[138], [139]. The accelerated rate of film formation with CTAB is likely attributed to reduced electrostatic repulsion of NO_3^- ions by the adsorbed CTA^+ at the cathode. This diminished repulsion of NO_3^- ions leads to their higher concentration at the electrode surface, facilitating faster nitrate reduction (R15) and ultimately resulting in thicker film growth. The adsorption of CTA^+ onto the negatively charged TiO_2 surface is supported by recent observations[140], aligning with the electrostatic interaction scheme proposed by An et al. for the self-assembly reaction involving various surfactants and inorganic species. Thick anatase phase coatings were intended as the project developed, which employing CTAB proprieties allowed[137], [141], [142], [143], as the following sections will present.

The annealing process helps in crystallizing the deposited TiO_2 layer by densifying the film, reducing defects, and improving the uniformity of the coating. This is crucial for ensuring the desired properties and functionality of the TiO_2 layer, such as corrosion resistance and adhesion. Depending on the annealing temperature and duration, different crystal structures such as anatase, rutile, or brookite may form. The choice of crystal structure can significantly impact the properties of the TiO_2 layer, including biocompatibility, morphology, and thickness. Annealing can also affect the composition and chemical states of the TiO_2 layer leading to the removal of residual impurities or organic residues from the electrodeposition process, resulting in a purer TiO_2 layer with enhanced chemical stability. It can also improve its mechanical properties such as hardness and abrasion resistance, which is particularly important for ensuring the long-term durability and performance of the TiO_2-coated substrate in practical applications[144]. A preference exists for anatase phase over rutile to achieve a larger surface area per unit volume, owing to the larger dimensions of rod-shaped rutile particles compared to the spherical shape

of anatase particles. It was observed that after the ED process presented a light grey surface, which turn white upon the annealing process, an indicator of this crystal phase. Also due to the Ti^{3+} defects in the dissociative adsorption of water onto TiO_2 surfaces and the influence of hydroxyls on the biological behaviour of titanium, controlling the density of surface defects through annealing is proposed to enhance implant interactions. Experiments revealed that low-temperature annealing can enhance anatase formation and create a controlled number of Ti^{3+} defects as high concentration of Ti^{3+} defects is associated with surface porosity. Such surfaces, characterized by high hydrophilicity and microporosity, are expected to facilitate interactions with surrounding tissue [144], [145].

5.2 Analysis and Characterization

Raman spectroscopic analysis was performed on sample surfaces to characterize their chemical composition. Raman spectrum of the TiO_2 coating, after annealing is depicted in Figure 5-2. Different vertical scales are presented, resulting of data analysis to offer better insight regarding the characteristics of observed peaks.

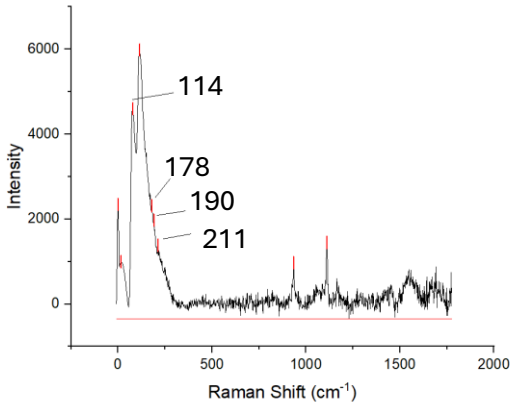

Figure 5-2 Raman Spectroscopy of the WAAM printed AZ61A substrates coated with TiO2.

Anatase phase of TiO_2 can be sensitively identified by Raman spectroscopy based on their characteristic peaks. The anatase phase shows major Raman bands at around 144, 197, 399, 515, 519 and 639 cm^{-1}.[125], [146] These bands can be attributed to the six Raman-active modes of anatase phase with the symmetries of E_g (Symmetric stretching mode ν 1), E_g, B_{1g} (Asymmetric stretching mode ν 3), A_{1g} (Symmetric stretching mode ν 1), B_{1g}, and E_g, respectively. Additionally, the band at 144 cm^{-1} is the strongest one for the anatase phase. Figure 5-2 shows the Raman spectra of WAAM printed TiO_2 calcined at 450 ºC with excitation lines at 633 nm. Our main related Raman bands are located at 114, 190 and 211 cm^{-1} (O-Ti-O bending-type vibrations) which can be associated bibliographically to the characteristic E_g peak of anatase. It has been known that the E_g peak is mainly caused by symmetric stretching vibration of O–Ti–O in TiO_2, the B_{1g} peak is caused by symmetric bending vibration of O–Ti–O, and the A_{1g} peak is caused by antisymmetric bending vibration of O–Ti–O [123], [124]. It's noteworthy, as reported

in the literature and confirmed in our study, that electrochemical deposition consistently produced anatase, in TiO_2 coating preparation.

Bands around 934 cm^{-1} and 1052 cm^{-1} were markedly observed in samples, which could be attributed to MgO (υ 4), as well as a peak at 1800-1900 cm^{-1}, characteristic of the presence of $Mg(OH)_2$ and Mg, but overlapped with other components presence. In addition, the band around 1500 cm^{-1} could be associated with carbonates due to CO_2 and atmosphere conditions [147].

However, Raman spectroscopy may not be the most appropriate test to evaluate a coating of TiO_2 on a magnesium based biomedical alloy, as show in peak overlap at 50-250 cm^{-1}. Being a surface-sensitive technique, the Raman signal obtained from the TiO_2 coating may be influenced by the underlying Mg-based alloy substrate and corrosion products, which our patterns could potentially confirm. If the TiO_2 coating is thin or if there are substrate roughness variations, it may be challenging to obtain representative information about the coating's properties throughout its entire thickness as it is difficult to distinguish between signals arising from the coating and those originating from the substrate background signals or overlapping peaks or increased background noise, as shown in Figure A-6-13.

If the TiO_2 coating exhibits chemical heterogeneity or if there are impurities present, it can complicate the interpretation of Raman spectra and lead to ambiguous results. Surface roughness of the sample can affect the Raman signal intensity and may introduce variability in the measurements. If the TiO_2 coating exhibits uneven thickness or rough surface morphology, it can also impact the reproducibility and reliability of Raman spectroscopy results and require further investigation[124], [125].

Overall, while Raman spectroscopy is a powerful technique for characterizing molecular structure and composition which allowed us to confirm anatase presence, its limitations in probing thin coatings, susceptibility to substrate interference, and sensitivity to sample surface properties make it less suitable as the sole method for evaluating TiO_2 coatings on Mg-based biomedical alloys. Complementary techniques such as X-ray diffraction (XRD) and scanning electron microscopy (SEM), may provide more comprehensive insights into the TiO_2 coating's crystalline structure and surface morphology.

5.2.1 XRD Analysis

For a structural analysis, X-ray diffraction (XRD) tests were conducted to obtain information about the crystalline lattice, surface structure, and overall confirm the presence of TiO_2 anatase. Regarding biocompatibility, anatase crystalline structure allows an increased surface area coating, to which a higher effective electrochemical substrate is associated. Figure 5-3 analyses an AZ61A alloy WAAM printed substrate after the ED process at standard parameters of 1 V for 45 minutes followed by annealing process mentioned in section 5.1. In the graph, it is possible to observe the values of 2Θ, in degrees, associated with the respective peaks.

In the diffractogram it is possible to observe 4 main diffraction peaks at 2 theta values of 20.97°, 36.93°, 48.21°, and 82.27°. It is also possible to observe that the peaks below 25° presented higher

FWHM values. In XRD, FWHM stands for "Full Width at Half Maximum." It refers to the width of a peak at its half maximum intensity value and is commonly used to characterize the crystallite size and the degree of crystallinity of materials. A narrower FWHM indicates sharper and more well-defined peaks, which typically correspond to larger crystallite sizes and higher degrees of crystallinity. Conversely, a broader FWHM suggests smaller crystallite sizes or greater levels of disorder or strain within the crystalline lattice. We also observed an increase in baseline pattern between 2 θ values of 10º-30º typically indicating an increase in amorphous or disordered phases in the sample.

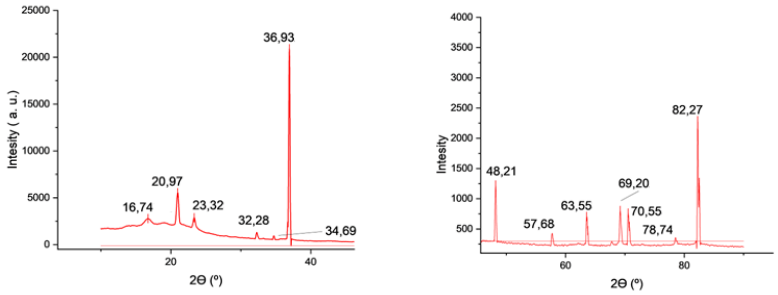

Figure 5-3 XRD Peak detail of WAAM substrate with annealed TiO2 Coating

Besides crystal size possible reasons for this observation are texture in the material, because diffraction peaks become sharper when the crystallographic planes are aligned, and the presence of amorphous or poorly crystalline phases of corrosion byproduct in the sample. Surface roughness and oxidation of the sample, especially in the lower 2Θ range, as well as residual stress and instrumental artifacts such as detector noise or background scattering can also contribute to baseline increase and peak broadening.

It is important to mention that after the ED followed by annealing, it was expected to observe evidence of TiO_2 anatase in the substrate coating. Additionally, it was also expected to find Mg (or similar regarding the AZ61A substrate) or traces of MgO and $Mg(OH)_2$ and eventually corrosion products. After bibliography review all diffraction patterns were associate to the respective Miller indices. It began by analysing patterns related to the AZ61A alloy and anatase TiO_2.

The main peak 2Θ of 36,93º is associated with the HCP (Hexagonal Close Packed) structure of Mg 101 (Magnesium (Mg): JCPDS card number 05-0664)[148]. However, we must address the works of Bagheri et al (2013)[149] where it is stated that TiO_2 anatase 103 shows diffraction peaks at 2Θ of 37,05º. Recalling the 7% presence of Al in the AZ61A alloy and the presence of anatase 004 at 2Θ of 36,7º suggested by Peng, Pi (2018)[150], it is possible that the peak intensity could be influenced by all 3 phases, which further studies may enlighten regarding peak overlap. Several works on XRD patterns of Magnesium and AZ61A alloy allowed us to identify peaks at 57,69º and 63,55º as Mg HCP influence [148], [151] , with values of peak at 32,29º and 34,69º (M1 and M2 in Figure 5-4) well documented in the AZ61A alloy XRD characterization studies[152], [153], [154], [155].

Subsequently, it was observed several peaks associate with anatase TiO_2 diffraction patterns. Upon bibliography review we were able to associate peaks at 2Θ values of 48,21º, 69,2º, 70,56º and 82,27º with the 200, 116, 220 and 224 crystalline structures of anatase TiO_2, respectively (Anatase XRD JCPDS Card no. 78-2486, no. 84-1286, no. 00-001-1272, and no. 88-1175) [69], [128], [130], [149], [156]. Our main objective at the beginning of the test was to confirm the presence of the anatase phase of TiO_2. By demonstrating the presence of anatase TiO_2, it was shown that the ED process allows for the creation of a stable and thick enough surface to identify the different anatase phases. Upon observing the peak corresponding to the A116 plane, we found a larger FWHM than expected, especially when compared to the other anatase planes. Coincidentally, several studies show rutile TiO_2 diffraction patterns at these 2Θ values [93], [157]. A probable amorphous or mixed-phase structure may contribute to a broader peak, to which inconclusive effectiveness may be ascertain. However, the intensity of the A224 anatase phase and narrowness of the remaining planes, particularly the A200 plane, as highlighted in various studies[98], [137], [158], [159], [160], helped understand the effectiveness of the ED process regarding the desired TiO_2 phase. There are no peaks from other phases observed, an indication of the deposition crystals high purity. The sharp peaks observed from the XRD pattern indicate that the TiO_2 particles have a consistent grain size.

It was then time to evaluate the pattern for 2Θ values below 30º, as a broad hump was observed in the baseline encompassing 3 distinct peaks at 16,75º, 20,97º and 23,33º. Since the reviewed bibliography indicates no significant peaks for either Mg or anatase in 2Θ values below 25º, investigation follow to the probable reaction or corrosion products that could remain in the TiO_2 coating after annealing at 450 ºC. Since the annealing process temperature promotes the formation of TiO_2 anatase crystals, we decided to compare to MgO (R4) and $Mg(OH)_2$ (R3) diffraction patterns. Several works detail a common increase in the XRD baseline within these 2Θ values when in presence of magnesium oxides and hydroxides, influenced also by the annealing process or its parameters. Through the study of Umaralikhan, et al. (2018)[129], [161], [162], [163], [164], [165], where MgO diffraction analysis was obtained, we were able to associate the obtained peak at 2Θ of 16,75º with this substance. Yet it is also noticeable the extremely high FWHM value, which led us to conclude that even though MgO is present in pure form, it could also be in a mixed phase structure, amorphous in nature or influence by the general increase of artifacts in lower 2Θ values in the XRD. The research of Sugapriya, et al. (2013) [144] conclude that increasing annealing temperatures originated a decreasing of the hump below 2Θ values of 30º. However, it also states that increasing annealing temperatures favors the formation of rutile phase, which overall was not desired for our studies. Sundrarajan et al. (2012) [166] obtain similar results while evaluating MgO under different annealing temperatures. With the XRD patterns obtained by Giorgi et al. (2005) while characterizing $Mg(OH)_2$ we were able to associate the peak at 2Θ of 20,97 with the 001 plane[167]. Since no other peaks evidenced XRD patterns of $Mg(OH)_2$ aligned with the research, we began to evaluate the possible presence of Titanium deposition byproducts. Conclusions are summarized in Figure

5-4. We show two scales in results to demonstrate Mg peak intensity when compared to other substances. Peaks 1 and 2 in Figure 5-4 could potentially be associated with anatase and Mg.

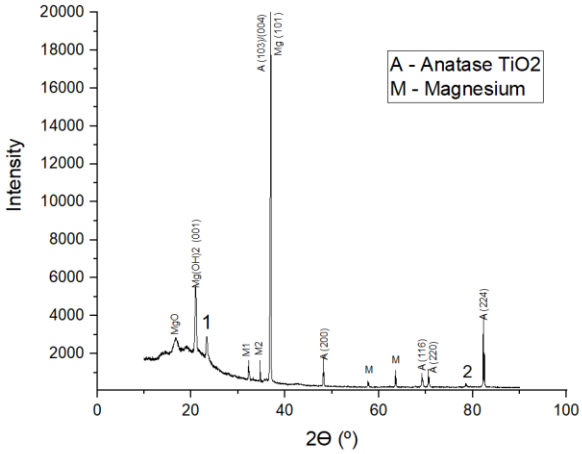

Figure 5-4 XRD of TiO2 ED on WAAM printed AZ61A alloy substrates.

For this next phase of the study, two other samples of the commercial WAAM printed AZ61A alloy underwent examination. The first sample was subjected to electrodeposition at 2 V for a duration of 45 minutes, without subsequent annealing. The second sample underwent electrodeposition at 1 V for 45 minutes, also without annealing. Ti hydroxides phases was expected to be detected. Magnesium and magnesium reaction products are also expected although some peaks may overlap. The following graphs shows the obtained results regarding the XRD of the 3 samples.

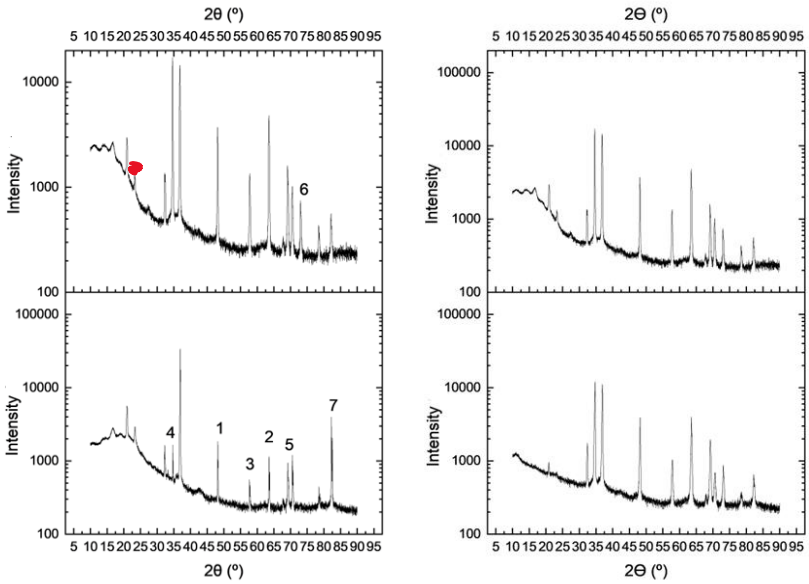

Figure 5-5 On the left side, XRD comparison between unannealed (top) and annealed (bottom) TiO_2 ED at 1 V for 45 minutes. On the right side XRD comparison between unannealed ED for 45 minutes at 1 V (top) and 2 V (bottom).

After comparing the diffraction patterns before and after annealing, it was possible to observe the influence on the change in surface structure of the coating. It was associated the decrease in

intensity and width in 1, 4, and area 5 in Figure 5-5 (and detailed in Figure A-6-14) with the formation of the crystalline anatase phase. Additionally, we noted an increase in the peak at 7. XRD patterns of TiO_2 reveal that even before calcination peaks of anatase were detected. Regarding magnesium byproducts, the peak at 6 disappeared, and peaks 2 and 3 showed a decrease. Since these are associated with magnesium diffraction patterns, we can conclude that they result from hydroxides that underwent alteration during the annealing process. Regarding the comparison of electrodeposition at 1 V or 2 V, some differences were observed. The diffraction pattern is similar at all peaks for 2 theta values above 25°. However, a decrease in noise in the baseline is observed with higher voltage. This could be a consequence of secondary reactions occurring around the titanium structure modification. It is also noticeable in the deposition without annealing that the peak at 25° (typical of anatase) becomes more visible (red dot).

The presence of aluminium (Al) in the alloy could influence the position of the peak at 36.93° as the addition of alloying elements can affect the lattice parameters and crystal structure of the material, leading to shifts in XRD peaks and the formation of solid solutions with magnesium. This can result in shifts or broadening of XRD peaks associated with both magnesium and any compounds formed during the electrodeposition process, such as TiO_2. Additional characterization techniques and comparison with reference patterns may be necessary to accurately identify the phases present due to the AZ61Aalloy [21], [65], [76]. CTAB typically does not exhibit distinct peaks in X-ray diffraction (XRD) patterns due to its organic nature and amorphous structure. Therefore, it's unlikely to find specific 2 θ values associated with CTAB in XRD analysis. However, if CTAB is present as a residue or impurity on the surface of a sample, it may contribute to a broad hump in the XRD pattern, usually observed at low angles. This hump is often indicative of amorphous or poorly crystalline materials. Therefore, in our analysis, CTAB is more likely to affect the overall background signal rather than produce sharp peaks, even if is noticeable a higher influence of the deposition voltage rather than the annealing process, in regard to reducing the hump observed at low 2 θ values[138], [139].

5.2.2 SEM Results

In this section, SEM images obtained after the TiO_2 ED (at 1 V for 45 minutes) process on the AZ61A alloy filament and WAAM printed substrates are presented in Figure 5-6 and Figure 5-7, respectively. As expected, SEM images revealed a successful ED of TiO_2. The surface of the coated filament appears to be uniform, covering the entire filament with a thick homogeneous layer and without any significant clusters, cracks, or crevices. It was noticed an alignment in the surface crystals and the presence of black spots that may result from corrosion products formed during the electrochemical activity of the ED process. It is also possible to observe some white spots that may result from titanium deposition, due to the reducing power of CTAB, which promotes the incorporation of this substance, promoting anatase phase. It is also important to refer that the difference in surface area exposed during

electrochemical test regarding AZ61A filament or WAAM substrates (0,05 cm^2 and 3,5 cm^2 respectfully), may influence coating properties due to alterations on the electric field created with the graphite rod counter.

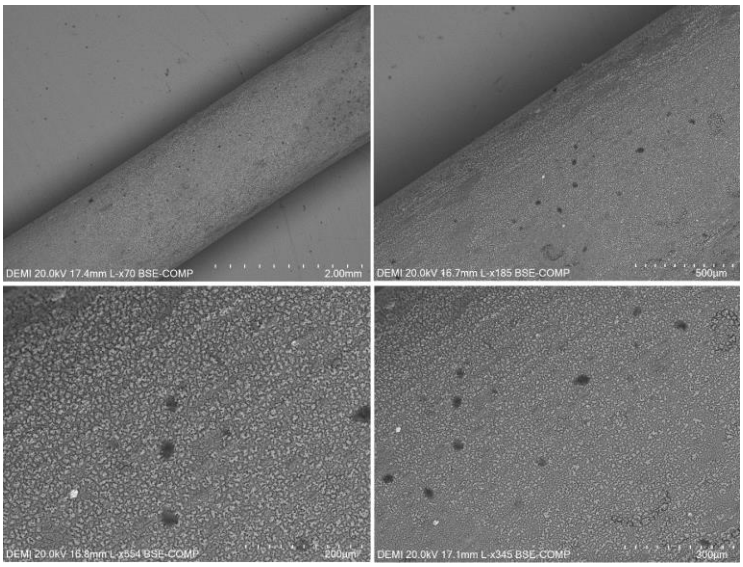

Figure 5-6 SEM of AZ61A alloy after electrodeposition of TiO_2 at 1V for 45 minutes.

On the WAAM printed substrate, surface effects were a bit different as surface roughness is observed, which correlates directly with the voltage response. Moreover, as the concentration of TiO_2 nanoparticles increased, the coating surface exhibited darkening (see Figure 5-6). This darkening phenomenon could be influenced primarily by comprising hydrogen, discharged, which induced oxygen vacancies in the TiO_2 lattice. As a result, Ti^{4+} ions were reduced to Ti^{3+}, leading to the darkening of the coating surface with higher incorporation of TiO_2 nanoparticles. Although the coating seemed thick after calcination, SEM images revealed that several dark spots occurred on the surface. The absorption of surface contaminants by the raw material (substrate and feedstock wire), such as grease, moisture and unwanted dust particles leads to generation of porosity on solidification.

The influence of Cl^- or other reactive ions on the surface grooves can affect the corrosion effect, manifested by the action of H_2, in the darker spots. This leads to increased area exposed, originating more corrosion. It is also important to note that the area of the filament compared to the graphite rod, when compared to the WAAM substrate, is much smaller. This can influence, in that, for the same electrical potential, a smaller area will increase its electrochemical activity. However, it is also observable the alignment in surface structure, a good indicator of anatase crystals formation. Both images may potentially indicate that the main objective of our study was achieved, but further research on WAAM substrates with TiO_2 coating is required to discard surface irregularities with substrate defect or improper adhesion [67], [69], [168], [169].

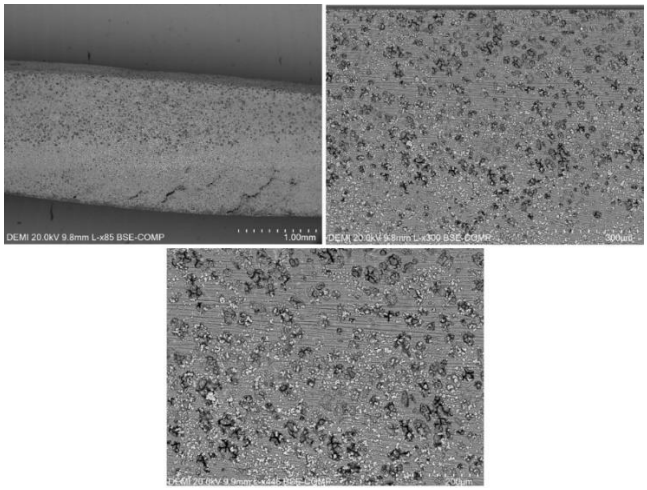

Figure 5-7 SEM image of WAAM printed AZ61A substrate + TiO_2 coating.

5.3 *In-vitro* Degradation Tests

The results of mass variation during in-vitro degradation tests are shown in Table A-6, in the appendix section, and in Figure 5-8. As shown, there are different pattern between the substances regarding the mass variation. In the titanium alloy the ratio is close to 1, which aligns with its natural corrosion resistance nature. The AZ61A alloy without coating or with unannealed coating showed less favourable results than the alloy with annealed coating

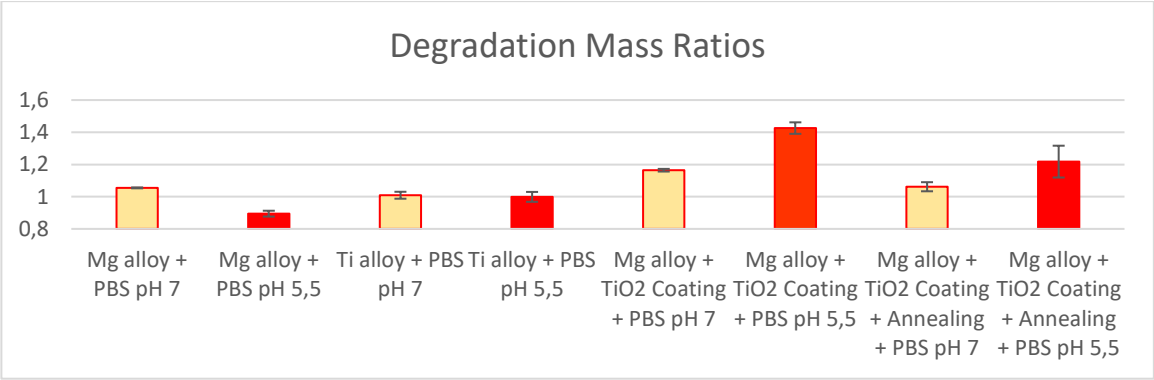

Figure 5-8 Mass ratios in degradation tests.

. As the degradation tests progressed, a dark surface began to cover the uncoated magnesium alloys. However, the filaments with coating, with and without annealing, maintained an unchanged surface. Over the weeks, an increase in filament weight and the beginning of precipitate formation attached to the uncoated AZ61A filament were observed. Since the PBS solution was changed weekly, the dissolution capacity would not maintain saturation values. However, this also led to believe that the crystals may be formed by degradation products reacting with products of ionic dissociation in the PBS. Figure A-6-15 shows the precipitates attached to the uncoated AZ61A after *in-vitro* degradation test with acid PBS, displaying improved degradation results with TiO_2 coating. Over the weeks the crystals continued

to increase in size, and eventually were collected from the uncoated and unannealed coated alloy in PBS 5.5 for further analysis. In the following weeks some deposits formed in the uncoated AZ61A in neutral PBS. The deposit corrosion layer increased its thickness and allowed the formation of large crystal, which were also collected for further analysis, with the help of a scalpel. Although it's important to note that the $H_2PO_4^-$ and HPO_4^{2-} ions present in PBS may react and form new products with the Mg alloy. This is evident in their low mass ratio of the uncoated AZ61A alloy after precipitates removal, as the precipitates also result from degradation products of the alloy. We should also address that under dynamic degradation tests precipitate formation may be diminished leading to different results in the mass ratios. It is important to note that the alloy with TiO_2 coating, with or without annealing, did not exhibit the same type of aggregates in the first weeks. However, deposits formed on the surface of the alloy with coating without annealing, which turn it almost entirely white by the end of the tests, in accord with the mass gain shown in Figure 5-8. Overall, the annealed TiO_2 coating offered protecting capabilities to the AZ61A alloy, showing resistance to degradation (Figure A-6-11).

After immersion, unannealed samples exhibited corrosion layers of variable homogeneity on their surfaces. In Figure A-6-12 it is observed that the annealed TiO_2 coating (3) showed significantly better results, when compared to uncoated Mg alloy (1), with decreased surface degradation and mass loss. When compared to the uncoated (2) or unannealed coating (4), it maintained the surface integrity throughout the degradation tests, having in some cases developed some precipitates at the uncoated part of the filament due to wire cutter cutting. Regarding the substances mass loss, as cleaning procedures only partially dissolved these corrosion layers, the dissolution of Mg alloys in PBS results in the precipitation of Mg-containing corrosion products on the substrates surface. This process involves the reaction between the magnesium alloy and the PBS solution, followed by the formation of insoluble magnesium phosphate precipitates, in the alloy or the PBS, such as $Mg_3(PO_4)_2$, due to pH increase resulting from the reaction of magnesium hydroxide at the Mg alloy surface[170]. However, a study of Schille et al. (2011) suggested that static immersion tests in simulated body fluids like PBS may not accurately simulate the corrosion behaviour of Mg alloys under in vivo conditions. While Mg alloys tested in PBS under static conditions showed weight gain due to the formation of insoluble corrosion layers, the same alloys exhibited weight loss when exposed to blood as a corrosion medium under dynamic conditions. In the blood test system, weight loss was observed for the Mg alloys investigated. Conversely, Mg alloys tested in PBS under static conditions showed weight gain due to corrosion layer formation. These layers could be partially removed by ultrasonic cleaning in water.[171] It was observed similar behaviour and the mass loss in uncoated Mg alloy in PBS 5,5 is potentially mostly due to precipitate removal.

After the removal of the precipitates from the filaments, XRD analysis was performed to identify the corrosion products that easily formed on the surface of the alloy. The most expected products would result from the degradation of magnesium and its reactions with oxides, hydroxides and phosphate groups mentioned early. Results potentially indicate presence of $Mg(OH)_2$ and corrosion products influenced by the TiO_2 coating [172], [173], [174], [175], [176], [177]. PBS solutions could also have an

influence on our results, with its high ionic dissociation, as research indicates that magnesium alloys display varying degradation patterns in different simulated body fluid solutions. The concentration of buffering agents and the presence of hydrocarbonates in test solutions are key factors influencing degradation behaviour, particularly in the early stages. Higher concentrations of buffering agents result in more negative corrosion potentials for the samples. The rapid reaction of hydroxide ions (OH^-) with abundant buffers in the solution accelerates the transformation from Mg to Mg^{2+}, contributing significantly to the elevated degradation rates observed [178].

Xu et al. investigated in vitro and in vivo three different Mn-containing magnesium alloys. For the in vitro study a PBS for the immersion test was used. With this simulated body fluid, a mass increase was measured and after cleaning a weight loss could be measured. However, the in vivo animal study showed only degradation with the same alloys. In this in vitro study precipitates also could be found, but they were not specified. In the presence of NaCl, in PBS, various layers such as crystalline $Mg(OH)_2$, amorphous phosphate-containing, and amorphous carbonated (Mg)-phosphate layers form. However, these layers offer poor protective properties. If the pH remains neutral, as it does in vivo due to homeostasis, corrosion will not be halted[179]. Corrosion behaviour in NaCl solutions initially exceeded that in PBS, but this trend reversed over prolonged immersion periods. The stabilization of MgO corrosion products by phosphorus-containing compounds contributed to this reversal, enhancing protection by mitigating the aggressive effects of chloride ions[180]. The instability of the in vivo corrosion layer, primarily composed of $Mg(OH)_2$, contributes to differences in corrosion rates between in vivo and in vitro environments. $Mg(OH)_2$ is unstable in aqueous solutions, particularly in chloride-containing environments. In vitro, corrosion ceases when an equilibrated ion concentration is reached, but in vivo, electrolyte concentrations remain in flux due to homeostasis, preventing equilibrium and resulting in complete material corrosion[181]. Since *in-vivo* degradation rates depend strongly on the location of an implant within the body and previous studies suggested that the degradation rate accelerates in surrounding tissues with higher degrees of vascularization, as the enhanced exchange of bodily fluid promotes the degradation of bioresorbable materials, a possible step will be evaluation under different PBS.

5.4 Electrochemical and Corrosion Experiments

Following the *in*-vitro degradation tests of TiO_2 coating on the AZ61A substrates, our investigation advanced into understanding its electrochemical behaviour in simulated human body fluid environment, starting by running Open Circuit Potential (OCP) tests in neutral and acid PBS.

For the uncoated AZ61A alloy, the OPC measurements in neutral PBS (Figure A-6-17) revealed a corrosion potential (Ecorr) of -1,45 V. Similarly, in an acidic PBS, the Ecorr was -1,72 V. The corrosion potential is a critical parameter in electrochemical analysis as it refers to the potential at which the anodic (loss of electrons) and cathodic (gain of electrons) reaction rates are in equilibrium, indicating a point where no electrochemical reaction is occurring. During the OPC tests, this equilibrium was visually

observed with the absence of hydrogen (H_2) bubbles when the current reached zero. In contrast, for the AZ61A alloy coated with TiO_2 coating, the OPC measurements in neutral PBS revealed a corrosion potential of -1.66 V. Notably, in acidic PBS, the potential exhibited a distinct behaviour by continually rising throughout the test, ultimately approaching -1.68 V (Figure A-6-18). This observed increase in potential during the test in the acidic environment is indicative of dynamic electrochemical reactions occurring at the material's surface, as the acidic medium brings the OCP of the coated alloy to values closer to the neutral medium, an increase unlike what is observed in the coated alloy. After OCP test we measured the PBS solution having indeed increased. We also noted a decrease in the OCP value of the coated alloy in neutral medium when compared with the test in neutral medium without the TiO_2 coating. Regarding the OCP tests of the coated alloy in acidic pH, we start by observing a stabilization slope at around -1,75 V, at which point the potential showed irregular behaviour and begin its increasing state until the tests were concluded. One possible explanation could be the integrity of the TiO_2 coating when in acid medium, which may lead to expose areas of the alloy, bringing the corrosion potential to similar values of what is observed in the neutral PBS. Also, the coating and alloy degradation byproducts may occur and influence the solution pH (later confirmed), altering results unpredictably, as the degradation rate may vary with the alloy areas exposed. In that regard we aimed to use substrates with the apparently most uniform and cluster free coatings. Overall, it was observed a general decrease in Ecorr in the TiO_2 coated filaments, which may indicate better corrosion resistance[179]. Then CV tests were started with a CV trial of 50 cycles in neutral PBS and parameters described in section 4.6, evaluating the electrochemical behaviour while optimizing the testing duration. Figure 5-9 refers to the first extended trial CV, performed in neutral PBS, and the following CV test comprised of 20 cycles each.

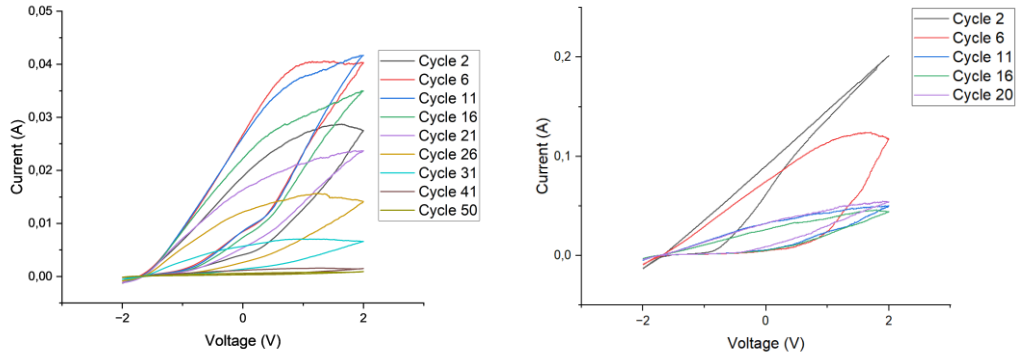

Figure 5-9 Trial CV test of 50 cycles in neutral PBS (left) and CV of 20 with parameters described in section 4.6 (right).

During the 50 cycles it is possible to notice that the protective layer that forms, resulting from the reaction products that form during the test could explain the decrease in current until it reaches zero as Magnesium works best as a conductor without the byproducts layer. Except for cycle 2, the curves present a gradual decrease in current resulting from the formation of products, which acts a protective layer preventing electrochemical activity on the substrate. This could mean that the system was still stabilizing at cycle 2. At the end of the first CV test a layer of foam formed on top of the solution cup,

greyish in colour. regarding the observed behaviour it could mostly be due to byproduct originated in the degradation of the filament during the CV (Figure A-6-35). During cyclic voltammetry tests conducted using a magnesium alloy coated with titanium dioxide electrochemical reactions may occur at the electrode surface, in addition to the above mentioned in section 2.1.1. The cycle 20 test in a neutral medium exhibited higher current value unlike expected. This could be attributed to the protective layer that gradually forms during degradation and is not corroded by the surrounding medium, as opposed to the PBS 5.5, where the protective layer undergoes degradation. However, as the number of cycles increases, the protective layer formed by the corrosion reaction products is gradually eroded in the acidic PBS but not in the neutral environment. This observation may suggest the higher current values observed in the neutral medium CV of commercial AZ61A Alloy with TiO_2 coating in acid medium.

5.4.1 CV of commercial AZ61A Alloy and TiO_2 coating

The first CV tests began by observing the difference in behaviour of the uncoated and TiO_2 coated alloy in neutral and acid PBS. Figure 5-10 and Figure 5-11 shows our results. In both neutral and acidic mediums, the TiO_2 coating significantly reduces the current compared to the exposed alloy, potentially indicating less corrosion. The neutral medium exhibits higher current values than the acidic medium due to increased corrosion of the magnesium alloy. However, the neutral medium shows narrower curves, suggesting higher reversibility of redox processes and potentially increased mass loss. Regarding the two media, we observed narrow polarization curve and lower cathodic peaks with the TiO_2 coating. Conversely, the acidic medium produces broader curves, indicating slower electron transfer kinetics and reduced mass loss.

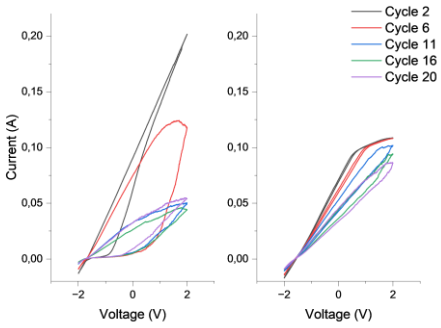

Figure 5-10 CVs in neutral PBS of uncoated (left) AZ61A commercial alloy and with TiO_2 coating (right).

The TiO_2 coating standardizes the curves and reduces corrosion in the neutral medium by maintaining the protective layer formed by the coating and corrosion by-products. Despite higher current values resulting from the corrosion of the protective layer, a steady decrease in current is observed throughout the test. The broader curve in cycle 6 of the neutral PBS suggests a balance between alloy protection from byproducts and the effects of pH and solution saturation on electrochemical kinetics. In the acid environment, the uncoated alloy exhibited a higher cathodic peak in cycle 2 compared to the TiO_2-coated alloy, with a gradual decrease in current thereafter due to corrosion induced by the acidic medium. The

absence of corrosion product aggregation prevented rapid increases in exposed alloy area and current. The neutral CV showed slower electron transfer kinetics, suggesting that corrosion products restricted the exposed alloy area, decreasing mass transfer and corrosion.

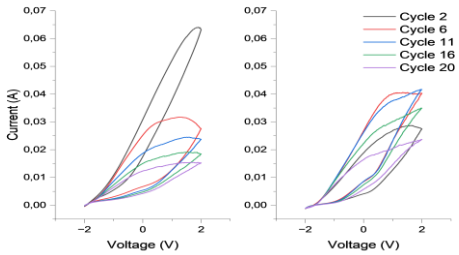

Figure 5-11 Comparison between CVs in acid PBS of uncoated (left) AZ61A commercial alloy and with TiO_2 coating (right).

The TiO_2 coating appeared to protect the alloy from environmental reactions, with lower cathodic peaks observed in cycle 2. However, as the acid PBS corroded the TiO_2 layer, the exposed area and current increased from cycle 6 onward. Although slightly higher current values were achieved in neutral medium, the coated alloy consistently exhibited broader curves, indicating a positive contribution of the TiO2 coating in reducing electrochemical activity around the implants.

5.4.2 CV of WAAM AZ61A substrates with TiO_2 coating in PBS

Upon CV tests conducted at WAAM printed substrates, the results were gathered in Figure 5-12, for neutral PBS and in Figure 5-13 for the acid PBS. As the WAAM substrates are larger than the filament, they may have better withstood the 20 cycles. We noticed a decrease in current in the alloy, as the test advanced. The uncoated substrates presented similar current values to those with coating leading us to begin comparing the effect of the coating in similar environments. Initially, magnesium alloys are less resistant to corrosion in an acidic environment due to the solubility of the corrosion layer.

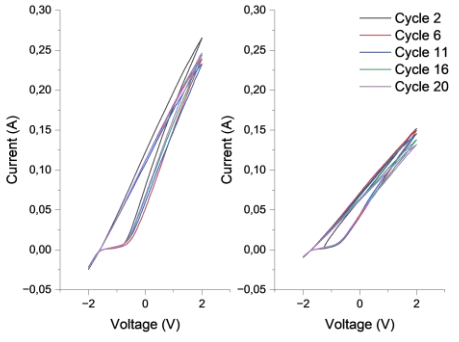

Figure 5-12 CVs in Neutral PBS of uncoated (left) AZ61A WAAM printed substrates, and with TiO_2 coating (right).

However, as the test progresses, the reactions in the acid environment become less intense due to the formation of a thick corrosion product layer, as shown in Figure 5-13.

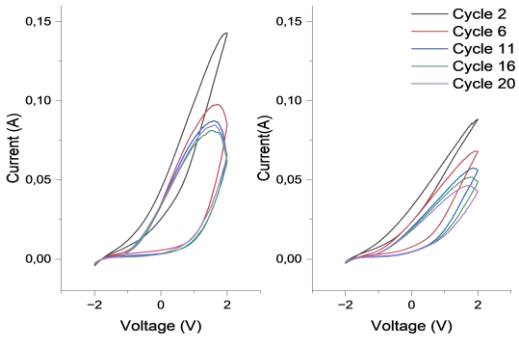

Figure 5-13 CVs in acid PBS of uncoated (left) AZ61A WAAM printed substrates, and with TiO_2 coating (right).

Contrary to expectations, this layer does not detach easily, ultimately protecting the material. Possible justifications include solution saturation, increased material roughness, pH changes, and differences in the adhesion of corrosion products. In dynamic environments like the human body, constant solution renewal and light cleansing may affect corrosion behaviour differently. Mass variation studies of magnesium alloys are challenging due to the formation of corrosion product layers, with some results indicating mass gain rather than loss [182]. Results were similar between commercial alloys and WAAM-printed ones, even though differences may occur due to different surface area of the electrodes when comparing AZ61A filament or WAAM printed substrates.

5.4.3 Mass Variation and Corrosion

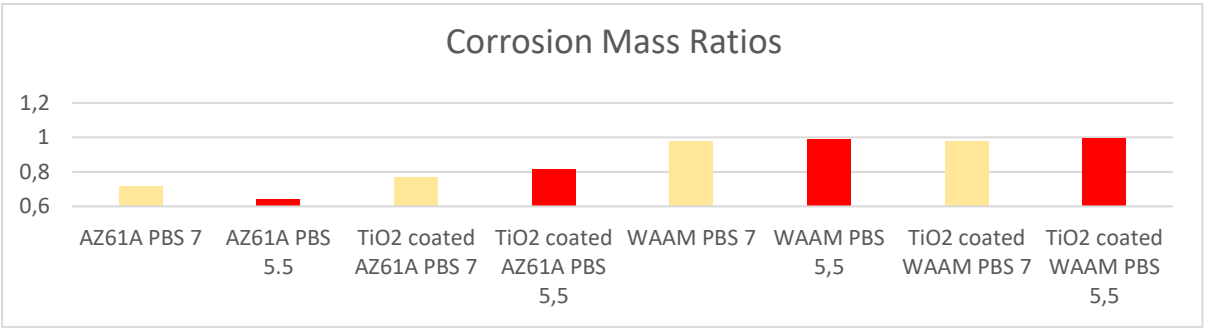

Figure 5-14 Corrosion Mass Ratios in CV Experiments

Figure 5-14 shows the mass ratios calculated to determine the corrosion resistance of the Mg alloy and the influence of the TiO_2 in that same resistance. To quantify the impact of the electrochemical tests on our coated substrates, we performed weight change analysis. The substrates were weighed both before and after the cyclic voltammetry tests. Any weight change observed indicate the extent of material loss due to corrosion or other electrochemical reactions occurring during the tests [169].

Results show a clear difference between WAAM substrates and Mg filament. This could be due to the difference in surface area of the WE compared with the CE. The TiO_2 could in fact considerably improve mass loss through corrosion in the alloy and show similar results with uncoated WAAM printed substrates. Further investigation is required to ensure feasibility of data. Upon observation of the CV test,

which shows a decrease of current in acid mediums, a correlation with mass loss may be observed in Figure 5-14.

The combination of OPC, CV, surface analysis, and weight change analysis provided a comprehensive understanding of how the TiO_2 coatings influenced the electrochemical behaviour and corrosion resistance of the AZ61A commercial Mg-based biomedical alloy. Regarding the corrosion in uncoated WAAM substrates, Figure A-6-32 and Figure A-6-31 show higher corrosion on the acid substrate. The protective layer is absent, and the structure surface appears to show severe cracks, from which further corrosion may occur. Figure A-6-41 and Figure A-6-43 show more cracks on the acid PBS, over the corrosion products, where the Cl^- penetrates the surface. Overall neutral PBS shows more corrosion products, and the corrosion products was formed with the hydroxide layer(Figure A-6-42 and Figure A-6-40).

6

CONCLUSIONS AND FUTURE PERSPECTIVES

In the field of biomedical engineering, bioresorbable material stands at the forefront of innovation in biomaterials. Set to be absorbed by human body, these materials corrode as their function in human body is performed, without losing properties during the process. Mg based alloys shows great advantages in this field, but its limitations fall in the fast degradation rate of magnesium, Recently, a plethora of studies have suggested that the surface modification of these materials could lead to improved corrosion resistance. This work aimed to investigate the effects of TiO_2 coating and electrochemical deposition of Mg alloys on biodegradable implants through degradation tests, chemical and structural characterization and electrochemical activity.

The ED process was conducted ate 0.5, 1, 1.5, and 2 V for the deposition periods of 15, 30 45 and 60 minutes. It was determined that, regarding our study, deposition at 1V for 45 minutes showed the apparently best surface, later confirmed with Optical Microscope images. ED parameters of the following depositions remained unchanged. SEM images confirmed that ED could indeed cover the substrate with a homogeneous film, later confirmed anatase phase TiO2 through Raman Spectroscopy and XRD. Coating thickness and integrity were obtained with the use of CTAB in the deposition period, followed by an annealing process at 450 ºC, to improve structure properties.

In-vitro degradation test revealed that the TiO_2 coated alloy presented overall better degradation rates that uncoated Mg alloy, particularly in acid media. The TiO_2 coating was in fact capable of preventing precipitate formation. Additionally, when compared to the Ti based alloy or the AZ61A alloy, the TiO_2 coating maintained structural integrity on the AZ61A leading to reduced loss of mass. Electrochemical experiments demonstrated that OCP in coated substrates revealed generally lower Ecorr values, in neutral and acid PBS. Regarding CV tests, materials revealed a decrease in cathodic peaks which can promote a favorable electrochemical response, observed through the SEM images after CV process, where a protective layer formed in neutral PBS but was dissolved in acid PBS, thus influencing corrosion protective behavior. The following steps may involve using different SBF in biocompatibility behavior *in-vitro*, toxicity, and cell adhesion tests to explore the biological properties of the substrates with TiO_2 coating and different geometries and surface area in substrates. Potential enhancements could include conducting tests under dynamic environments and utilizing real body fluids.

BIBLIOGRAPHY

[1] P. C. Banerjee, S. Al-Saadi, L. Choudhary, S. E. Harandi, and R. Singh, "Magnesium implants: Prospects and challenges," *Materials*, vol. 12, no. 1. MDPI AG, Jan. 03, 2019. doi: 10.3390/ma12010136.

[2] T. A. van Vugt, J. A. P. Geurts, J. J. Arts, and N. C. Lindfors, "Biomaterials in treatment of orthopedic infections," *Management of Periprosthetic Joint Infections (PJIs)*, pp. 41–68, Jan. 2017, doi: 10.1016/B978-0-08-100205-6.00003-3.

[3] F. Witte, "The history of biodegradable magnesium implants: A review," *Acta Biomaterialia*, vol. 6, no. 5. Elsevier Ltd, pp. 1680–1692, 2010. doi: 10.1016/j.actbio.2010.02.028.

[4] S. Chatterjee, M. Saxena, D. Padmanabhan, M. Jayachandra, and H. J. Pandya, "Futuristic medical implants using bioresorbable materials and devices," *Biosensors and Bioelectronics*, vol. 142. Elsevier Ltd, Oct. 01, 2019. doi: 10.1016/j.bios.2019.111489.

[5] Y. Chen, Z. Xu, C. Smith, and J. Sankar, "Recent advances on the development of magnesium alloys for biodegradable implants," *Acta Biomaterialia*, vol. 10, no. 11. Elsevier Ltd, pp. 4561–4573, Nov. 01, 2014. doi: 10.1016/j.actbio.2014.07.005.

[6] G. Manivasagam and S. Suwas, "Biodegradable Mg and Mg based alloys for biomedical implants," *Materials Science and Technology (United Kingdom)*, vol. 30, no. 5. Maney Publishing, pp. 515–520, 2014. doi: 10.1179/1743284713Y.0000000500.

[7] H. Ibrahim, S. N. Esfahani, B. Poorganji, D. Dean, and M. Elahinia, "Resorbable bone fixation alloys, forming, and post-fabrication treatments," *Materials Science and Engineering C*, vol. 70. Elsevier Ltd, pp. 870–888, Jan. 01, 2017. doi: 10.1016/j.msec.2016.09.069.

[8] S. Vach Agocsova *et al.*, "Resorbable Biomaterials Used for 3D Scaffolds in Tissue Engineering: A Review," *Materials*, vol. 16, no. 12. MDPI, Jun. 01, 2023. doi: 10.3390/ma16124267.

[9] R. Kumar and P. Katyal, "Effects of alloying elements on performance of biodegradable magnesium alloy," *Mater Today Proc*, vol. 56, pp. 2443–2450, Jan. 2022, doi: 10.1016/J.MATPR.2021.08.233.

[10] A. M. Al Alawi, S. W. Majoni, and H. Falhammar, “Magnesium and Human Health: Perspectives and Research Directions,” *International Journal of Endocrinology*, vol. 2018. Hindawi Limited, 2018. doi: 10.1155/2018/9041694.

[11] Z. Zeng, M. Salehi, A. Kopp, S. Xu, M. Esmaily, and N. Birbilis, “Recent progress and perspectives in additive manufacturing of magnesium alloys,” *Journal of Magnesium and Alloys*, vol. 10, no. 6. National Engg. Reaserch Center for Magnesium Alloys, pp. 1511–1541, Jun. 01, 2022. doi: 10.1016/j.jma.2022.03.001.

[12] R. Costello, A. Rosanoff, F. Nielsen, and C. West, “Perspective: Call for Re-evaluation of the Tolerable Upper Intake Level for Magnesium Supplementation in Adults,” *Advances in Nutrition*, vol. 14, no. 5, pp. 973–982, Sep. 2023, doi: 10.1016/j.advnut.2023.06.008.

[13] G. K. Schwalfenberg and S. J. Genuis, “The Importance of Magnesium in Clinical Healthcare,” *Scientifica (Cairo)*, vol. 2017, 2017, doi: 10.1155/2017/4179326.

[14] A. M. Al Alawi, S. W. Majoni, and H. Falhammar, “Magnesium and Human Health: Perspectives and Research Directions,” *International Journal of Endocrinology*, vol. 2018. Hindawi Limited, 2018. doi: 10.1155/2018/9041694.

[15] M. M. Jamel, M. M. Jamel, and H. F. Lopez, “Designing Advanced Biomedical Biodegradable Mg Alloys: A Review,” *Metals*, vol. 12, no. 1. MDPI, Jan. 01, 2022. doi: 10.3390/met12010085.

[16] I. Antoniac *et al.*, “Magnesium-Based Alloys Used in Orthopedic Surgery,” *Materials*, vol. 15, no. 3. MDPI, Feb. 01, 2022. doi: 10.3390/ma15031148.

[17] J. L. Wang, J. K. Xu, C. Hopkins, D. H. K. Chow, and L. Qin, “Biodegradable Magnesium-Based Implants in Orthopedics—A General Review and Perspectives,” *Advanced Science*, vol. 7, no. 8. John Wiley and Sons Inc., Apr. 01, 2020. doi: 10.1002/advs.201902443.

[18] M. P. Staiger, A. M. Pietak, J. Huadmai, and G. Dias, “Magnesium and its alloys as orthopedic biomaterials: A review,” *Biomaterials*, vol. 27, no. 9. pp. 1728–1734, Mar. 2006. doi: 10.1016/j.biomaterials.2005.10.003.

[19] C. K. Seal, K. Vince, and M. A. Hodgson, “Biodegradable surgical implants based on magnesium alloys - A review of current research,” in *IOP Conference Series: Materials Science and Engineering*, 2009. doi: 10.1088/1757-899X/4/1/012011.

[20] F. Witte *et al.*, “Degradable biomaterials based on magnesium corrosion,” *Curr Opin Solid State Mater Sci*, vol. 12, no. 5–6, pp. 63–72, Oct. 2008, doi: 10.1016/j.cossms.2009.04.001.

[21] G. Song, “Control of biodegradation of biocompatable magnesium alloys,” *Corrosion Science*, vol. 49, no. 4. pp. 1696–1701, Apr. 2007. doi: 10.1016/j.corsci.2007.01.001.

[22] G. Eddy Jai Poinern, S. Brundavanam, and D. Fawcett, “Biomedical Magnesium Alloys: A Review of Material Properties, Surface Modifications and Potential as a Biodegradable

Orthopaedic Implant," *Am J Biomed Eng*, vol. 2, no. 6, pp. 218–240, Jan. 2013, doi: 10.5923/j.ajbe.20120206.02.

[23] C. Liu, Z. Ren, Y. Xu, S. Pang, X. Zhao, and Y. Zhao, "Biodegradable Magnesium Alloys Developed as Bone Repair Materials: A Review," *Scanning*, vol. 2018. Hindawi Limited, 2018. doi: 10.1155/2018/9216314.

[24] Y. Chen, Z. Xu, C. Smith, and J. Sankar, "Recent advances on the development of magnesium alloys for biodegradable implants," *Acta Biomaterialia*, vol. 10, no. 11. Elsevier Ltd, pp. 4561–4573, Nov. 01, 2014. doi: 10.1016/j.actbio.2014.07.005.

[25] S. Chatterjee, M. Saxena, D. Padmanabhan, M. Jayachandra, and H. J. Pandya, "Futuristic medical implants using bioresorbable materials and devices," *Biosensors and Bioelectronics*, vol. 142. Elsevier Ltd, Oct. 01, 2019. doi: 10.1016/j.bios.2019.111489.

[26] M. M. Jamel, M. M. Jamel, and H. F. Lopez, "Designing Advanced Biomedical Biodegradable Mg Alloys: A Review," *Metals*, vol. 12, no. 1. MDPI, Jan. 01, 2022. doi: 10.3390/met12010085.

[27] G. Manivasagam and S. Suwas, "Biodegradable Mg and Mg based alloys for biomedical implants," *Materials Science and Technology (United Kingdom)*, vol. 30, no. 5. Maney Publishing, pp. 515–520, 2014. doi: 10.1179/1743284713Y.0000000500.

[28] V. S. Telang, R. Pemmada, V. Thomas, S. Ramakrishna, P. Tandon, and H. S. Nanda, "Harnessing additive manufacturing for magnesium-based metallic bioimplants: Recent advances and future perspectives," *Current Opinion in Biomedical Engineering*, vol. 17. Elsevier B.V., Mar. 01, 2021. doi: 10.1016/j.cobme.2021.100264.

[29] V. Herber, B. Okutan, G. Antonoglou, N. G. Sommer, and M. Payer, "Bioresorbable magnesium-based alloys as novel biomaterials in oral bone regeneration: General review and clinical perspectives," *Journal of Clinical Medicine*, vol. 10, no. 9. MDPI, May 01, 2021. doi: 10.3390/jcm10091842.

[30] H. Zhou, B. Liang, H. Jiang, Z. Deng, and K. Yu, "Magnesium-based biomaterials as emerging agents for bone repair and regeneration: from mechanism to application," *Journal of Magnesium and Alloys*, vol. 9, no. 3. National Engg. Reaserch Center for Magnesium Alloys, pp. 779–804, May 15, 2021. doi: 10.1016/j.jma.2021.03.004.

[31] D. Castro, P. Jaeger, A. C. Baptista, and J. P. Oliveira, "An overview of high-entropy alloys as biomaterials," *Metals*, vol. 11, no. 4. MDPI AG, 2021. doi: 10.3390/met11040648.

[32] C. Peng, N. Cao, Z. Qi, Y. Yan, R. Wu, and G. Wang, "Preparation and corrosion performance of PPy/silane film on AZ31 magnesium alloy via one-step cyclic voltammetry," *Polymers (Basel)*, vol. 13, no. 18, Sep. 2021, doi: 10.3390/polym13183148.

[33] Y. Liu *et al.*, "Fundamental Theory of Biodegradable Metals—Definition, Criteria, and Design," *Advanced Functional Materials*, vol. 29, no. 18. Wiley-VCH Verlag, May 02, 2019. doi: 10.1002/adfm.201805402.

[34] U. Riaz, I. Shabib, and W. Haider, "The current trends of Mg alloys in biomedical applications—A review," *Journal of Biomedical Materials Research - Part B Applied Biomaterials*, vol. 107, no. 6. John Wiley and Sons Inc., pp. 1970–1996, Aug. 01, 2019. doi: 10.1002/jbm.b.34290.

[35] A. Kania, M. M. Szindler, and M. Szindler, "Structure and corrosion behavior of TiO2 thin films deposited by ALD on a biomedical magnesium alloy," *Coatings*, vol. 11, no. 1, pp. 1–14, Jan. 2021, doi: 10.3390/coatings11010070.

[36] K. Wieszczycka, K. Staszak, M. J. Woźniak-Budych, J. Litowczenko, B. M. Maciejewska, and S. Jurga, "Surface functionalization – The way for advanced applications of smart materials," *Coordination Chemistry Reviews*, vol. 436. Elsevier B.V., Jun. 01, 2021. doi: 10.1016/j.ccr.2021.213846.

[37] Z. Zeng, M. Salehi, A. Kopp, S. Xu, M. Esmaily, and N. Birbilis, "Recent progress and perspectives in additive manufacturing of magnesium alloys," *Journal of Magnesium and Alloys*, vol. 10, no. 6. National Engg. Reaserch Center for Magnesium Alloys, pp. 1511–1541, Jun. 01, 2022. doi: 10.1016/j.jma.2022.03.001.

[38] T.-S. Shih, W.-S. Liu, and Y.-J. Chen, "Fatigue of as-extruded AZ61A magnesium alloy," 2002. [Online]. Available: www.elsevier.com/locate/msea

[39] J. Ribeiro, "DEVELOPMENT OF RESORBABLE METAL-BASED BIOMEDICAL IMPLANTS," M.S. Thesis, Nova School of Science & Technology, Nova Univ., Lisbon, 2022., Lisbon, 2022.

[40] J. Zhang, Q. Yu, Y. Jiang, and Q. Li, "An experimental study of cyclic deformation of extruded AZ61A magnesium alloy," *Int J Plast*, vol. 27, no. 5, pp. 768–787, May 2011, doi: 10.1016/j.ijplas.2010.09.004.

[41] W. Gao *et al.*, "The status, challenges, and future of additive manufacturing in engineering," *CAD Computer Aided Design*, vol. 69, pp. 65–89, Dec. 2015, doi: 10.1016/j.cad.2015.04.001.

[42] N. Balashanmugam, "Perspectives on additive manufacturing in Industry 4.0," *Addit Manuf*, pp. 127–150, 2021, doi: 10.1016/B978-0-12-822056-6.00001-1.

[43] T. DebRoy *et al.*, "Additive manufacturing of metallic components – Process, structure and properties," *Progress in Materials Science*, vol. 92. Elsevier Ltd, pp. 112–224, Mar. 01, 2018. doi: 10.1016/j.pmatsci.2017.10.001.

[44] A. Zocca, G. Franchin, P. Colombo, and J. Günster, "Additive Manufacturing," in *Encyclopedia of Materials: Technical Ceramics and Glasses*, vol. 1–3, Elsevier, 2021, pp. 203–221. doi: 10.1016/B978-0-12-803581-8.12081-8.

[45] K. Chua, I. Khan, R. Malhotra, and D. Zhu, "Additive manufacturing and 3D printing of metallic biomaterials," *Engineered Regeneration*, vol. 2. KeAi Communications Co., pp. 288–299, Jan. 01, 2021. doi: 10.1016/j.engreg.2021.11.002.

[46] Y. Qin *et al.*, "Additive manufacturing of biodegradable metals: Current research status and future perspectives," *Acta Biomaterialia*, vol. 98. Acta Materialia Inc, pp. 3–22, Oct. 15, 2019. doi: 10.1016/j.actbio.2019.04.046.

[47] M. Vignesh *et al.*, "Development of Biomedical Implants through Additive Manufacturing: A Review," *Journal of Materials Engineering and Performance*, vol. 30, no. 7. Springer, pp. 4735–4744, Jul. 01, 2021. doi: 10.1007/s11665-021-05578-7.

[48] Z. Qi, B. Cong, B. Qi, H. Sun, G. Zhao, and J. Ding, "Microstructure and mechanical properties of double-wire + arc additively manufactured Al-Cu-Mg alloys," *J Mater Process Technol*, vol. 255, pp. 347–353, May 2018, doi: 10.1016/J.JMATPROTEC.2017.12.019.

[49] A. P. Moreno Madrid, S. M. Vrech, M. A. Sanchez, and A. P. Rodriguez, "Advances in additive manufacturing for bone tissue engineering scaffolds," *Materials Science and Engineering C*, vol. 100. Elsevier Ltd, pp. 631–644, Jul. 01, 2019. doi: 10.1016/j.msec.2019.03.037.

[50] R. Karunakaran, S. Ortgies, A. Tamayol, F. Bobaru, and M. P. Sealy, "Additive manufacturing of magnesium alloys," *Bioactive Materials*, vol. 5, no. 1. KeAi Communications Co., pp. 44–54, Mar. 01, 2020. doi: 10.1016/j.bioactmat.2019.12.004.

[51] T. Klein, A. Arnoldt, M. Schnall, and S. Gneiger, "Microstructure Formation and Mechanical Properties of a Wire-Arc Additive Manufactured Magnesium Alloy," *JOM*, vol. 73, no. 4, pp. 1126–1134, Apr. 2021, doi: 10.1007/s11837-021-04567-4.

[52] M. Chaturvedi, E. Scutelnicu, C. C. Rusu, L. R. Mistodie, D. Mihailescu, and S. Arungalai Vendan, "Wire arc additive manufacturing: Review on recent findings and challenges in industrial applications and materials characterization," *Metals*, vol. 11, no. 6. MDPI AG, Jun. 01, 2021. doi: 10.3390/met11060939.

[53] S. R. Singh and P. Khanna, "Wire arc additive manufacturing (WAAM): A new process to shape engineering materials," in *Materials Today: Proceedings*, Elsevier Ltd, 2021, pp. 118–128. doi: 10.1016/j.matpr.2020.08.030.

[54] T. A. Rodrigues, V. Duarte, R. M. Miranda, T. G. Santos, and J. P. Oliveira, "Current status and perspectives on wire and arc additive manufacturing (WAAM)," *Materials*, vol. 12, no. 7, 2019, doi: 10.3390/ma12071121.

[55] B. Wu *et al.*, "A review of the wire arc additive manufacturing of metals: properties, defects and quality improvement," *Journal of Manufacturing Processes*, vol. 35. Elsevier Ltd, pp. 127–139, Oct. 01, 2018. doi: 10.1016/j.jmapro.2018.08.001.

[56] C. R. Cunningham, J. M. Flynn, A. Shokrani, V. Dhokia, and S. T. Newman, "Invited review article: Strategies and processes for high quality wire arc additive manufacturing," *Additive Manufacturing*, vol. 22. Elsevier B.V., pp. 672–686, Aug. 01, 2018. doi: 10.1016/j.addma.2018.06.020.

[57] D. Jafari, T. H. J. Vaneker, and I. Gibson, “Wire and arc additive manufacturing: Opportunities and challenges to control the quality and accuracy of manufactured parts,” *Mater Des*, vol. 202, Apr. 2021, doi: 10.1016/j.matdes.2021.109471.

[58] H. Yi, Q. Wang, and H. Cao, “Wire-arc directed energy deposition of magnesium alloys: microstructure, properties and quality optimization strategies,” *Journal of Materials Research and Technology*, vol. 20. Elsevier Editora Ltda, pp. 627–649, Sep. 01, 2022. doi: 10.1016/j.jmrt.2022.07.083.

[59] R. Soni, S. Jhavar, S. Tyeb, S. K. Gupta, S. Suwas, and K. Chatterjee, “Wire Arc Additive Manufacturing of Zinc as a Degradable Metallic Biomaterial,” *J Funct Biomater*, vol. 13, no. 4, Dec. 2022, doi: 10.3390/jfb13040212.

[60] A. R. McAndrew *et al.*, “Interpass rolling of Ti-6Al-4V wire + arc additively manufactured features for microstructural refinement,” *Addit Manuf*, vol. 21, pp. 340–349, May 2018, doi: 10.1016/j.addma.2018.03.006.

[61] R. Allavikutty, P. Gupta, T. S. Santra, and J. Rengaswamy, “Additive manufacturing of Mg alloys for biomedical applications: Current status and challenges,” *Current Opinion in Biomedical Engineering*, vol. 18. Elsevier B.V., Jun. 01, 2021. doi: 10.1016/j.cobme.2021.100276.

[62] L. E. Pompa, “Corrosion assessment and enhanced biocompatibility analysis of Corrosion assessment and enhanced biocompatibility analysis of biodegradable magnesium-based alloys biodegradable magnesium-based alloys.” [Online]. Available: https://scholarworks.utrgv.edu/leg_etd

[63] R. K. Singh Raman, S. Jafari, and S. E. Harandi, “Corrosion fatigue fracture of magnesium alloys in bioimplant applications: A review,” *Engineering Fracture Mechanics*, vol. 137. Elsevier Ltd, pp. 97–108, Mar. 01, 2015. doi: 10.1016/j.engfracmech.2014.08.009.

[64] E. Ghali, W. Dietzel, and K. U. Kainer, “Testing of general and localized corrosion of magnesium alloys: A critical review,” *Journal of Materials Engineering and Performance*, vol. 13, no. 5. pp. 517–529, Oct. 2004. doi: 10.1361/10599490420665.

[65] H. Hornberger, S. Virtanen, and A. R. Boccaccini, “Biomedical coatings on magnesium alloys - A review,” *Acta Biomaterialia*, vol. 8, no. 7. Elsevier Ltd, pp. 2442–2455, 2012. doi: 10.1016/j.actbio.2012.04.012.

[66] Y. Ouyang *et al.*, “Electrodeposition of F-doped hydroxyapatite-TiO2 coating on AZ31 magnesium alloy for enhancing corrosion protection and biocompatibility,” *J Mater Sci*, vol. 57, no. 36, pp. 17188–17202, Sep. 2022, doi: 10.1007/s10853-022-07732-5.

[67] W. H. Chen *et al.*, “Effect of TiO2 nanoparticles on the corrosion resistance, wear, and antibacterial properties of microarc oxidation coatings applied on AZ31 magnesium alloy,” *Surf Coat Technol*, vol. 476, Jan. 2024, doi: 10.1016/j.surfcoat.2023.130238.

[68] P. Tian and X. Liu, “Surface modification of biodegradable magnesium and its alloys for biomedical applications,” *Regenerative Biomaterials*, vol. 2, no. 2. Oxford University Press, pp. 135–151, Jun. 01, 2015. doi: 10.1093/rb/rbu013.

[69] X. Chen and S. S. Mao, “Titanium dioxide nanomaterials: Synthesis, properties, modifications and applications,” *Chemical Reviews*, vol. 107, no. 7. pp. 2891–2959, Jul. 2007. doi: 10.1021/cr0500535.

[70] S. Awasthi, S. K. Pandey, E. Arunan, and C. Srivastava, “A review on hydroxyapatite coatings for the biomedical applications: Experimental and theoretical perspectives,” *Journal of Materials Chemistry B*, vol. 9, no. 2. Royal Society of Chemistry, pp. 228–249, Jan. 14, 2021. doi: 10.1039/d0tb02407d.

[71] K. K. A. Mosas, A. R. Chandrasekar, A. Dasan, A. Pakseresht, and D. Galusek, “Recent Advancements in Materials and Coatings for Biomedical Implants,” *Gels*, vol. 8, no. 5. MDPI, May 01, 2022. doi: 10.3390/gels8050323.

[72] P. Wan, L. Tan, and K. Yang, “Surface Modification on Biodegradable Magnesium Alloys as Orthopedic Implant Materials to Improve the Bio-adaptability: A Review,” *J Mater Sci Technol*, vol. 32, no. 9, pp. 827–834, Sep. 2016, doi: 10.1016/j.jmst.2016.05.003.

[73] L. Xu, X. Liu, K. Sun, R. Fu, and G. Wang, “Corrosion Behavior in Magnesium-Based Alloys for Biomedical Applications,” *Materials*, vol. 15, no. 7. MDPI, Apr. 01, 2022. doi: 10.3390/ma15072613.

[74] X. Kang, S. Liu, Z. Dai, Y. He, X. Song, and Z. Tan, “Titanium dioxide: From engineering to applications,” *Catalysts*, vol. 9, no. 2. MDPI, Feb. 01, 2019. doi: 10.3390/catal9020191.

[75] L. White, Y. Koo, Y. Yun, and J. Sankar, “TiO2 deposition on AZ31 magnesium alloy using plasma electrolytic oxidation,” *J Nanomater*, vol. 2013, 2013, doi: 10.1155/2013/319437.

[76] P. Amaravathy, S. Sathyanarayanan, S. Sowndarya, and N. Rajendran, “Bioactive HA/TiO2 coating on magnesium alloy for biomedical applications,” *Ceram Int*, vol. 40, no. 5, pp. 6617–6630, Jun. 2014, doi: 10.1016/j.ceramint.2013.11.119.

[77] A. J. Haider, Z. N. Jameel, and I. H. M. Al-Hussaini, “Review on: Titanium dioxide applications,” in *Energy Procedia*, Elsevier Ltd, 2019, pp. 17–29. doi: 10.1016/j.egypro.2018.11.159.

[78] J. Sánchez-Bodón, J. A. Del Olmo, J. M. Alonso, I. Moreno-Benítez, J. L. Vilas-Vilela, and L. Pérez-Álvarez, “Bioactive Coatings on Titanium: A Review on Hydroxylation, Self-Assembled Monolayers (SAMs) and Surface Modification Strategies,” *Polymers (Basel)*, vol. 14, no. 1, Jan. 2022, doi: 10.3390/polym14010165.

[79] A. Fujishima, X. Zhang, and D. A. Tryk, “TiO2 photocatalysis and related surface phenomena,” *Surface Science Reports*, vol. 63, no. 12. pp. 515–582, Dec. 15, 2008. doi: 10.1016/j.surfrep.2008.10.001.

[80] T. L. Thompson and J. T. Yates, “Surface science studies of the photoactivation of TIO2 - New photochemical processes,” *Chemical Reviews*, vol. 106, no. 10. pp. 4428–4453, Oct. 2006. doi: 10.1021/cr050172k.

[81] F. U. Rehman, C. Zhao, H. Jiang, and X. Wang, “Biomedical applications of nano-titania in theranostics and photodynamic therapy,” *Biomaterials Science*, vol. 4, no. 1. Royal Society of Chemistry, pp. 40–54, Jan. 01, 2016. doi: 10.1039/c5bm00332f.

[82] Z. Fei Yin, L. Wu, H. Gui Yang, and Y. Hua Su, “Recent progress in biomedical applications of titanium dioxide,” *Physical Chemistry Chemical Physics*, vol. 15, no. 14. pp. 4844–4858, Apr. 14, 2013. doi: 10.1039/c3cp43938k.

[83] P. Amaravathy, C. Rose, S. Sathiyanarayanan, and N. Rajendran, “Evaluation of in vitro bioactivity and MG63 Oesteoblast cell response for TiO2 coated magnesium alloys,” *J Solgel Sci Technol*, vol. 64, no. 3, pp. 694–703, Dec. 2012, doi: 10.1007/s10971-012-2904-6.

[84] M. Daroonparvar *et al.*, “Corrosion resistance investigation of nanostructured Si- and Si/TiO 2-coated Mg alloy in 3.5% NaCl solution,” *Vacuum*, vol. 108, pp. 61–65, 2014, doi: 10.1016/j.vacuum.2014.05.020.

[85] H. R. Bakhsheshi-Rad *et al.*, “In vitro degradation behavior, antibacterial activity and cytotoxicity of TiO2-MAO/ZnHA composite coating on Mg alloy for orthopedic implants,” *Surf Coat Technol*, vol. 334, pp. 450–460, Jan. 2018, doi: 10.1016/j.surfcoat.2017.11.027.

[86] L. C. Córdoba, M. F. Montemor, and T. Coradin, “Silane/TiO2 coating to control the corrosion rate of magnesium alloys in simulated body fluid,” *Corros Sci*, vol. 104, pp. 152–161, Mar. 2016, doi: 10.1016/j.corsci.2015.12.006.

[87] M. I. Hamil, M. A. Siyah, and M. K. Khalaf, “Electrophoretic deposition of thin film TiO2 on Ti6AL4V alloy surface for biomedical applications,” *Egypt J Chem*, vol. 63, no. 8, pp. 2959–2964, 2020, doi: 10.21608/ejchem.2020.21569.2284.

[88] M. Peron, A. Bin Afif, A. Dadlani, F. Berto, and J. Torgersen, “Comparing physiologically relevant corrosion performances of Mg AZ31 alloy protected by ALD and sputter coated TiO2,” *Surf Coat Technol*, vol. 395, Aug. 2020, doi: 10.1016/j.surfcoat.2020.125922.

[89] M. Peron, R. Bertolini, and S. Cogo, “On the corrosion, stress corrosion and cytocompatibility performances of ALD TiO2 and ZrO2 coated magnesium alloys,” *J Mech Behav Biomed Mater*, vol. 125, Jan. 2022, doi: 10.1016/j.jmbbm.2021.104945.

[90] L. Y. Cui *et al.*, “Electrodeposition of TiO2 layer-by-layer assembled composite coating and silane treatment on Mg alloy for corrosion resistance,” *Surf Coat Technol*, vol. 324, pp. 560–568, Sep. 2017, doi: 10.1016/j.surfcoat.2017.06.015.

[91] U. Diebold, “The surface science of titanium dioxide.”

[92] A. Kubacka, M. Fernández-García, and G. Colón, “Advanced nanoarchitectures for solar photocatalytic applications,” *Chemical Reviews*, vol. 112, no. 3. pp. 1555–1614, Mar. 14, 2012. doi: 10.1021/cr100454n.

[93] A. Kiejna, T. Pabisiak, and S. W. Gao, “The energetics and structure of rutile TiO2(110),” *Journal of Physics Condensed Matter*, vol. 18, no. 17, pp. 4207–4217, May 2006, doi: 10.1088/0953-8984/18/17/009.

[94] M. Jokinen, M. Pätsi, H. Rahiala, T. Peltola, M. Ritala, and J. B. Rosenholm, “Influence of sol and surface properties on in vitro bioactivity of sol- gel-derived TiO2 and TiO2-SiO2 films deposited by dip-coating method,” *J Biomed Mater Res*, vol. 42, no. 2, pp. 295–302, Nov. 1998, doi: 10.1002/(SICI)1097-4636(199811)42:2<295::AID-JBM15>3.0.CO;2-I.

[95] N. Singh, U. Batra, K. Kumar, and A. Mahapatro, “Investigating TiO2–HA–PCL hybrid coating as an efficient corrosion resistant barrier of ZM21 Mg alloy,” *Journal of Magnesium and Alloys*, vol. 9, no. 2, pp. 627–646, Mar. 2021, doi: 10.1016/J.JMA.2020.08.003.

[96] L. Huang, K. Su, Y. F. Zheng, K. W. K. Yeung, and X. M. Liu, “Construction of TiO2/silane nanofilm on AZ31 magnesium alloy for controlled degradability and enhanced biocompatibility,” *Rare Metals*, vol. 38, no. 6, pp. 588–600, Jun. 2019, doi: 10.1007/s12598-018-1187-7.

[97] T. Rajh, N. M. Dimitrijevic, M. Bissonnette, T. Koritarov, and V. Konda, “Titanium dioxide in the service of the biomedical revolution,” *Chemical Reviews*, vol. 114, no. 19. American Chemical Society, pp. 10177–10216, Oct. 08, 2014. doi: 10.1021/cr500029g.

[98] D. Reyes-Coronado, G. Rodríguez-Gattorno, M. E. Espinosa-Pesqueira, C. Cab, R. De Coss, and G. Oskam, “Phase-pure TiO2 nanoparticles: Anatase, brookite and rutile,” *Nanotechnology*, vol. 19, no. 14, Apr. 2008, doi: 10.1088/0957-4484/19/14/145605.

[99] N. Lu, Z. Zhu, X. Zhao, R. Tao, X. Yang, and Z. Gao, “Nano titanium dioxide photocatalytic protein tyrosine nitration: A potential hazard of TiO2 on skin,” *Biochem Biophys Res Commun*, vol. 370, no. 4, pp. 675–680, Jun. 2008, doi: 10.1016/j.bbrc.2008.04.010.

[100] B. C. Schanen, A. S. Karakoti, S. Seal, D. R. Drake, W. L. Warren, and W. T. Self, “Exposure to titanium dioxide nanomaterials provokes inflammation of an in vitro human immune construct,” *ACS Nano*, vol. 3, no. 9, pp. 2523–2532, Sep. 2009, doi: 10.1021/nn900403h.

[101] B. Dong *et al.*, “Wire arc additive manufacturing of Al-Zn-Mg-Cu alloy: Microstructures and mechanical properties,” *Addit Manuf*, vol. 36, Dec. 2020, doi: 10.1016/j.addma.2020.101447.

[102] H. May, Y. Alper Kati, G. Gumussuyu, T. Yunus Emre, M. Unal, and O. Kose, “Bioabsorbable magnesium screw versus conventional titanium screw fixation for medial malleolar fractures,” *Journal of Orthopaedics and Traumatology*, vol. 21, no. 1, Dec. 2020, doi: 10.1186/s10195-020-00547-7.

[103] M. Kaseem, T. Zehra, B. Dikici, A. Dafali, H. W. Yang, and Y. G. Ko, "Improving the electrochemical stability of AZ31 Mg alloy in a 3.5wt.% NaCl solution via the surface functionalization of plasma electrolytic oxidation coating," *Journal of Magnesium and Alloys*, vol. 10, no. 5, pp. 1311–1325, May 2022, doi: 10.1016/J.JMA.2021.08.028.

[104] Y. Su *et al.*, "Bioinspired surface functionalization of metallic biomaterials," *Journal of the Mechanical Behavior of Biomedical Materials*, vol. 77. Elsevier Ltd, pp. 90–105, Jan. 01, 2018. doi: 10.1016/j.jmbbm.2017.08.035.

[105] S. Hou, "Solvothermal fabrication of TiO2 nanosheet films on degradable Mg–Zn alloys," *Surface Engineering*, vol. 32, no. 10, pp. 745–749, Oct. 2016, doi: 10.1080/02670844.2015.1134855.

[106] S. Hou, W. Yu, Z. Yang, Y. Li, L. Yang, and S. Lang, "Properties of titanium oxide coating on mgzn alloy by magnetron sputtering for stent application," *Coatings*, vol. 10, no. 10, pp. 1–10, Oct. 2020, doi: 10.3390/coatings10100999.

[107] S. Park, J. Park, J. Heo, B. Y. Hong, and J. Hong, "Growth behaviors and biocidal properties of titanium dioxide films depending on nucleation duration in liquid phase deposition," *Appl Surf Sci*, vol. 425, pp. 547–552, Dec. 2017, doi: 10.1016/j.apsusc.2017.07.043.

[108] W. Q. Yu, J. Qiu, L. Xu, and F. Q. Zhang, "Corrosion behaviors of TiO2 nanotube layers on titanium in Hank's solution," *Biomedical Materials*, vol. 4, no. 6, 2009, doi: 10.1088/1748-6041/4/6/065012.

[109] M. Samiee, A. Noori, Z. S. Seyedraoufi, and M. J. Eshraghi, "Enhanced biocompatibility of biodegradable magnesium alloy modified by TiO2-MgO-GO coating," *Journal of the Australian Ceramic Society*, vol. 60, no. 1, pp. 231–238, Feb. 2024, doi: 10.1007/s41779-023-00960-1.

[110] V. Vishwakarma, G. S. Kaliaraj, and K. K. Amirtharaj Mosas, "Multifunctional Coatings on Implant Materials—A Systematic Review of the Current Scenario," *Coatings*, vol. 13, no. 1. MDPI, Jan. 01, 2023. doi: 10.3390/coatings13010069.

[111] Y. Tao and B. Zhu, "Titanium Oxide Films Prepared by Cathodic Electrodeposition Method," *J Electron Mater*, vol. 49, no. 12, pp. 7526–7531, Dec. 2020, doi: 10.1007/s11664-020-08513-z.

[112] C. D. Lokhande, S.-K. Min, K.-D. Jung, and O.-S. Joo, "Cathodic electrodeposition of amorphous titanium oxide films from an alkaline solution bath."

[113] L. Mohan, D. Durgalakshmi, M. Geetha, T. S. N. Sankara Narayanan, and R. Asokamani, "Electrophoretic deposition of nanocomposite (HAp + TiO2) on titanium alloy for biomedical applications," *Ceram Int*, vol. 38, no. 4, pp. 3435–3443, May 2012, doi: 10.1016/J.CERAMINT.2011.12.056.

[114] T. H. Wang, A. M. Navarrete-López, S. Li, D. A. Dixon, and J. L. Gole, "Hydrolysis of TiCl4: Initial steps in the production of TiO 2," *Journal of Physical Chemistry A*, vol. 114, no. 28, pp. 7561–7570, Jul. 2010, doi: 10.1021/jp102020h.

[115] L. Y. Niu, Z. H. Jiang, G. Y. Li, C. D. Gu, and J. S. Lian, "A study and application of zinc phosphate coating on AZ91D magnesium alloy," *Surf Coat Technol*, vol. 200, no. 9, pp. 3021–3026, Feb. 2006, doi: 10.1016/J.SURFCOAT.2004.10.119.

[116] J. A. Cabral-Miramontes *et al.*, "Corrosion behavior of Zn-TiO 2 and Zn-ZnO Electrodeposited coatings in 3.5% NaCl solution," *Int J Electrochem Sci*, vol. 14, no. 5, pp. 4226–4239, 2019, doi: 10.20964/2019.05.10.

[117] C. Das, E. Kastania, J. Witt, and O. Ozcan, "Corrosion protection properties of poly(4-vinyl pyridine) containing multilayer polymeric coatings on magnesium alloy AZ31," *Materials and Corrosion*, vol. 73, no. 3, pp. 427–435, Mar. 2022, doi: 10.1002/maco.202112708.

[118] L. Kouisni, M. Azzi, M. Zertoubi, F. Dalard, and S. Maximovitch, "Phosphate coatings on magnesium alloy AM60 part 1: study of the formation and the growth of zinc phosphate films," *Surf Coat Technol*, vol. 185, no. 1, pp. 58–67, Jul. 2004, doi: 10.1016/J.SURFCOAT.2003.10.061.

[119] Z. Lin, T. Wang, X. Yu, X. Sun, and H. Yang, "Functionalization treatment of micro-arc oxidation coatings on magnesium alloys: a review," *J Alloys Compd*, vol. 879, p. 160453, Oct. 2021, doi: 10.1016/J.JALLCOM.2021.160453.

[120] M. S. Safavi, F. C. Walsh, L. Visai, and J. Khalil-Allafi, "Progress in Niobium Oxide-Containing Coatings for Biomedical Applications: A Critical Review," *ACS Omega*, vol. 7, no. 11. American Chemical Society, pp. 9088–9107, Mar. 22, 2022. doi: 10.1021/acsomega.2c00440.

[121] A. Kar, K. S. Raja, and M. Misra, "Electrodeposition of hydroxyapatite onto nanotubular TiO2 for implant applications," *Surf Coat Technol*, vol. 201, no. 6, pp. 3723–3731, Dec. 2006, doi: 10.1016/j.surfcoat.2006.09.008.

[122] B. M. Praveen and T. V. Venkatesha, "Electrodeposition and properties of Zn-nanosized TiO 2 composite coatings," *Appl Surf Sci*, vol. 254, no. 8, pp. 2418–2424, Feb. 2008, doi: 10.1016/j.apsusc.2007.09.047.

[123] M. Lubas, J. J. Jasinski, M. Sitarz, L. Kurpaska, P. Podsiad, and J. Jasinski, "Raman spectroscopy of TiO2 thin films formed by hybrid treatment for biomedical applications," in *Spectrochimica Acta - Part A: Molecular and Biomolecular Spectroscopy*, Elsevier, Dec. 2014, pp. 867–871. doi: 10.1016/j.saa.2014.05.045.

[124] F. Tian, Y. Zhang, J. Zhang, and C. Pan, "Raman spectroscopy: A new approach to measure the percentage of anatase TiO2 exposed (001) facets," *Journal of Physical Chemistry C*, vol. 116, no. 13, pp. 7515–7519, Apr. 2012, doi: 10.1021/jp301256h.

[125] L. G. Bland, K. Gusieva, and J. R. Scully, “Effect of Crystallographic Orientation on the Corrosion of Magnesium: Comparison of Film Forming and Bare Crystal Facets using Electrochemical Impedance and Raman Spectroscopy,” *Electrochim Acta*, vol. 227, pp. 136–151, Feb. 2017, doi: 10.1016/J.ELECTACTA.2016.12.107.

[126] S. Ebnesajjad, “Surface and Material Characterization Techniques,” *Handbook of Adhesives and Surface Preparation: Technology, Applications and Manufacturing*, pp. 31–48, Jan. 2011, doi: 10.1016/B978-1-4377-4461-3.10004-5.

[127] J. Chang and Y. L. Zhou, “Surface modification of bioactive glasses,” *Bioactive Glasses*, pp. 119–143, Jan. 2018, doi: 10.1016/B978-0-08-100936-9.00008-3.

[128] T. Theivasanthi and M. Alagar, “Titanium dioxide (TiO 2) Nanoparticles-XRD Analyses-An Insight.”

[129] M. A. Aramendıá *et al.*, “XRD and Solid-State NMR Study of Magnesium Oxide-Magnesium Orthophosphate Systems,” 1998.

[130] K. Thamaphat, P. Limsuwan, and B. Ngotawornchai, “Phase Characterization of TiO 2 Powder by XRD and TEM,” 2008.

[131] P. S. Nnamchi and C. S. Obayi, “Electrochemical Characterization of Nanomaterials,” *Characterization of Nanomaterials: Advances and Key Technologies*, pp. 103–127, Jan. 2018, doi: 10.1016/B978-0-08-101973-3.00004-3.

[132] Y. S. Choudhary, L. Jothi, and G. Nageswaran, “Electrochemical Characterization,” *Spectroscopic Methods for Nanomaterials Characterization*, vol. 2, pp. 19–54, Jan. 2017, doi: 10.1016/B978-0-323-46140-5.00002-9.

[133] P. T. Kissinger and W. R. Heineman, “Cyclic Voltammetry.” [Online]. Available: https://pubs.acs.org/sharingguidelines

[134] L. Y. Cui *et al.*, “Electrodeposition of TiO2 layer-by-layer assembled composite coating and silane treatment on Mg alloy for corrosion resistance,” *Surf Coat Technol*, vol. 324, pp. 560–568, Sep. 2017, doi: 10.1016/j.surfcoat.2017.06.015.

[135] P. Amaravathy, S. Sathyanarayanan, S. Sowndarya, and N. Rajendran, “Bioactive HA/TiO2 coating on magnesium alloy for biomedical applications,” *Ceram Int*, vol. 40, no. 5, pp. 6617–6630, Jun. 2014, doi: 10.1016/j.ceramint.2013.11.119.

[136] S. Agarwal, J. Curtin, B. Duffy, and S. Jaiswal, “Biodegradable magnesium alloys for orthopaedic applications: A review on corrosion, biocompatibility and surface modifications,” *Materials Science and Engineering: C*, vol. 68, pp. 948–963, Nov. 2016, doi: 10.1016/J.MSEC.2016.06.020.

[137] H. J. An, S. R. Jang, R. Vittal, J. Lee, and K. J. Kim, “Cationic surfactant promoted reductive electrodeposition of nanocrystalline anatase TiO2 for application to dye-sensitized solar cells,” *Electrochim Acta*, vol. 50, no. 13, pp. 2713–2718, Apr. 2005, doi: 10.1016/j.electacta.2004.11.017.

[138] J. B. Zhong, J. Z. Li, F. M. Feng, S. T. Huang, and J. Zeng, “CTAB-assisted fabrication of TiO2 with improved photocatalytic performance,” *Mater Lett*, vol. 100, pp. 195–197, 2013, doi: 10.1016/j.matlet.2013.03.030.

[139] Y. Zou, Y. Li, N. Zhang, and X. Liu, “Flower-like CuO synthesized by CTAB-assisted hydrothermal method,” 2011.

[140] D. Ning, A. Zhang, M. Murtaza, and H. Wu, “Effect of surfactants on the electrodeposition of Cu-TiO2 composite coatings prepared by jet electrodeposition,” *J Alloys Compd*, vol. 777, pp. 1245–1250, Mar. 2019, doi: 10.1016/j.jallcom.2018.11.077.

[141] K. D. Dobson, A. D. Roddick-Lanzilotta, and A. J. McQuillan, “An in situ infrared spectroscopic investigation of adsorption of sodium dodecylsulfate and of cetyltrimethylammonium bromide surfactants to TiO2, ZrO2, Al2O3, and Ta2O5 particle films from aqueous solutions,” *Vib Spectrosc*, vol. 24, no. 2, pp. 287–295, Dec. 2000, doi: 10.1016/S0924-2031(00)00096-5.

[142] J. Yuenyongsuwan, N. Nithiyakorn, P. Sabkird, E. A. O’Rear, and T. Pongprayoon, “Surfactant effect on phase-controlled synthesis and photocatalyst property of TiO2 nanoparticles,” *Mater Chem Phys*, vol. 214, pp. 330–336, Aug. 2018, doi: 10.1016/j.matchemphys.2018.04.111.

[143] C. R. C. HAK, D. N. E. FATANAH, Y. ABDULLAH, and M. Y. M. SULAIMAN, “The Effect of Surfactants on the Stability of TiO2 Aqueous Suspension,” *International Journal of Current Research in Science, Engineering & Technology*, vol. 1, no. Spl-1, p. 172, Mar. 2018, doi: 10.30967/ijcrset.1.s1.2018.172-178.

[144] S. Sugapriya, R. Sriram, and S. Lakshmi, “Effect of annealing on TiO2 nanoparticles,” *Optik (Stuttg)*, vol. 124, no. 21, pp. 4971–4975, Nov. 2013, doi: 10.1016/j.ijleo.2013.03.040.

[145] F. Guillemot, M. C. Porté, C. Labrugère, and C. Baquey, “Ti4+ to Ti3+ conversion of TiO2 uppermost layer by low-temperature vacuum annealing: Interest for titanium biomedical applications,” *J Colloid Interface Sci*, vol. 255, no. 1, pp. 75–78, 2002, doi: 10.1006/jcis.2002.8623.

[146] J. Zhang, M. Li, Z. Feng, J. Chen, and C. Li, “UV raman spectroscopic study on TiO2- I. phase transformation at the surface and in the bulk,” *Journal of Physical Chemistry B*, vol. 110, no. 2, pp. 927–935, Jan. 2006, doi: 10.1021/jp0552473.

[147] J. Moreno *et al.*, “In vitro characterization of anodized magnesium alloy as a potential biodegradable material for biomedical applications,” *Electrochim Acta*, vol. 437, Jan. 2023, doi: 10.1016/j.electacta.2022.141463.

[148] H. T. Teng, T. J. Li, X. L. Zhang, and Z. T. Zhang, “Influence of sub-rapid solidification on microstructure and mechanical properties of AZ61A magnesium alloy,” *Transactions of Nonferrous Metals Society of China (English Edition)*, vol. 18, no. SPEC. ISSUE 1, 2008, doi: 10.1016/s1003-6326(10)60180-x.

[149] S. Bagheri, K. Shameli, and S. B. Abd Hamid, “Synthesis and characterization of anatase titanium dioxide nanoparticles using egg white solution via Sol-Gel method,” *J Chem*, 2013, doi: 10.1155/2013/848205.

[150] P. I. Peng, “A PHYSICAL MODEL FOR EXPERIMENTAL X-RAY DIFFRACTION MEASUREMENTS OF TiO 2 THIN FILMS GROWN ON SrTiO 3 SUBSTRATE VIA PULSED LASER DEPOSITION,” 2018.

[151] M. J. Fernandus, T. Senthilkumar, V. Balasubramanian, and S. Rajakumar, “Optimizing diffusion bonding parameters to maximize the strength of aa6061 aluminum and AZ61A magnesium alloy joints,” *Exp Tech*, vol. 38, no. 4, pp. 21–36, 2014, doi: 10.1111/j.1747-1567.2012.00815.x.

[152] S. Rajakumar, V. Balasubramanian, and A. Razalrose, “Friction stir and pulsed current gas metal arc welding of AZ61A magnesium alloy: A comparative study,” *Mater Des*, vol. 49, pp. 267–278, 2013, doi: 10.1016/j.matdes.2013.01.051.

[153] A. Dhanapal, S. Rajendra Boopathy, and V. Balasubramanian, “Influence of pH value, chloride ion concentration and immersion time on corrosion rate of friction stir welded AZ61A magnesium alloy weldments,” *Journal of Alloys and Compounds*, vol. 523. pp. 49–60, May 15, 2012. doi: 10.1016/j.jallcom.2012.01.070.

[154] A. El-Morsy, A. Ismail, and M. Waly, “Microstructural and mechanical properties evolution of magnesium AZ61 alloy processed through a combination of extrusion and thermomechanical processes,” *Materials Science and Engineering: A*, vol. 486, no. 1–2, pp. 528–533, Jul. 2008, doi: 10.1016/j.msea.2007.09.044.

[155] S. J. Huang, M. Subramani, A. N. Ali, D. B. Alemayehu, J. N. Aoh, and P. C. Lin, “The Effect of Micro-SiCp Content on the Tensile and Fatigue Behavior of AZ61 Magnesium Alloy Matrix Composites,” *International Journal of Metalcasting*, vol. 15, no. 3, pp. 780–793, Jul. 2021, doi: 10.1007/s40962-020-00508-0.

[156] W. Promnopas *et al.*, “Crystalline phases and optical properties of titanium dioxide films deposited on glass substrates by microwave method,” *Surf Coat Technol*, vol. 306, pp. 69–74, Nov. 2016, doi: 10.1016/j.surfcoat.2016.04.078.

[157] A. Ishii, I. Oikawa, M. Imura, T. Kanai, and H. Takamura, “Magnesium doping for the promotion of rutile phase formation in the pulsed laser deposition of TiO2 thin films,” *Mater Trans*, vol. 59, no. 1, pp. 33–38, 2018, doi: 10.2320/matertrans.MB201704.

[158] N. G. Park, J. Van De Lagemaat, and A. J. Frank, “Comparison of dye-sensitized rutile- and anatase-based TiO2 solar cells,” *Journal of Physical Chemistry B*, vol. 104, no. 38, pp. 8989–8994, Sep. 2000, doi: 10.1021/jp994365l.

[159] H. G. Yang *et al.*, “Anatase TiO2 single crystals with a large percentage of reactive facets,” *Nature*, vol. 453, no. 7195, pp. 638–641, May 2008, doi: 10.1038/nature06964.

[160] S. Liu, J. Yu, and M. Jaroniec, “Anatase TiO2 with dominant high-energy {001} facets: Synthesis, properties, and applications,” *Chemistry of Materials*, vol. 23, no. 18. pp. 4085–4093, Sep. 27, 2011. doi: 10.1021/cm200597m.

[161] L. Umaralikhan and M. Jamal Mohamed Jaffar, “Green Synthesis of MgO Nanoparticles and it Antibacterial Activity,” *Iran J Sci Technol Trans A Sci*, vol. 42, no. 2, pp. 477–485, Jun. 2018, doi: 10.1007/s40995-016-0041-8.

[162] M. A. Aramendía *et al.*, “Study of MgO and Pt/MgO Systems by XRD, TPR, and 1H MAS NMR,” *Langmuir*, vol. 15, no. 4, pp. 1192–1197, 1999, doi: 10.1021/la9808972.

[163] N. Rani, S. Chahal, A. S. Chauhan, P. Kumar, R. Shukla, and S. K. Singh, “X-ray Analysis of MgO Nanoparticles by Modified Scherer’s Williamson-Hall and Size-Strain Method,” 2019. [Online]. Available: www.sciencedirect.comwww.materialstoday.com/proceedings

[164] M. R. Bindhu, M. Umadevi, M. Kavin Micheal, M. V. Arasu, and N. Abdullah Al-Dhabi, “Structural, morphological and optical properties of MgO nanoparticles for antibacterial applications,” *Mater Lett*, vol. 166, pp. 19–22, Mar. 2016, doi: 10.1016/j.matlet.2015.12.020.

[165] S. Yousefi, B. Ghasemi, and M. P. Nikolova, “Morpho/Opto-structural Characterizations and XRD-Assisted Estimation of Crystallite Size and Strain in MgO Nanoparticles by Applying Williamson–Hall and Size–Strain Techniques,” *J Clust Sci*, vol. 33, no. 5, pp. 2197–2207, Sep. 2022, doi: 10.1007/s10876-021-02144-y.

[166] M. c, J. Suresh, and R. R. Gandhi, “A COMPARATIVE STUDY ON ANTIBACTERIAL PROPERTIES OF MgO NANOPARTICLES PREPARED UNDER DIFFERENT CALCINATION TEMPERATURE.”

[167] R. Giorgi, C. Bozzi, L. Dei, C. Gabbiani, B. W. Ninham, and P. Baglioni, “Nanoparticles of Mg(OH)2: Synthesis and application to paper conservation,” *Langmuir*, vol. 21, no. 18, pp. 8495–8501, Aug. 2005, doi: 10.1021/la050564m.

[168] C. Su, X. Chen, C. Gao, and Y. Wang, “Effect of heat input on microstructure and mechanical properties of Al-Mg alloys fabricated by WAAM,” *Appl Surf Sci*, vol. 486, pp. 431–440, Aug. 2019, doi: 10.1016/J.APSUSC.2019.04.255.

[169] P. Tong, Y. Sheng, R. Hou, M. Iqbal, L. Chen, and J. Li, “Recent progress on coatings of biomedical magnesium alloy,” *Smart Mater Med*, vol. 3, pp. 104–116, Jan. 2022, doi: 10.1016/j.smaim.2021.12.007.

[170] L. Xu, E. Zhang, D. Yin, S. Zeng, and K. Yang, “In vitro corrosion behaviour of Mg alloys in a phosphate buffered solution for bone implant application,” *J Mater Sci Mater Med*, vol. 19, no. 3, pp. 1017–1025, Mar. 2008, doi: 10.1007/s10856-007-3219-y.

[171] C. Schille *et al.*, "Corrosion of experimental magnesium alloys in blood and PBS: A gravimetric and microscopic evaluation," in *Materials Science and Engineering: B*, Elsevier Ltd, Dec. 2011, pp. 1797–1801. doi: 10.1016/j.mseb.2011.04.007.

[172] K. O. Kongshaug, H. Fjellvåg, and K. P. Lillerud, "The synthesis and crystal structure of a hydrated magnesium phosphate Mg 3 (PO 4) 2 ·4H 2 O," 2001. [Online]. Available: www.elsevier.com/locate/ssscie

[173] D. A. Mikhailov, M. I. Lelet, D. G. Fukina, and Y. N. Lelet, "Photocatalytic Properties of the MgHPO4·3H2O and MgKPO4·6H2O Phosphates," *Inorganic Materials*, vol. 58, no. 6, pp. 620–629, Jun. 2022, doi: 10.1134/S0020168522060061.

[174] Y. Li, M. Sui, Y. Ding, G. Zhang, J. Zhuang, and C. Wang, "Preparation of Mg(OH)2 nanorods," *Advanced Materials*, vol. 12, no. 11, pp. 818–821, 2000, doi: 10.1002/(SICI)1521-4095(200006)12:11<818::AID-ADMA818>3.0.CO;2-L.

[175] S. Mousa, "STUDY ON SYNTHESIS OF MAGNESIUM PHOSPHATE MATERIALS," 2010.

[176] S. J. Ding, C. T. Kao, M. Y. Shie, C. Hung, and T. H. Huang, "The Physical and Cytological Properties of White MTA Mixed with Na2HPO4 as an Accelerant," *J Endod*, vol. 34, no. 6, pp. 748–751, Jun. 2008, doi: 10.1016/j.joen.2008.02.041.

[177] R. Mahajan, R. Prakash, S. Kumar, V. Kumar, R. J. Choudhary, and D. M. Phase, "Surface and luminescent properties of Mg3(PO4)2:Dy3+ phosphors," *Optik (Stuttg)*, vol. 225, Jan. 2021, doi: 10.1016/j.ijleo.2020.165717.

[178] Y. Xin, T. Hu, and P. K. Chu, "Influence of Test Solutions on In Vitro Studies of Biomedical Magnesium Alloys," *J Electrochem Soc*, vol. 157, no. 7, p. C238, 2010, doi: 10.1149/1.3421651.

[179] L. Xu, G. Yu, E. Zhang, F. Pan, and K. Yang, "In vivo corrosion behavior of Mg-Mn-Zn alloy for bone implant application," *J Biomed Mater Res A*, vol. 83, no. 3, pp. 703–711, Nov. 2007, doi: 10.1002/jbm.a.31273.

[180] M. Alvarez-Lopez *et al.*, "Corrosion behaviour of AZ31 magnesium alloy with different grain sizes in simulated biological fluids," *Acta Biomater*, vol. 6, no. 5, pp. 1763–1771, 2010, doi: 10.1016/j.actbio.2009.04.041.

[181] A. H. M. Sanchez, B. J. C. Luthringer, F. Feyerabend, and R. Willumeit, "Mg and Mg alloys: How comparable are in vitro and in vivo corrosion rates? A review," *Acta Biomaterialia*, vol. 13. Elsevier Ltd, pp. 16–31, Feb. 01, 2015. doi: 10.1016/j.actbio.2014.11.048.

[182] Y. F. Zheng, X. N. Gu, and F. Witte, "Biodegradable metals," *Materials Science and Engineering R: Reports*, vol. 77. Elsevier Ltd, pp. 1–34, 2014. doi: 10.1016/j.mser.2014.01.001.

[183] J. M. Lourenço. The NOVAthesis LATEX Template User's Manual. NOVA University Lisbon. 2021. url: https://github.com/joaomlourenco/novathesis_word/raw/master/novathesis_word-FINAL-EN.pdf.

A

ANNEX

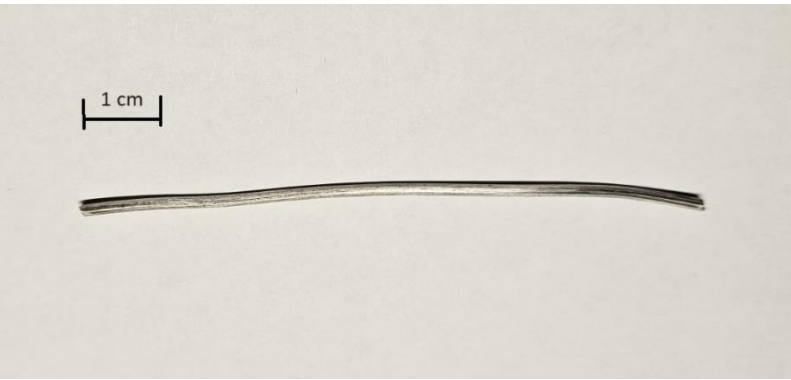

Figure A-6-1 Photograph of the filament of AZ61A alloy, used to print the WAAM substrates.

Table A-1 Parameters values for the welding process - Wire Feed Speed, Travel Speed, Contact to Work Distance, Shield Gas Flow/Rate and Voltage Trim)

WFS (m/min)	TS (mm/min)	CTWD (mm)	SGF (l/min)	ΔV (V)
3, 3.5, 4, 5.5	500, 550, 700	12, 14, 17, 19	19	-1, -4, -5

Figure A-6-2 Photograph of a printed wall (obtained from[39]).

Mechanical properties of base metals

Base metals	Crystal structure	Melting point (°C)	Density (g/CC)	Ultimate tensile strength (MPa)	Yield strength (MPa)	Shear strength (MPa)	Elongation (%)	Hardness (Hv)
AA6061	FCC	660	2.7	310	275	207	12	107
AZ61A	HCP	649	1.754	271	217	140	8.4	99

FCC, face centered cubic; HCP, hexagonal close packed.

Figure A-6-3 Mechanical Properties of AZ61A alloy (adapted from[151]).

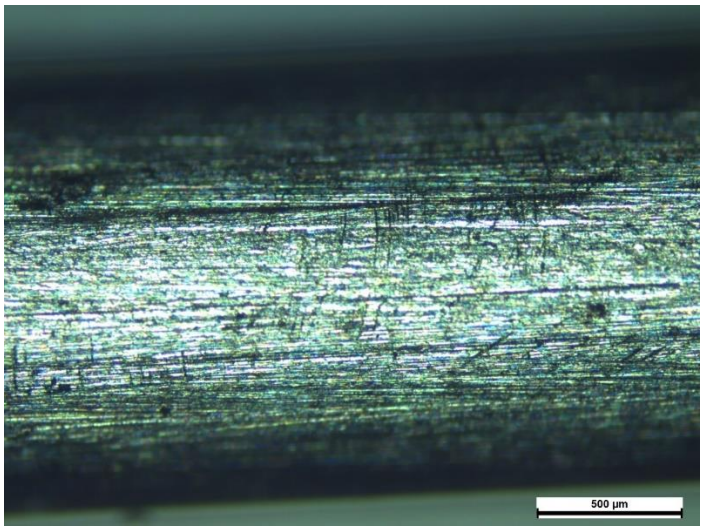

Figure A-6-4 Microscope image of the filament of AZ61A alloy, used to print the WAAM substrates (5x)

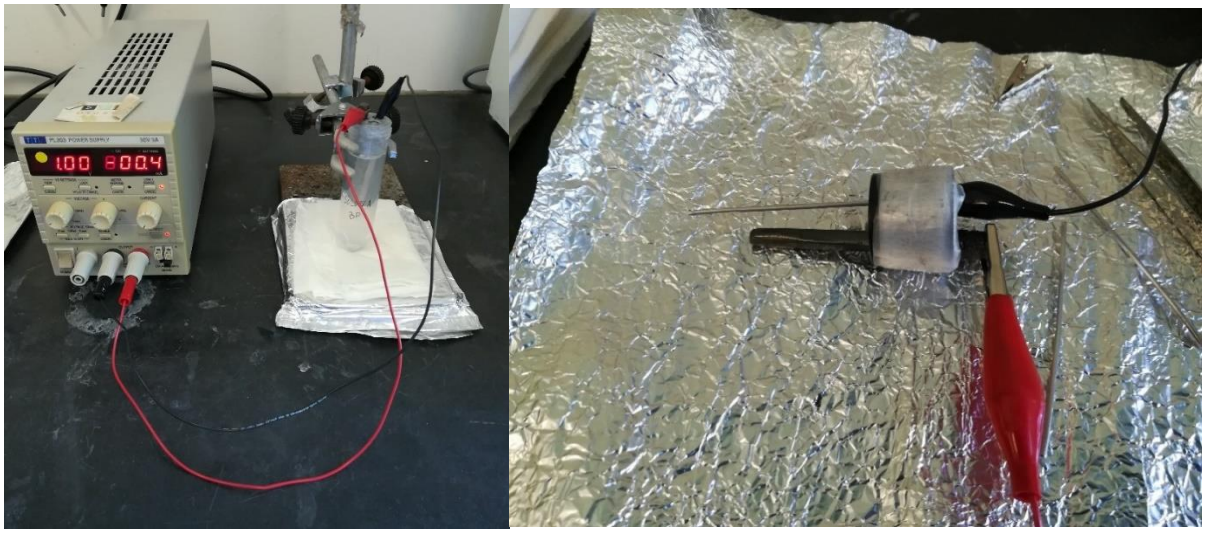

Figure A-6-5 Photograph of the Electrodeposition Set-up (left) and the detailed plastic lid (right) with the Graphite rod as a counter electrode, attached to the red wire, and the commercial alloy AZ61A (right) or the WAAM printed substrate (left) as the working electrode.

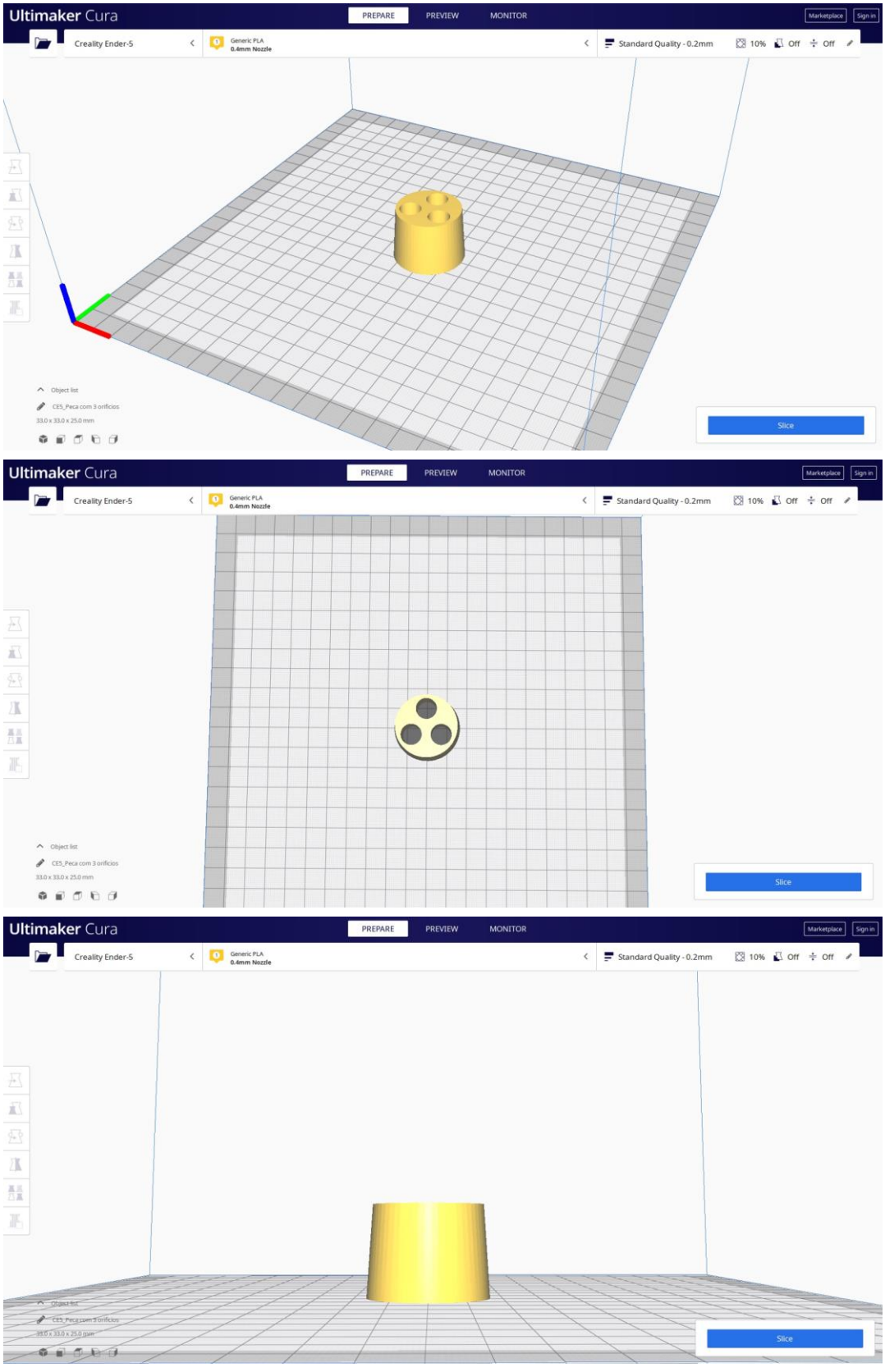

Figure A-6-6 SLT of custom plastic lid.

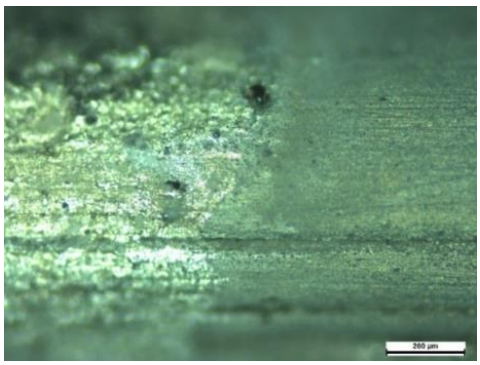

Figure A-6-7 OM image of AZ61A filament after ED at 1V for 45 minutes - Border detail (uncoated (left) and coated (right) (10x).

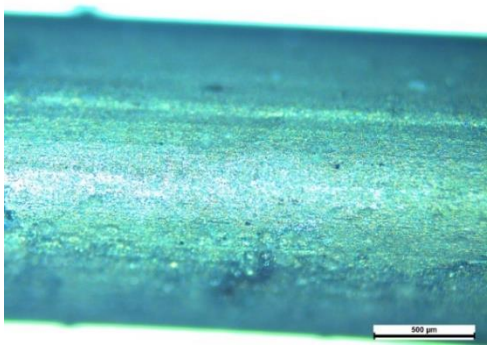

Figure A-6-8 Optic Microscope image of AZ61A alloy filament after ED at 1V for 45 minutes (5x)

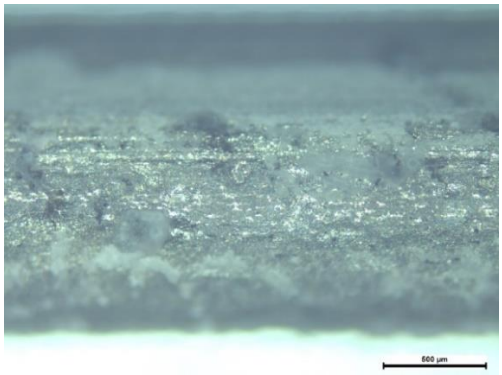

Figure A-6-9 Optic Microscope image of AZ61A alloy filament after ED at 0,5 V for 45 minutes (10x)

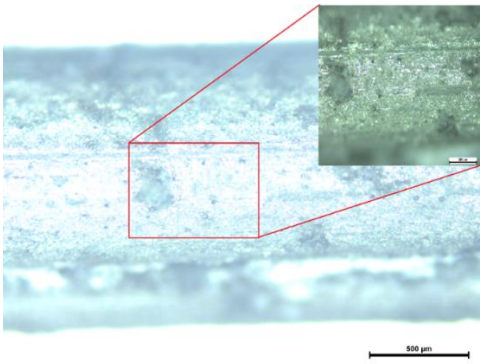

Figure A-6-10 Optic Microscope images of ED in AZ61A alloy filament at 6V for 45 minutes.

Table A-2 Optic Microscope images of AZ61A alloy filament after ED at 1 V,1.5 V and 2 V during 15 and 30 minutes (5x)

	15 minutes	**30 minutes**
1 V	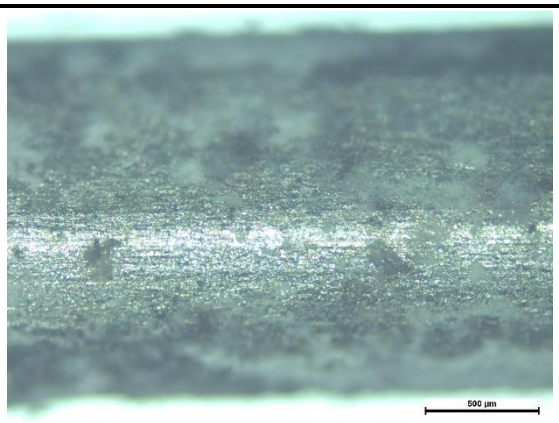	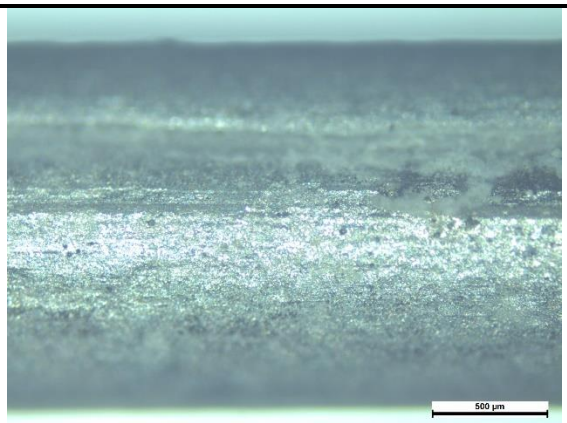
1,5V	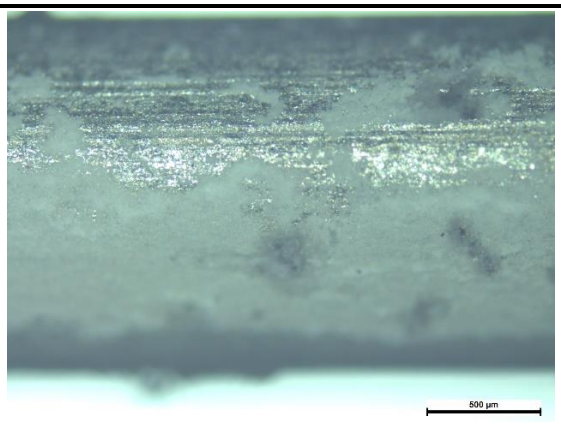	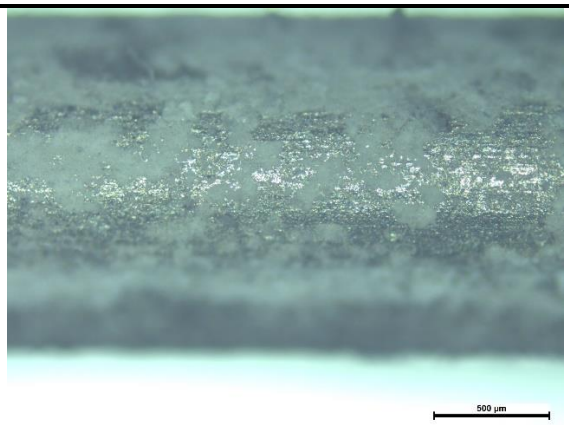
2 V	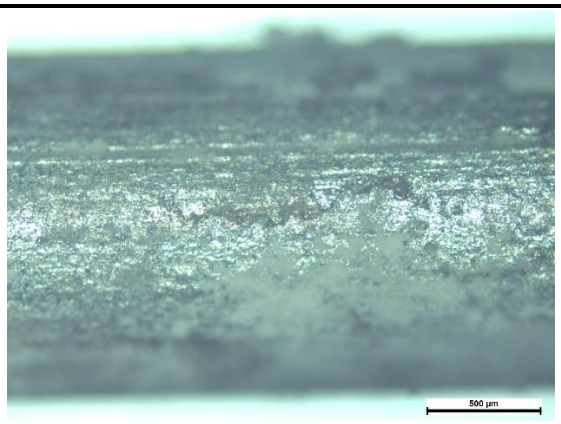	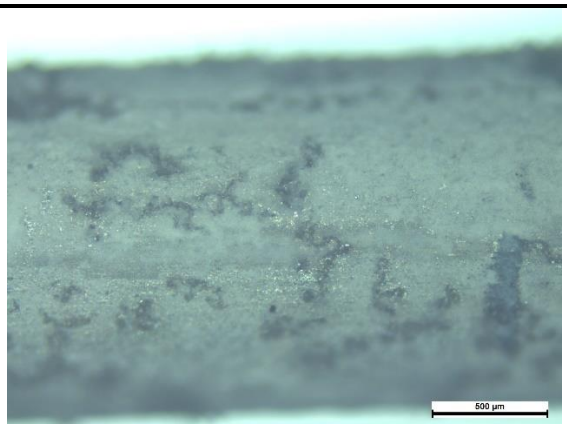

Table A-3 Optic Microscope images of AZ61A alloy filament after ED at 1 V,1.5 V and 2 V for 45 and 60 minutes (5x)

	45 minutes	**60 minutes**
1 V	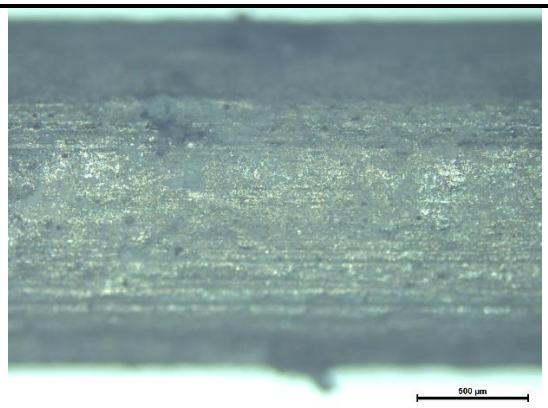	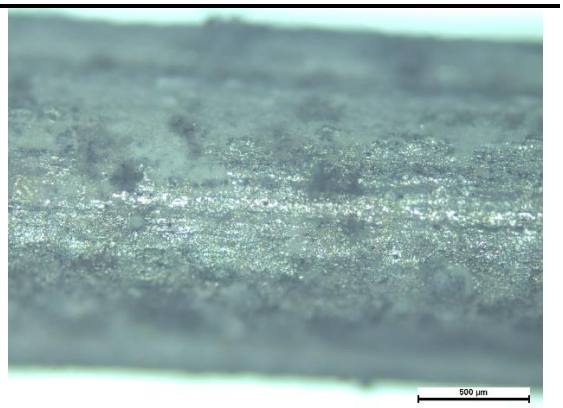
1,5 V	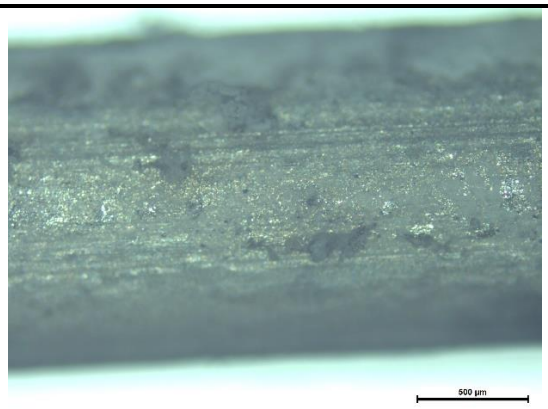	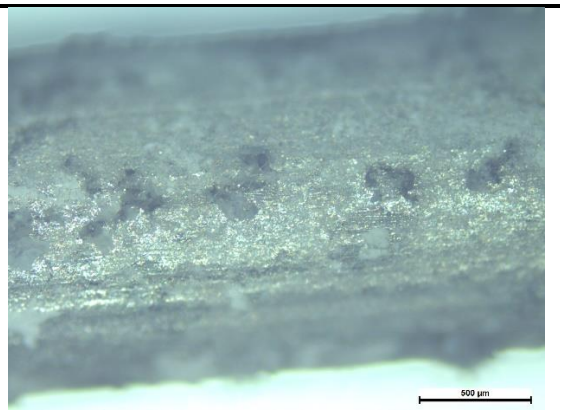
2 V	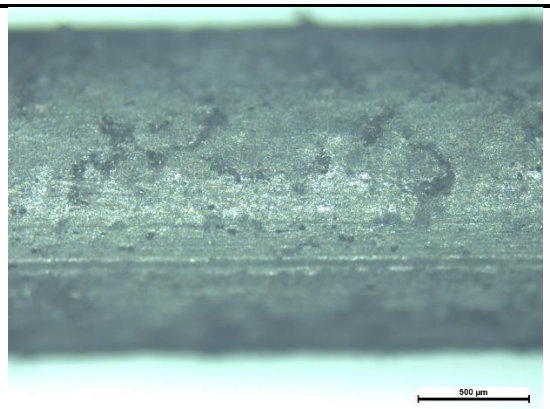	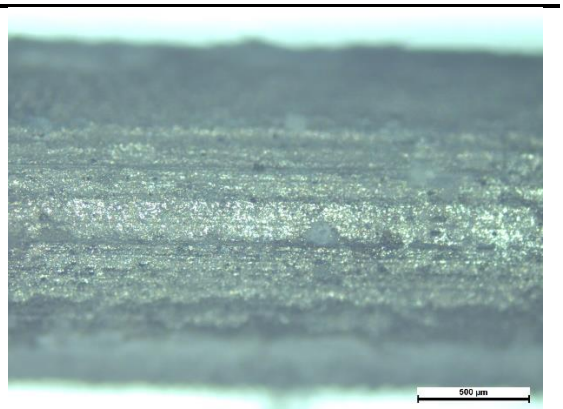

Table A-4 Optic Microscope images of AZ61A alloy filament after ED at 1 V,1.5 V and 2 V for 15 and 30 minutes (10x)

	15'	30'
1V	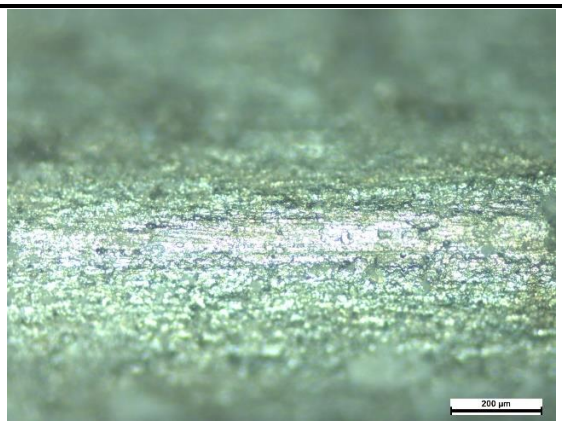	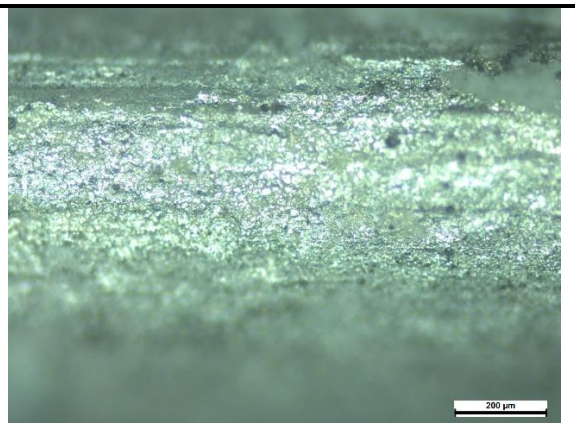
1,5V	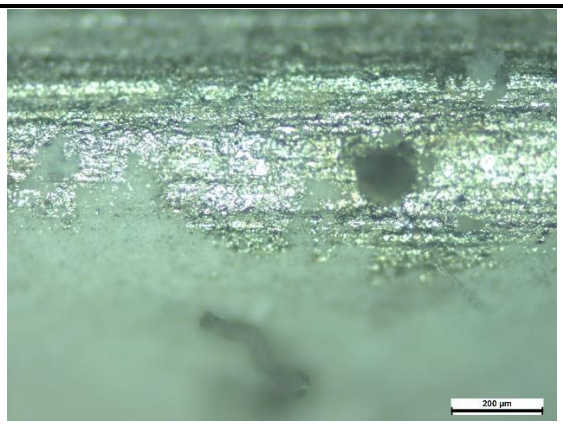	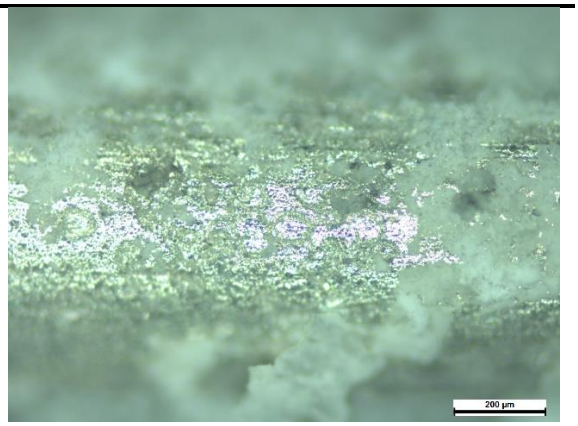
2V	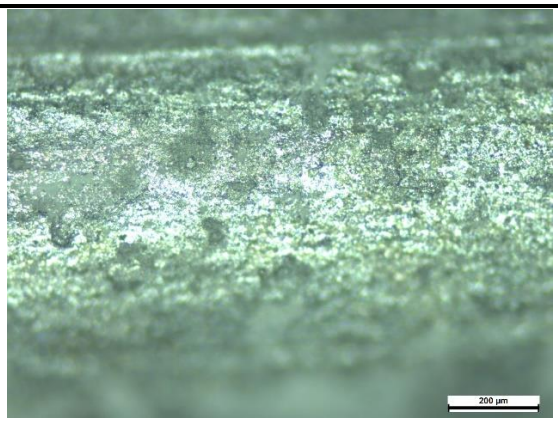	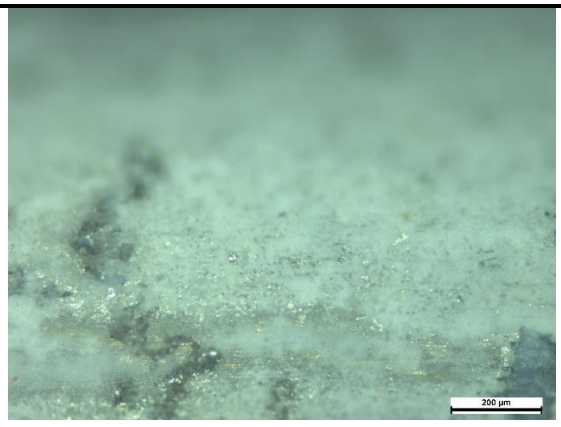

~

Table A-5 Optic Microscope images of ED in AZ61A alloy filament at 1 V,1.5 V and 2 V for 15 and 30 minutes (10x)

	45'	60'
1V	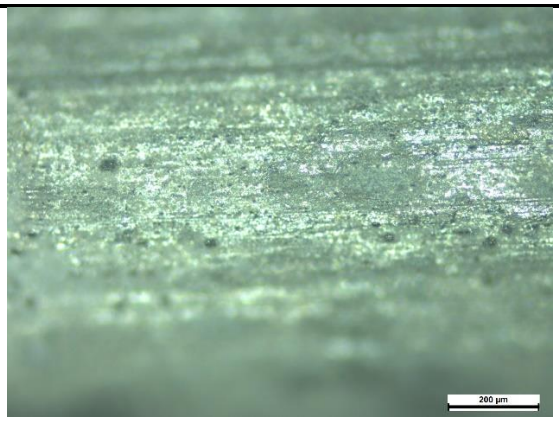	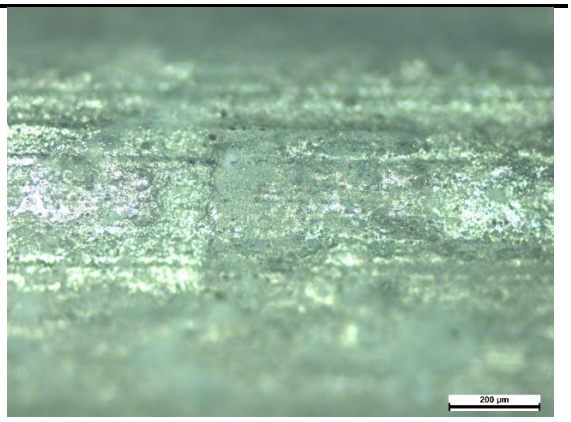
1,5V	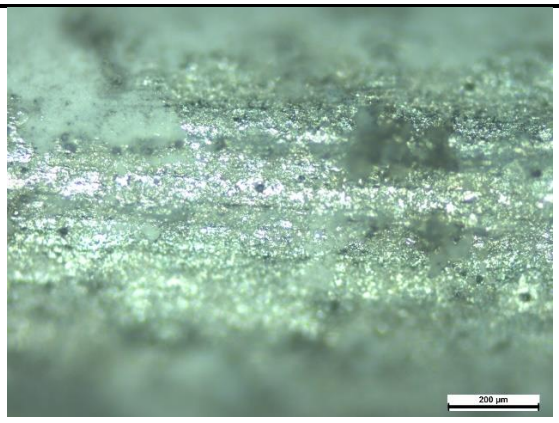	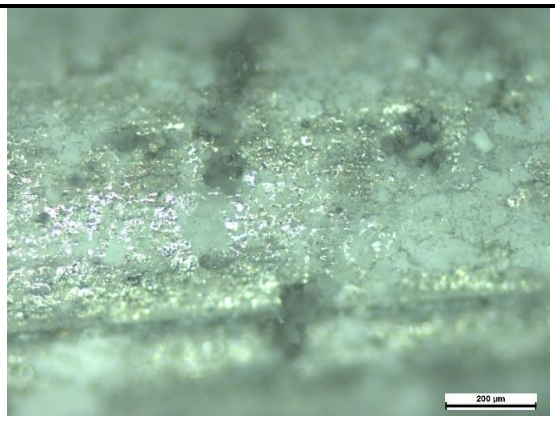
2V	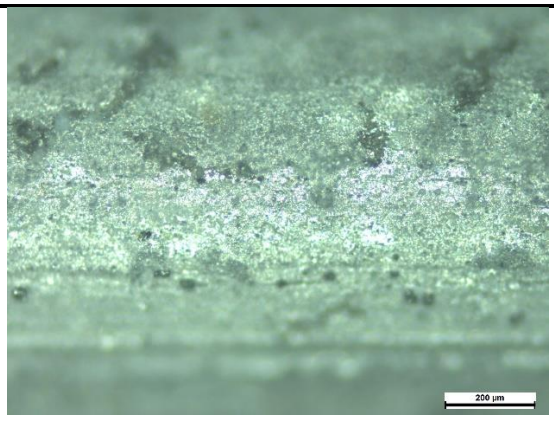	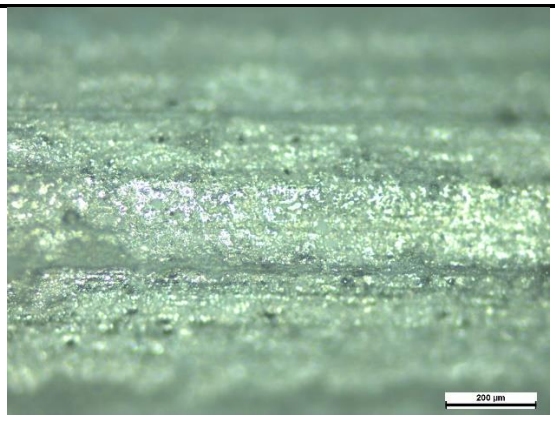

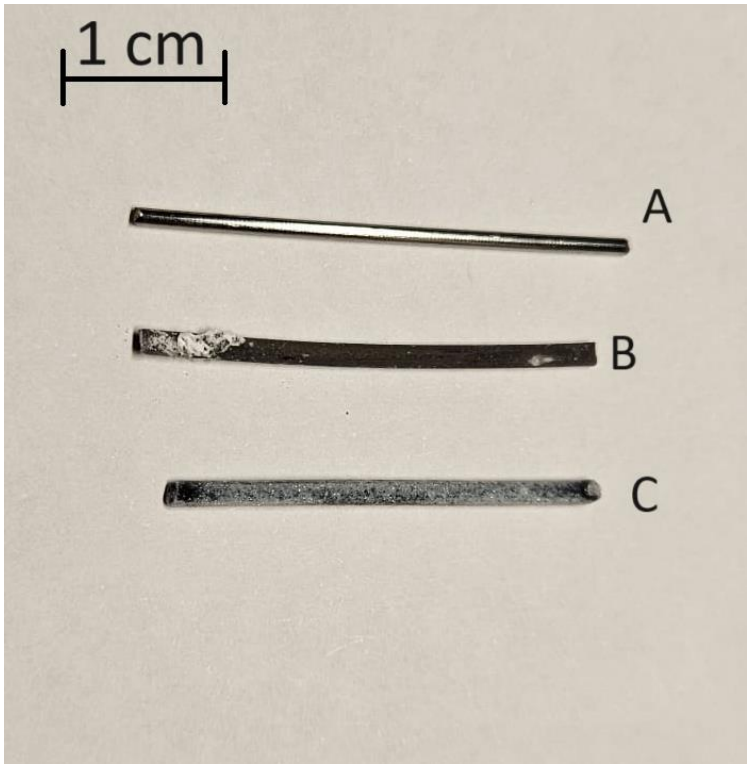

Figure A-6-11 Photograph of Titanium based filament (A), AZ61A filament with annealed TiO_2 coating (B), and uncoated AZ61A filament (C) after Degradation Tests

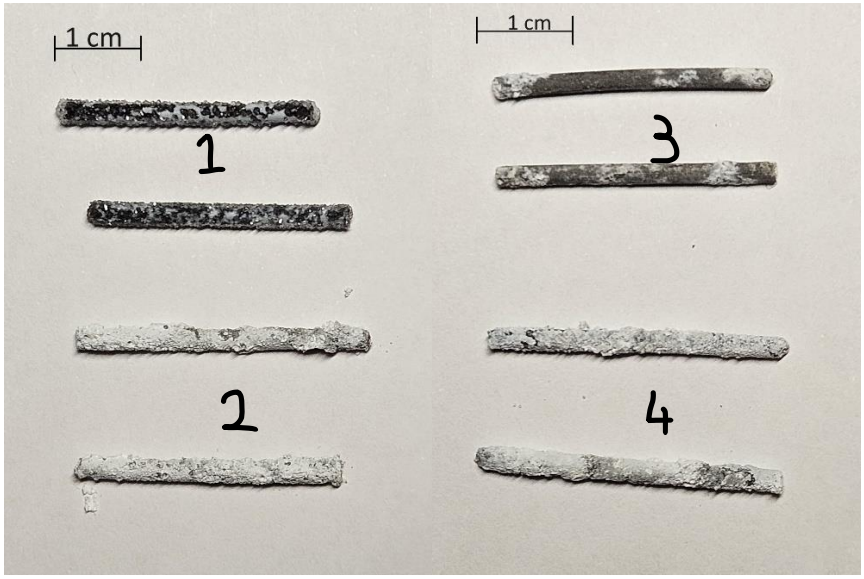

Figure A-6-12 Photograph of uncoated AZ61A filament after degradation tests in acid PBS (1) and neutral PBS(2), and AZ61A filament with annealed TiO2 coating, after degradation tests in acid (3) and neutral (4) PBS.

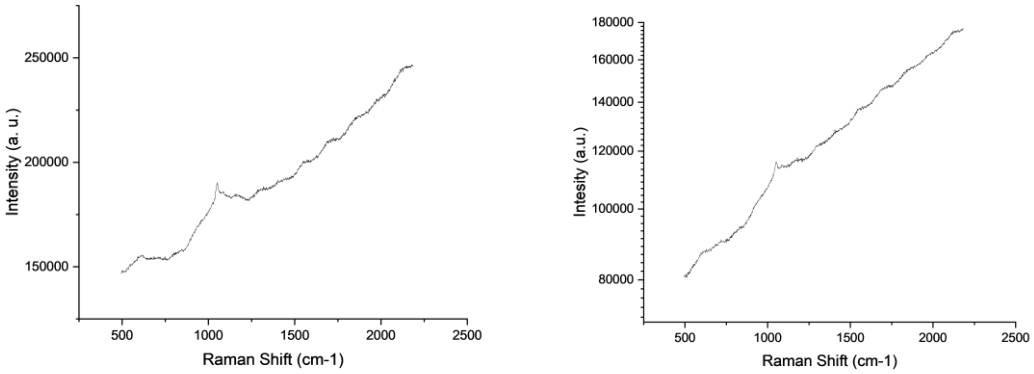

Figure A-6-13 Raman Spectroscopy of the AZ61A commercial alloy coated with TiO_2 (left) and coated WAAM substrate (right)

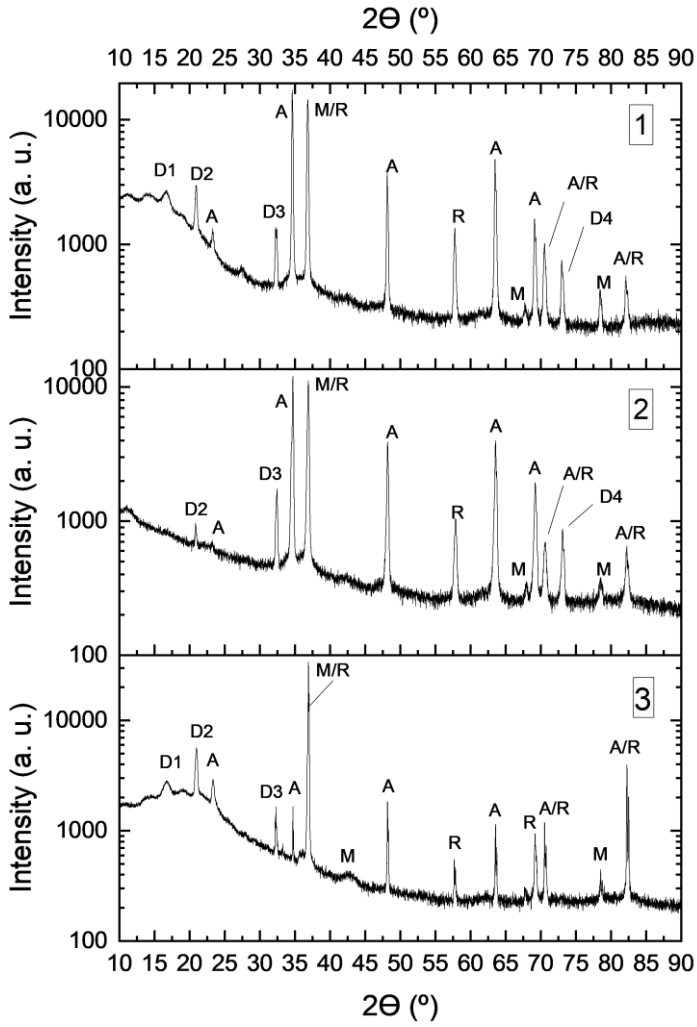

Figure A-6-14 XRD of AZ61A alloy with TiO_2 coating (1-ED at 1V for 45 minutes without annealing; 2- ED at 2V for 45 minutes without annealing; 3- ED at 1 V for 45 minutes with annealing)

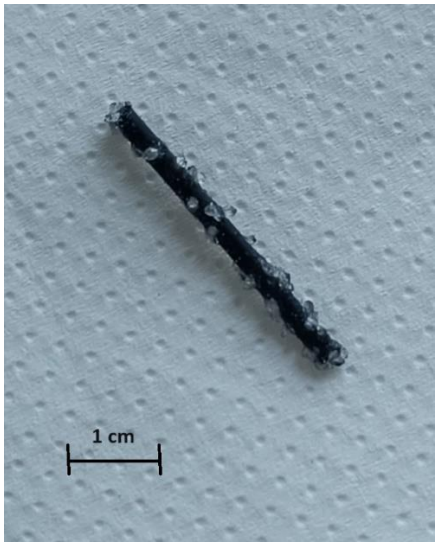

Figure A-6-15 Photograph of precipitates formed during degradation tests.

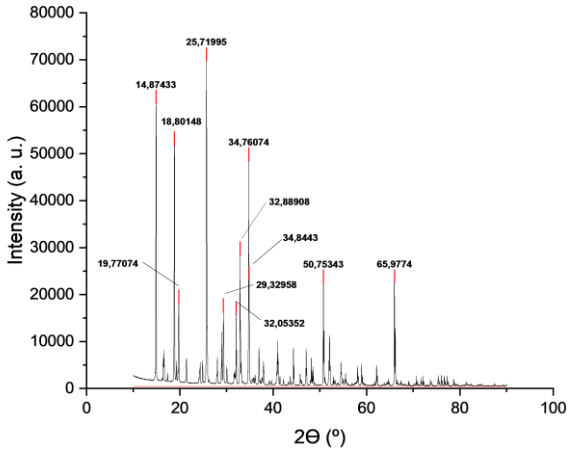

Figure A-6-16 Peak details in XRD of precipitates formed in degradation tests of uncoated and unannealed coated AZ61A alloy

Table A-6 Mass ratios in degradation tests

Substrate	PBS pH	Weight Ratio
AZ61A alloy	7.4	1,0547 ±0,0027
	5.5	0,8947 ±0,0181
Titanium alloy	7.4	1,0091 ±0,0215
	5.5	0,9989 ±0,0307
AZ61A Alloy + TiO_2 coating without annealing	7.4	1,1643 ±0,0082
	5.5	1,4774 ±0,1067
AZ61A Alloy + TiO_2 annealed coating	7.4	1,0443 ±0,0013
	5.5	1,2177 ±0,0819

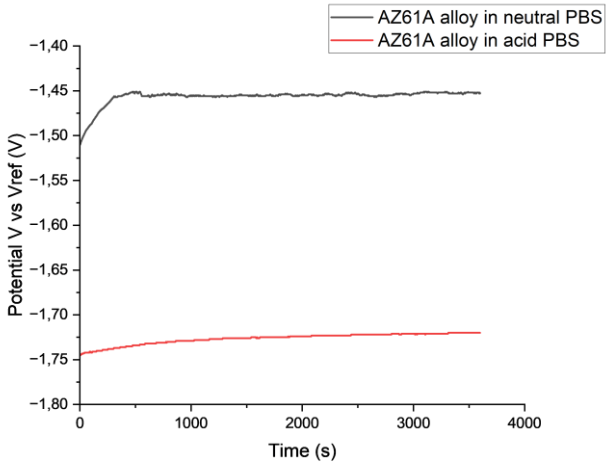

Figure A-6-17 OCP tests of AZ61A commercial alloy in neutral and acid PBS

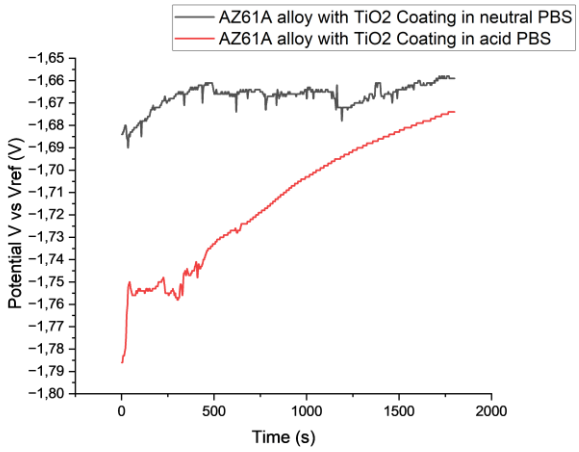

Figure A-6-18 OCP tests of AZ61A alloy with TiO_2 coating in neutral and acid PBS.

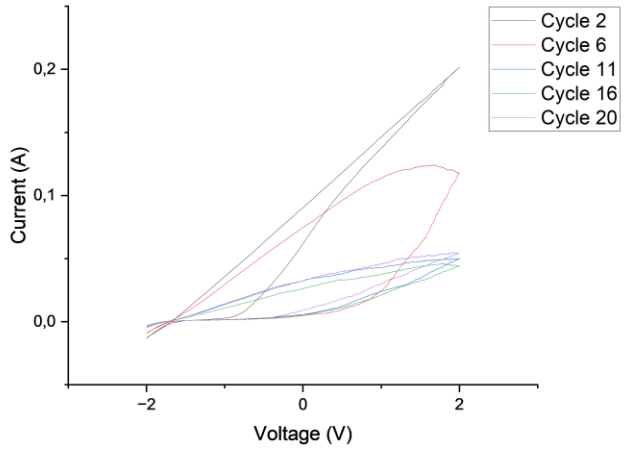

Figure A-6-19 CV of AZ61A commercial alloy in neutral PBS.

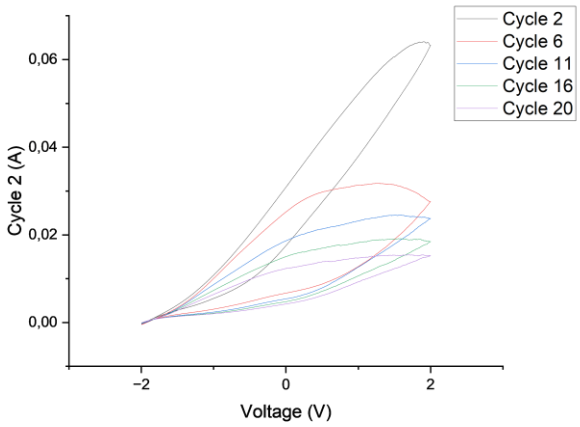

Figure A-6-20 CV of AZ61A commercial alloy in acid PBS.

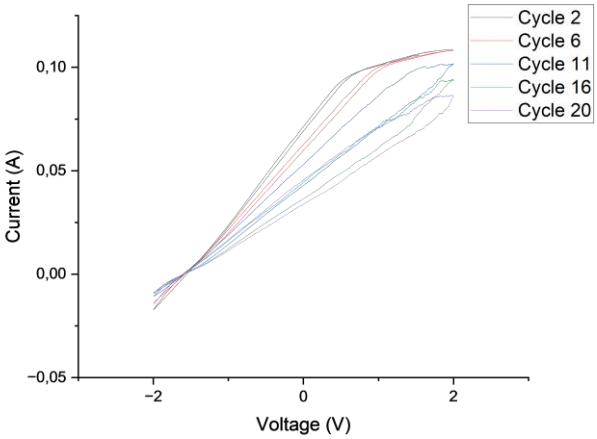

Figure A-6-21 CV of AZ61A commercial alloy with a TiO_2 coating, in neutral PBS

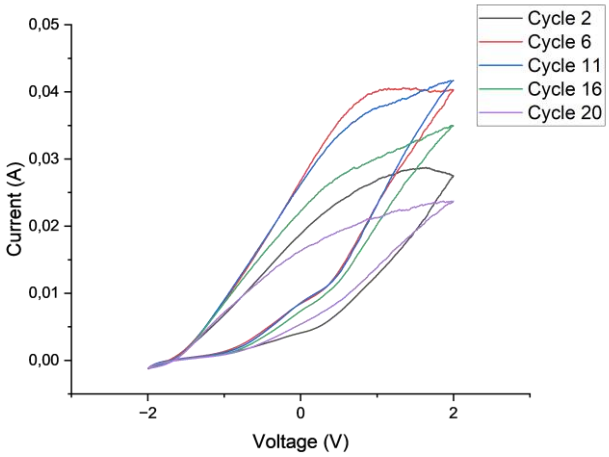

Figure A-6-22 CV of AZ61A commercial alloy with a TiO_2 coating, in acid PBS

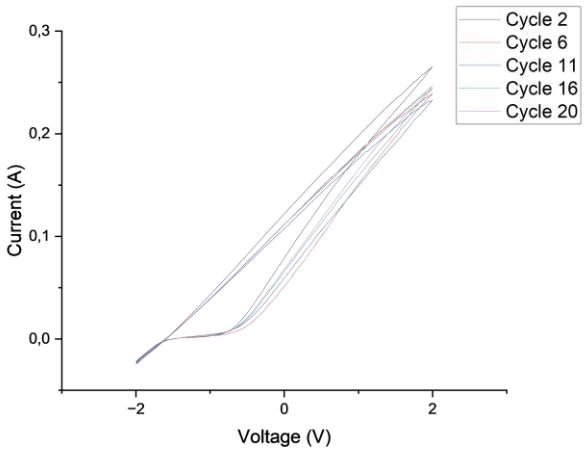

Figure A-6-23 CV of WAAM printed Substrates in neutral PBS.

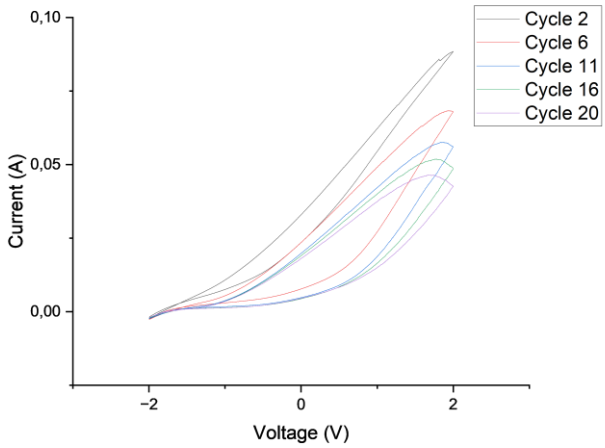

Figure A-6-24 CV of WAAM printed Substrates in acid PBS.

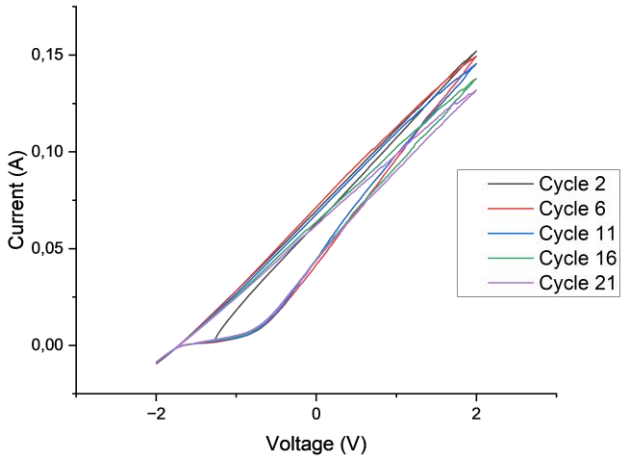

Figure A-6-25 CV of WAAM printed substrate with TiO_2 coating, in neutral PBS.

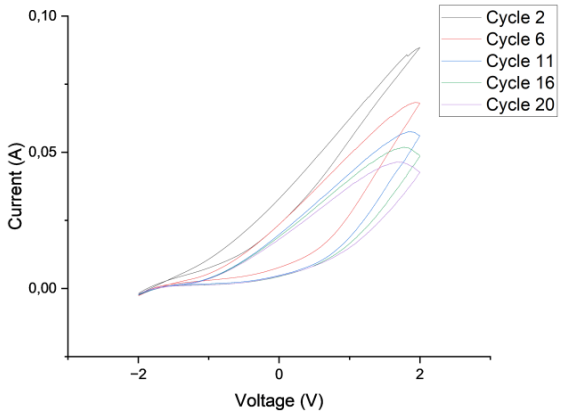

Figure A-6-26 CV of WAAM printed substrate with TiO_2 coating, in acid PBS.

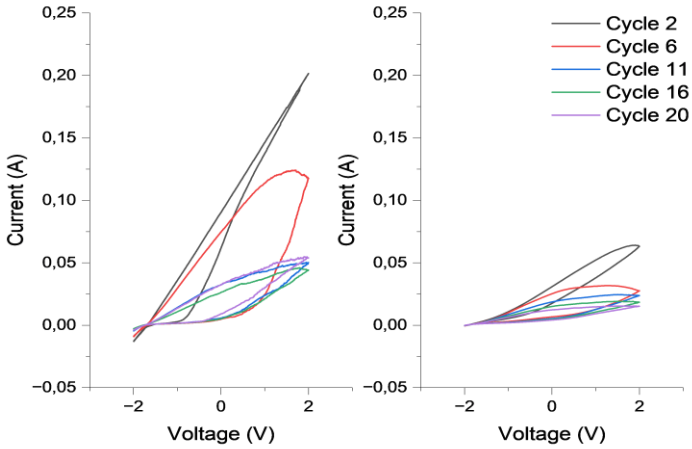

Figure A-6-27 Comparison between CVs of AZ61A commercial alloy in neutral PBS (left) and acid PBS (right).

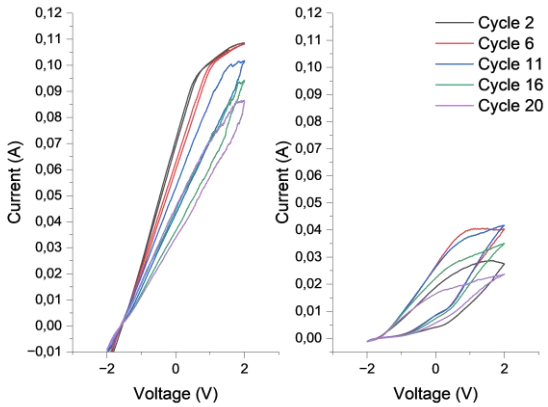

Figure A-6-28 Comparison between CVs of AZ61A commercial alloy with TiO_2 coating in neutral PBS (left) and acid PBS (right).

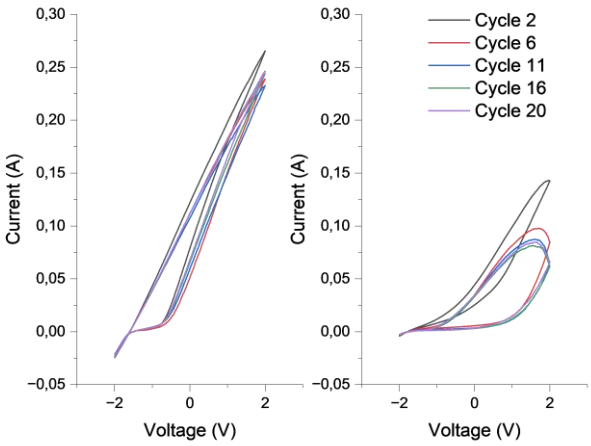

Figure A-6-29 CVs of AZ61A alloy WAAM printed substrates in neutral PBS (left) and acid PBS (right)

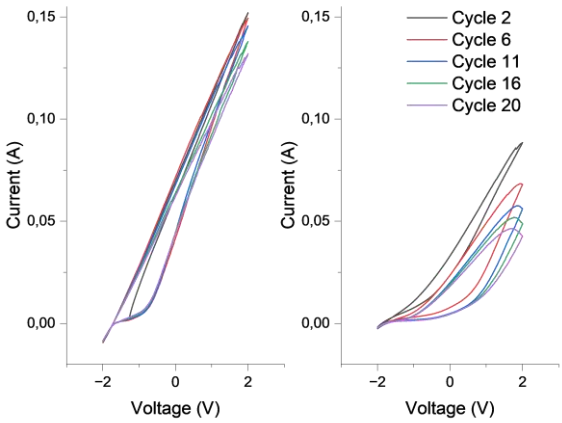

Figure A-6-30 CVs of AZ61A alloy WAAM printed substrates, with TiO_2 coating, in neutral PBS (left) and acid PBS (right)

Table A-7 Mass Ratios of the CV Experiments

	Neutral PBS	**Acid PBS**
AZ61A alloy	0,7197	0,6419
AZ61A alloy + TiO_2 coating	0,7701	0,8181
WAAM substrate	0,9799	0,9925
WAAM substrate + TiO_2 coating	0,9804	0,9947

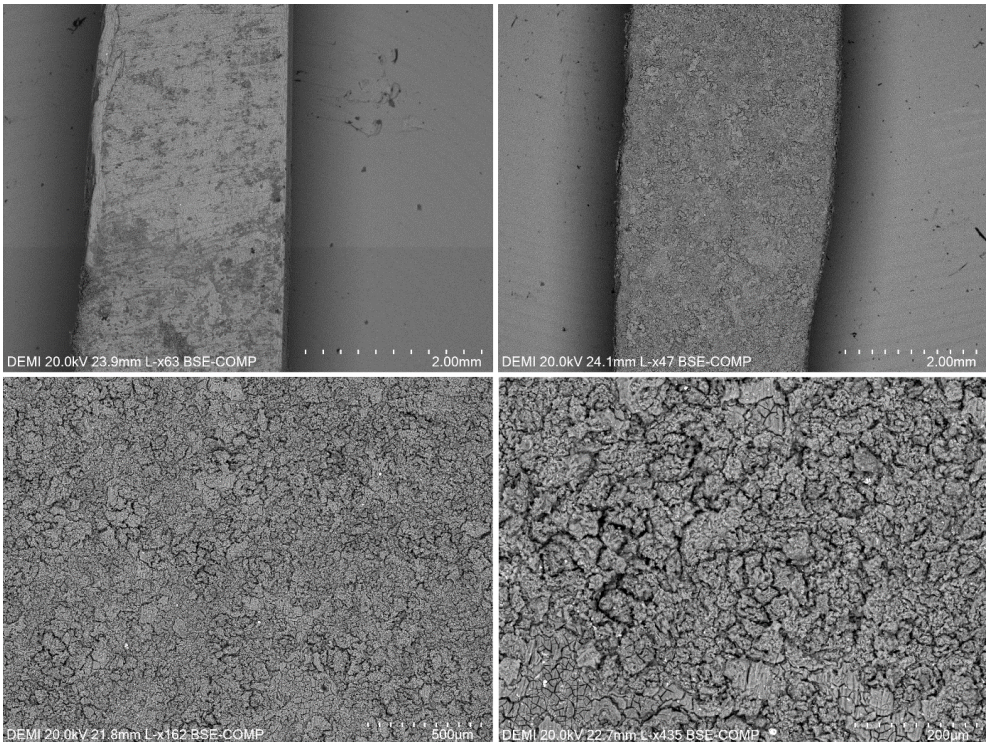

Figure A-6-31 SEM image of WAAM after CV in acid PBS.

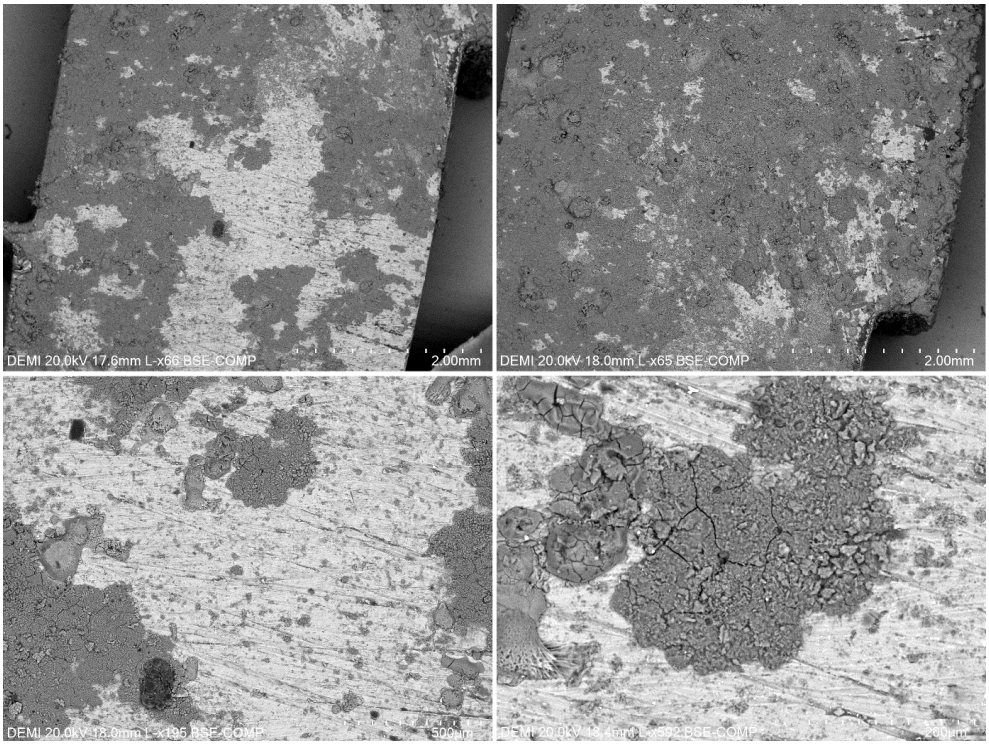

Figure A-6-32 SEM image of WAAM after CV in neutral PBS.

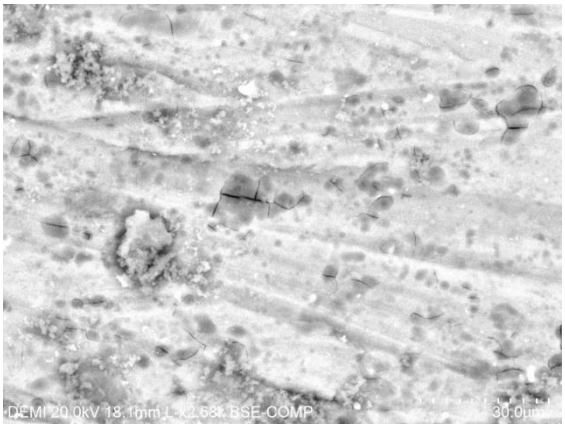

Figure A-6-33 SEM image of WAAM after CV in neutral PBS (detail).

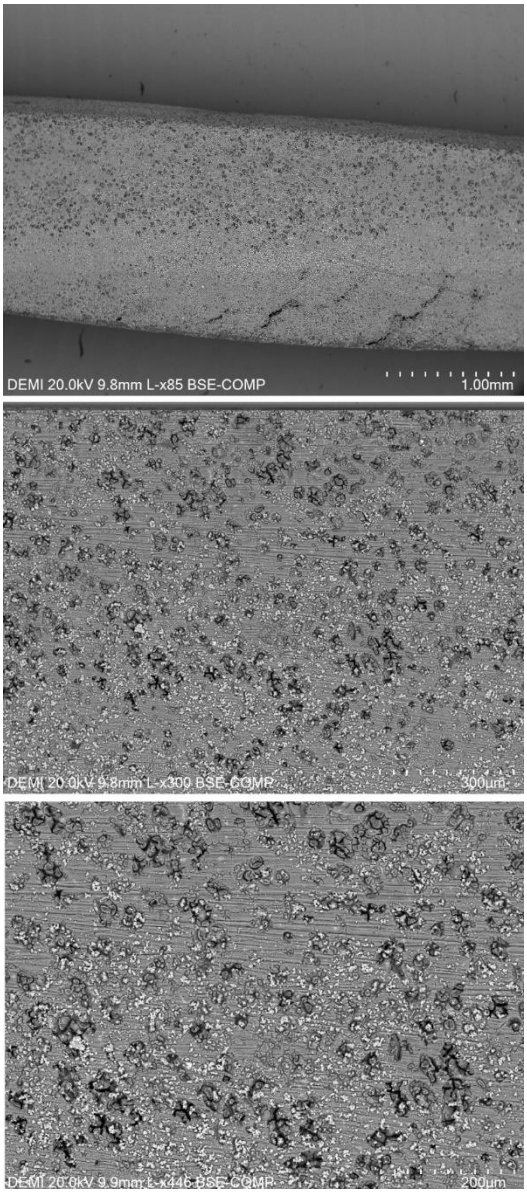

Figure A-6-34 SEM image of WAAM printed substrate with TiO_2 coating.

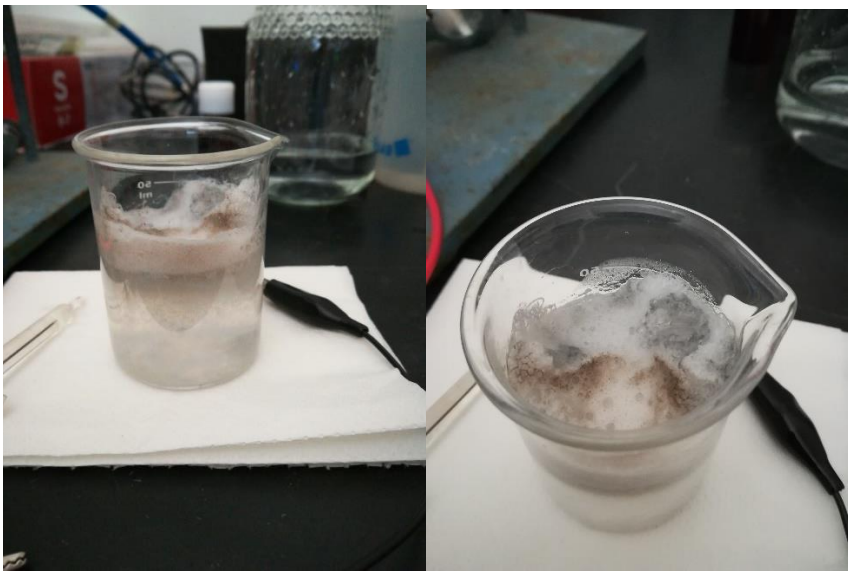

Figure A-6-35 Photograph of foam layer formed during CV tests.

Figure A-6-36 Photograph of WAAM printed substrates with TiO_2 coating (coating on the right side).

Figure A-6-37 Photograph of sliced WAAM printed substrates without TiO_2 coating.

Figure A-6-38 Photograph of the Linear Precison Saw Buehler Isomet 4000

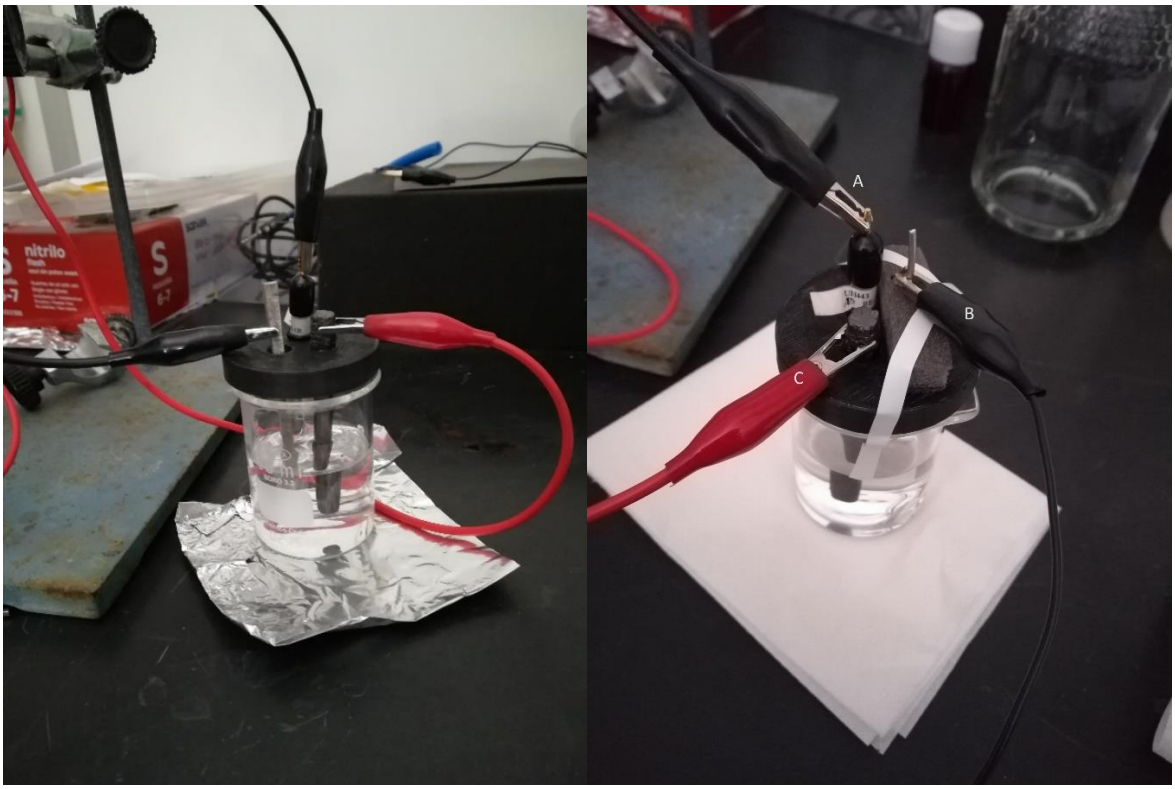

Figure A-6-39 Photograph of the three-electrode set up in CV experiments with reference electrode (A), working electrode (B) and counter eletrode (C)

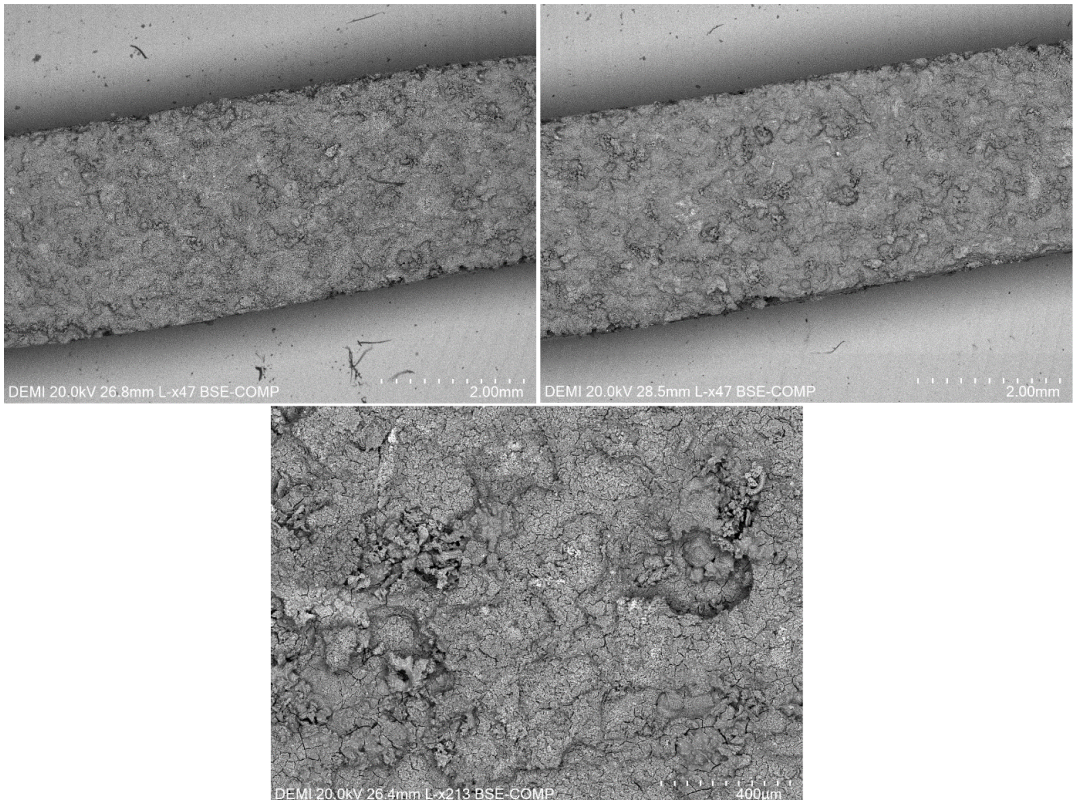

Figure A-6-40 SEM WAAM + TiO_2 coating after CV in PBS 7

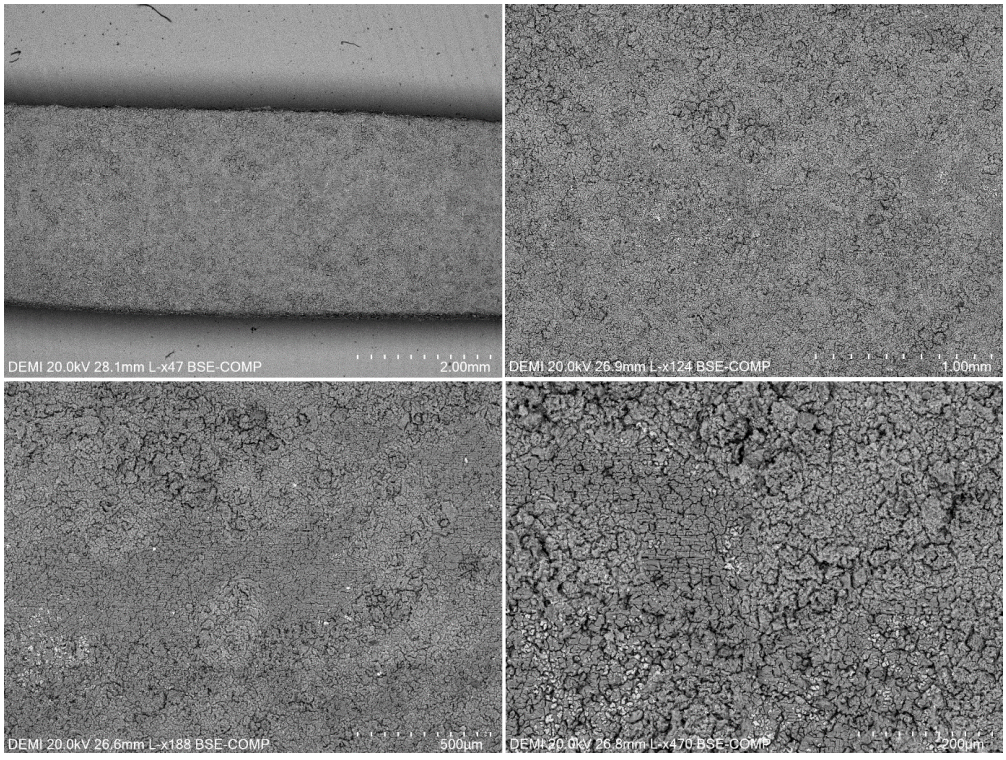

Figure A-6-41SEM WAAM + TiO_2 coating after CV in PBS 5,5

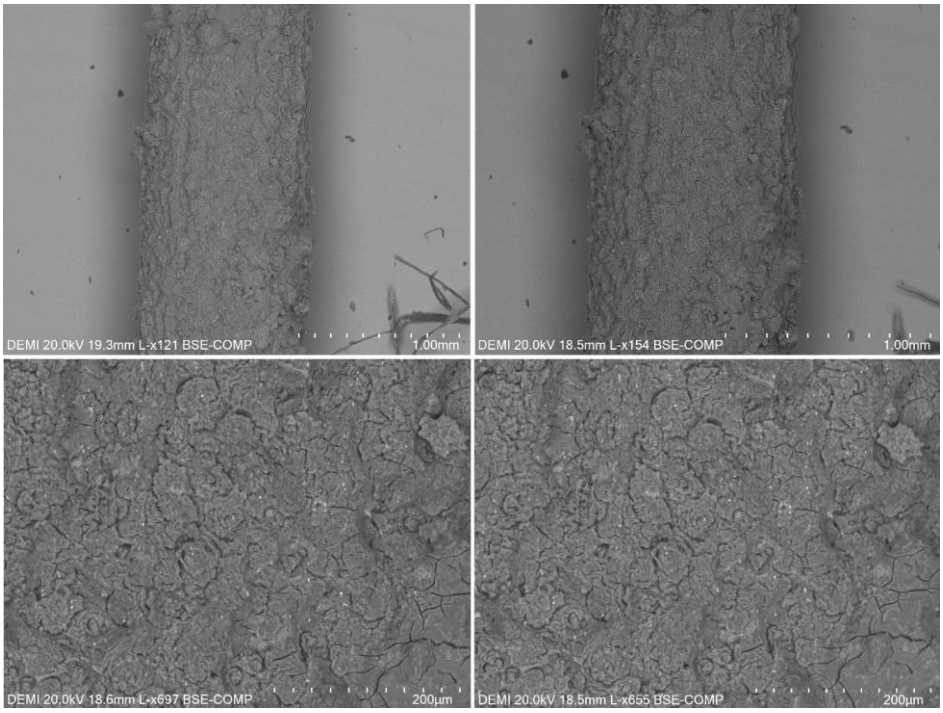

Figure A-6-42 SEM Image of AZ61A alloy with TiO_2 coating after CV in PBS 7

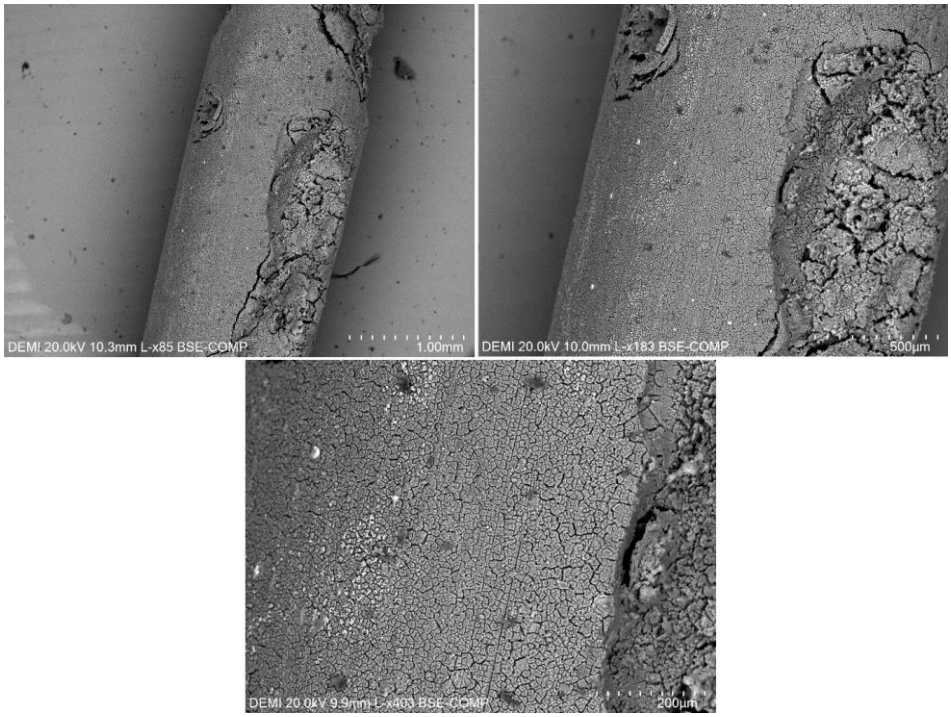

Figure A-6-43 SEM Image of AZ61A alloy with TiO_2 coating after CV in PBS 5,5